

**NUMERICAL EXPERIMENTS  
IN MODULATED TURBULENCE**

## Colophon

The research presented in this thesis was done within the Chair Numerical Analysis and Computational Mechanics (NACM), Department of Applied Mathematics, Faculty EEMCS, University of Twente, the Netherlands.



This work was supported by the research program *Turbulence and its role in energy conversion processes* of the Foundation for Fundamental Research of Matter (FOM) that is financially supported by the Netherlands Organization for Scientific Research (NWO).



This work was part of the research program of the J. M. Burgers School for Fluid Dynamics.



© Arkadiusz K. Kuczaj, Hengelo, 2006

No part of this work may be reproduced by print, photocopy or any other means without the permission in writing from the author.

ISBN 90-365-2430-X

# NUMERICAL EXPERIMENTS IN MODULATED TURBULENCE

## DISSERTATION

to obtain  
the doctor's degree at the University of Twente,  
on the authority of the rector magnificus,  
prof. dr. W. H. M. Zijm,  
on account of the decision of the graduation committee,  
to be publicly defended  
on Friday 8 December 2006 at 15:00

by

**Arkadiusz Krzysztof Kuczaj**

born on 11 April 1975  
in Nowa Ruda, Poland

This dissertation has been approved by the promotors:

prof. dr. ir B. J. Geurts

prof. dr. ir J. J. W. van der Vegt

# Preface

This dissertation is the outcome of my work in the project “Fractal forcing of anisotropic, inhomogeneous turbulent flow” being a part of the Fundamental Research on Matter program “Turbulence and its role in energy conversion processes”. I wish to thank the following individuals and organizations for their support in developing this project.

First and foremost I would like to gratefully acknowledge my supervisor Bernard Geurts. He has supported me with his knowledge and scientific enthusiasm whilst allowing me to work in my own way throughout the whole period of my research studies at the University of Twente.

I would like to thank the members of the Turbulence Working Group–Twente (TWG–T) for many interesting discussions and the NACM group headed by Jaap van der Vegt.

Many people directly or indirectly contributed to this work. Especially, I would like to thank Darryl Holm (Imperial College & Los Alamos National Laboratory), Detlef Lohse (University of Twente), David McComb (University of Edinburgh), Arkady Tsinober (Imperial College), and Willem van de Water (Eindhoven University of Technology).

Darryl Holm has organized my summer research program at the Los Alamos National Laboratory and shared with me his great scientific knowledge in the field of turbulence modelling. Detlef Lohse has contributed to the study of the response maxima in periodically forced turbulence. David McComb has provided me with valuable insights into many aspects of my work during

my research visits at the University of Edinburgh. I appreciate Arkady Tsinober for his remarks regarding geometrical statistics of turbulence in the context of my work. I am grateful to Willem van de Water for many interesting discussions and valuable remarks.

The computational support from local NACM/MPCM facilities and SARA Supercomputer Center in Amsterdam is greatly appreciated. I would like to thank Bert van Corler (SARA), Willem Vermin (SARA), Enno Oosterhuis (UT), and Peter Michielse (NWO).

Privately, many thanks go to my former office-mates Kirankumar Hiremath, Fedderik van der Bos, and Milan Maksimovic, secretaries: Marielle Plekenpol, Diana Dalenoord, and the whole staff and students in the Department of Applied Mathematics at the University of Twente.

Special thanks go to Agnieszka and my parents for their emotional support.

Arkadiusz K. Kuczaj

Hengelo, December 2006

# Contents

<b>1</b>	<b>Introduction</b>	<b>1</b>
<b>2</b>	<b>Mixing in manipulated turbulence</b>	<b>9</b>
2.1	Introduction . . . . .	10
2.2	Simulation of forced turbulence . . . . .	13
2.3	Modulated cascading by broadband forcing . . . . .	25
2.4	Small and large scale mixing efficiency . . . . .	33
2.5	Conclusions . . . . .	39
<b>3</b>	<b>Energy dynamics in broadband-forced turbulence</b>	<b>49</b>
3.1	Introduction . . . . .	50
3.2	Computational flow model . . . . .	53
3.3	Broadband-forced turbulence . . . . .	62
3.4	Two- and three-mode interaction of scales . . . . .	70
3.5	Conclusions . . . . .	76
<b>4</b>	<b>Response maxima in periodically forced turbulence</b>	<b>81</b>
4.1	Introduction . . . . .	81
4.2	Computational flow model . . . . .	83
4.3	Averaging procedure and simulation setting . . . . .	85
4.4	Modulated turbulence . . . . .	88
4.5	Conclusions . . . . .	91

---

<b>5</b>	<b>Turbulence modification by time-periodic forcing</b>	<b>93</b>
5.1	Introduction . . . . .	94
5.2	Computational flow model . . . . .	96
5.3	Periodic modulation . . . . .	98
5.4	Conclusions . . . . .	107
<b>6</b>	<b>Concluding remarks and outlook</b>	<b>111</b>
	<b>Bibliography</b>	<b>115</b>
	<b>Summary</b>	<b>125</b>
	<b>Curriculum vitae</b>	<b>131</b>



# Chapter 1

## Introduction

The understanding and control of turbulence has tremendous significance in a variety of fluid flows. Examples are readily found in astrophysical, geophysical and environmental flow problems, in atmosphere weather predictions and aerospace applications, and in countless industrial innovations. Apart from the scientific importance of basic turbulence phenomena, various accompanying transport processes are often strongly influenced by turbulence. One example that is considered in this thesis is scalar *mixing*. A proper description of mixing can not be achieved without an understanding of turbulence. Mixing involves mechanical stirring (dispersion) that is purely convective and brings different fluid parcels into contact through the action of stresses and strain. Diffusion processes further spread the tracer on all scales present in a flow. These processes operate together and are enhanced by turbulent flows that make them of large interest in engineering and industrial applications.

The general purpose of this thesis is to study the influence of turbulence on the efficiency of mixing, with the use of numerical simulations. One way to influence the mixing efficiency is to change the turbulence intensity through time- and space-dependent agitation. In practice, this can be achieved for example by shaking or stirring of flows in some prescribed way, e.g., by following a time-periodic protocol or by adopting a geometrically complex blender architecture. In this thesis we will consider the situation of non-

ideal, modulated turbulence, in which the flow is disturbed on various scales of motion in physical space and the modulation may periodically vary in time. We will quantify flow structuring, energy dynamics consequences of such modulations and their influence on mixing characteristics.

Before presenting the content of this thesis, we will very briefly consider some basic phenomenology of turbulence phenomena. Then the content of each chapter will be presented and finally the general outline of this thesis will be given.

**Basic phenomenology of turbulence.** What makes turbulence so difficult to understand? In a turbulent flow we observe for the most energetic length-scales a strong momentum convection, a small momentum diffusion and rapid variations of pressure and velocity in space and time. From the mathematical point of view these processes are completely described by the Navier–Stokes equations that govern the fluid flow. The incompressible Navier–Stokes equations without external forces have the following form

$$\frac{\partial \mathbf{v}}{\partial t} + (\mathbf{v} \cdot \nabla) \mathbf{v} = -\nabla p + \nu \nabla^2 \mathbf{v} \quad ; \quad \nabla \cdot \mathbf{v} = 0, \quad (1.1)$$

where  $\mathbf{v}(\mathbf{x}, t)$  is the velocity,  $p(\mathbf{x}, t)$  is the pressure and  $\nu$  is the kinematic viscosity of a fluid. These equations form a system of nonlinear coupled partial differential equations that represent the conservation principles of momentum and mass. By providing suitable initial and boundary conditions we make their possible solution fully deterministic in time and space.

The numerical solutions in a turbulent regime typically display a significant dependence on small-scale features. Given small differences in the initial conditions of the numerical or physical experiments, either way, we often end-up with totally different outcomes of turbulent flow already after a short time. The initial differences will grow with time, which is a signature of deterministic chaos present in the nonlinearity embedded in the Navier–Stokes equations. For example, if the initial uncertainties are below measurement accuracy, we cannot control them explicitly and the system ultimately appears unpredictable, due to experimentally non-repeatable outcomes. This is encapsulated in the widely known *butterfly effect* that expresses the sensitive dependence on initial conditions and makes for example long-term weather predictions so difficult.

---

One wonders whether it is possible at all to make a theoretical model to describe the primary aspects of the behavior of turbulence. The intriguing energy cascading process, suggested by Kolmogorov's universality hypothesis of independence between large and small scales [58], serves quite well to provide at least an approximate model of energy dynamics in turbulence. Moreover, the self-amplification mechanism between vorticity and strain [100] suggests that turbulence possesses its own geometrical structure. This gives some hope to construct such a theory of turbulence. Application of renormalization group analysis for basic turbulent flows [71] or regularization-type models [47, 48] opens new mathematical and computational perspectives that may be used to explore more complex flows in the future.

**Computer Aided Understanding of turbulence.** The sensitivity to the initial condition and the vast extent of scales that must be taken into account to properly represent the scales in a turbulent flow are very problematic issues. Fortunately, developments in two scientific disciplines, i.e., High-Performance Computing (HPC) and Computational Fluid Dynamics (CFD) allow considering flows that so far were computationally inaccessible [82]. This provides a research approach that may give detailed access to all flow properties in canonical turbulent flows such as homogeneous turbulence, shear layers, boundary layers and complex interacting vortex systems such as arise in the wake of an airplane.

By nondimensionalizing the Navier–Stokes equations one observes that flow conditions may be labeled with a single dimensionless number. This expresses the ratio of the inertial to the viscous forces and is known as the Reynolds number

$$\text{Re} = \frac{UL}{\nu}, \quad (1.2)$$

where  $U$  is the characteristic velocity,  $L$  is the characteristic length, and  $\nu$  the kinematic viscosity introduced earlier. Large Reynolds numbers indicate that inertial forces dominate the viscous forces. This corresponds to situations in which the nonlinear convective effects are important. In such regimes a broad range of scales will be present in the flow that must be resolved in computations.

The largest scales that will occur in a flow are of the size of the characteristic length  $L$  that macroscopically describes the system for which we want to find a solution, e.g., the length of a pipe or size of a channel. The smallest dynamically relevant scales are related to viscosity, hence they directly depend on the Reynolds number. From dimensional analysis, the disparity of these length scales in turbulent flow can be calculated by raising the Reynolds number to the  $3/4$  power:

$$L/\eta \sim \text{Re}^{3/4}, \quad (1.3)$$

where  $\eta$  is the Kolmogorov scale. The above ratio can be used to estimate the number of grid points that is needed for accurate simulations of turbulence. In fact, the required number of grid points is proportional to the Reynolds number raised to the  $9/4$  power because of three-dimensionality. Correspondingly, the amount of scales that needs to be resolved is enormous, making extreme demands on the computational effort that is involved.

The computational challenge represented by turbulent flow has stimulated the progress in CFD methods. A popular division of current methods is into three general groups: Direct Numerical Simulations (DNS), Large-Eddy Simulations (LES) and Reynolds Averaged Navier–Stokes Simulations (RANS). Simplifying, the first group of methods exactly resolves all scales present in a flow, the second - divides them into two parts, that are either resolved or modeled and the latter - solves the long-time averaged equations for the mean flow. Both LES and RANS require the introduction of an explicit model that accounts for small-scale turbulence (LES), or the Reynolds stresses (RANS). The energy transfer among eddies and statistical correlations between velocities play an important role in LES and RANS descriptions. The DNS approach gives numerically exact solutions of the Navier–Stokes equations at very high computational cost, while the other two approaches are computationally less demanding and applicable in industry to varying degree.

Turbulence requires a continuous supply of energy to overcome the viscous damping that prevents it to exist by itself. For example, Earth's atmosphere is ultimately forced by radiation from the Sun that translates into at least two sources of agitation, i.e., temperature gradients transporting heat from hot to cold regions and wind shear that generates vortices.

Studying turbulent flow requires attention for the dynamics described by the Navier–Stokes equations in combination with the boundary (forcing) conditions that supply energy to the system. Aspects such as amplitude, spectral content and temporal variation of the forcing can have an important effect on the resulting turbulent flow. This is the general area where the work presented in this thesis starts to play a role.

**Thesis content.** This dissertation addresses fundamental aspects in turbulence using Direct Numerical Simulations. The main emphasis is placed on forcing methods. These can be used as instruments to better understand the dynamics and structures present in the numerical solutions of the Navier–Stokes equations. Likewise, such forcing schemes may serve as modeling tools that account for specific boundary conditions, for example in complex geometry flows such as flow over a forest, or through a metal foam. This may help to understand turbulence and stimulate the construction of approximate models that can accurately capture the primary dynamics of turbulent flows for example in large-eddy simulations. We restricted our study to the canonical problem of turbulent flow in basic geometry of a cubic box with periodic boundary conditions. We studied in detail the consequences of turbulence modulation introduced by forcing.

In brief, the main topics addressed in this thesis are:

**Mixing in manipulated turbulence.** For an idealized turbulent flow various large-scale (stochastic and deterministic) forcing methods were invented. They basically supply the energy and sustain a quasistationary state in turbulence. We will examine these methods concentrating on deterministic procedures in spectral space that modulate the flow properties. While forcing is commonly applied to large scales only, we focus on consequences when forcing is also applied in an extended range, i.e., modifying a broader set of scales. We will study how such broadband agitation of smaller scales modulates the flow-transport properties. This is achieved by evaluating passive scalar fields driven by modulated turbulence. We will start with a spherically shaped initial tracer and see how it is dispersed by turbulent flow using various configurations of broadband forcing.

We will look at the instantaneous and cumulative effects evaluating surface area, curvature and wrinkling of passive scalar concentration at chosen iso-levels. We use these simulations primarily to illustrate broadband forcing as a modelling tool that can be used to modulate turbulence in a specific way.

**Energy dynamics in broadband-forced turbulence.** The broadband forcing directly introduces energy to explicitly specified smaller scales. The injection of energy influences a broader range of scales through nonlinear interactions present in the energy transfer function and modulates the energy distribution between scales compared to the reference Kolmogorov case. We will concentrate on the energy transfer in the broadband context, studying the effect of energy injection at various scales of motion in terms of the partitioned energy transfer function between various triad contributions. We will investigate the magnitude of the contributions from various spatial scales to the overall energy transfer.

**Response maxima in periodically forced turbulence.** Another example of non-ideal turbulence considered here is turbulence modulated via time-periodic forcing. The numerical investigations performed here were motivated by the results of theoretical studies of the response of turbulence subject to periodically modulated stirring [44]. We will look at the amplification of the response of turbulence found for specific stirring frequencies of the order of the inverse of the eddy-turnover time. The amplified response is observed for various quantities like kinetic energy, energy-dissipation rate or microscale Taylor-Reynolds number. The obtained results are in agreement with theoretical predictions and may serve as a link between theory and experimental results obtained in periodic-modulated systems.

**Turbulence modification by time-periodic forcing.** The maximal response in amplitude found for the large-scale periodically forced turbulence along with a characteristic phase-shift between forcing

---

and analyzed quantities (e.g., total energy or energy-dissipation rate) opens the question of the actual roots of this phenomenon. We will perform a parameter study and numerically analyze the influence of the amplitude of the forcing modulation, the periodic protocol and the extent of agitated scales on the turbulence amplitude response. This way the importance of the cascading effect can be directly investigated establishing mainly the large-scale character of the response maxima. The variation of the amplitude modulation will be confronted with theoretical predictions obtained for small values of the amplitude.

**Outline.** The organization of the thesis is as follows. In Chapter 2 we give an overview of different forcing methods used as basic research tools in turbulence. We present and evaluate the numerical method used to solve the Navier–Stokes equations and describe the extension of the large-scale forcing to its broadband representation in spectral space along with its spatial localization in physical space. We examine the effects of such a forcing method application on flow transport properties concentrating on the dispersion of passive scalar tracers. The energy dynamics of the broadband-forced turbulence is investigated in Chapter 3. We present a numerical study of the energy transfer terms and scale interactions in the broadband forcing context. In Chapter 4 we investigate periodically modulated large-scale forced turbulence. We confirm the existence of response maxima in periodically modulated turbulence using DNS. We present the ensemble-averaging procedure that was used in this case. Based on these investigations we further examine the application of periodic forcing in Chapter 5. We study the response of turbulence to forcing with more complex harmonic variations in time and vary the amplitude of forcing and the extent of the agitated scales. In the last chapter concluding remarks with an outlook for further research in this field are given.

The collected chapters are independent papers that appeared previously in *Journal of Turbulence*, *Physical Review E* and *Europhysics Letters* with the exception of Chapter 5 that was recently submitted to *Computers & Fluids*.





# Chapter 2

## Mixing in manipulated turbulence<sup>†</sup>

A numerical investigation of turbulent flow, subject to deterministic broadband forcing, is presented. Explicit forcing procedures are included that represent the simultaneous agitation of a wide spectrum of length scales, including both large scales as well as a band of much smaller scales. Such forcing induces a multiscale modulation of turbulent flow that is motivated by flow through complex objects and along irregular boundaries. Two types of forcing procedures are investigated; with reference to the collection of forced modes these procedures are classified as “constant energy” or “constant-energy input rate”. It is found that a considerable modulation of the traditional energy cascading can be introduced with a specific forcing strategy. In spectral space, forcing yields *strongly localized* deviations from the common Kolmogorov scaling law, directly associated with the explicitly forced scales. In addition, the accumulated effect of forcing induces a significant *nonlocal* alteration of the kinetic energy including the spectrum for the large scales. Consequently, a manipulation of turbulent flow can be achieved over an extended range, well beyond the directly forced scales. Compared to flow forced in the large scales only, the energy in broadband-forced turbulence is found to be transferred more effectively to smaller scales. The turbulent mixing of a passive scalar field is also investigated, in order to quantify the physical-space modifications of transport processes in multiscale forced turbulence. The surface area and wrinkling of level sets of the scalar field are monitored as measures of the influence of explicit forcing on the local and global mixing efficiency. At small Schmidt numbers, the values of surface area are mainly governed by the large scale sweeping-effect of the flow while the wrinkling is influenced mainly by the agitation of the smaller scales.

---

<sup>†</sup>“*Mixing in manipulated turbulence*” by A. K. Kuczaj and B. J. Geurts to appear in *Journal of Turbulence* as a paper associated with the focus-issue *Multi-scale Interactions in Turbulent Flows Workshop* held in Center for Nonlinear Studies at Los Alamos National Laboratory, Santa Fe, New Mexico, USA (July 18-21, 2005) [60].

## 2.1 Introduction

Various multiscale phenomena in turbulent flows arise from the passage of fluid through and along geometrically complex objects placed inside the flow domain. The corresponding perturbations of the flow arise simultaneously on a range of length scales and find their origin in the complexity of the boundaries of these objects. A motivating example is the flow through a porous region such as a metal foam depicted in Fig. 2.1. Many more examples can readily be mentioned, arising in different technological applications or in numerous natural flows, including flow over forest canopies [31, 2, 11].

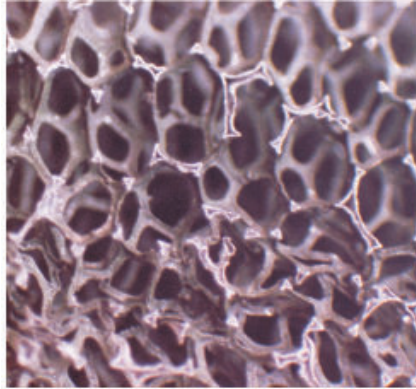


**Fig. 2.1:** A porous nickel foam contains various geometrical complexities on different length scales [65].

The purpose of this paper is to investigate the computational modeling of flows through complex regions via the introduction of explicit forcing terms in the Navier–Stokes equations. Consistent with the many shape details of the obstructing objects, such forcing will need to represent the perturbation of the flow on various length scales simultaneously. This distinguishes the proposed computational modeling from more conventional forced turbulence procedures. In the latter the flow agitation is restricted to a few large scales only with the aim to observe the development of a natural inertial range at smaller scales in the turbulent flow [103, 54]. Instead, in this paper we allow the forcing of a collection of widely different modes.

The consequences for transport and dispersion in such turbulent flows will be studied both in spectral as well as in physical space. We will primarily establish the degree by which the spectral properties of a turbulent flow can be modified relative to the classical Kolmogorov scaling, and quantify the efficiency with which embedded scalar fields can be mixed by the modulated flow.

Complementary to the proposed explicit forcing approach, two alternative formulations have been put forward in literature to capture the flow in and around complex objects. These include the explicit boundary modeling [106] as well as an approximation in terms of effective boundary conditions and (surface) roughness parameters [46, 51]. The roughness parametrization has been introduced for situations in which the roughness length scales are much smaller than the boundary layer thickness [99]. For geometries that display both large- and small-scale contortions of the shape of the object, compared to the boundary layer thickness, the surface-roughness parametrization may not be sufficiently accurate [22]. Alternatively, in case of explicit boundary modeling, no-slip conditions are imposed at all the intricate shape details of the object. This computational approach can in principle achieve full accuracy but is limited to cases of modest complexity in view of the elaborate geometric modeling and the high computational expenses that are required [14, 13].

A central motivation for the present paper is derived from the problem of *universality* in turbulence, i.e., the degree of (in-)dependence of the large and the small scales in turbulence on the type of forcing that drives the flow. This problem was addressed earlier through numerical simulation, e.g., in Refs. [43, 90, 6, 7]. Specifically, these simulations employed stochastic power-law forcing methods and investigated the occurrence and properties of an inertial range of scales that separates the large and the small scales. The scaling relations of velocity structure functions were found to deviate from the well-known Kolmogorov prediction [8]. This is commonly referred to as anomalous scaling that signals the occurrence of multifractality in turbulence [6]. This also suggests a degree of dependence of the velocity fluctuations on the particular stirring mechanism that is used, thereby affecting to some extent all scales present in the flow. As a physical example, flow through complex gasket structures may give rise to self-similar turbulence spectra, which do not follow the well known Kolmogorov  $-5/3$

slope [58]. Such non-Kolmogorov turbulence was observed in flows over tree canopies, and is reminiscent of a spectral shortcut feature that was also observed experimentally [31]. In this paper we investigate the potential of multiscale forcing to accurately characterize such dynamic flow consequences of complex domain boundaries without the need to explicitly account for their intricate geometrical shape. We consider the incompressible Navier–Stokes equations with multiscale forcing working as a stirrer whose dynamical effects are controlled by a distribution of simultaneously perturbed length scales. To arrive at a multiscale modeling that is quantitatively linked to actual complex objects several steps need to be taken. In this paper we address a first step in which we examine in some detail the influence different forcing procedures have on the energy dynamics in spectral space and the mixing characteristics in physical space. Special attention is devoted to the mixing efficiency of a passive tracer by monitoring the surface area and wrinkling of level sets of these scalar fields [33]. Specifically we look at the instantaneous and accumulated effect on surface area and wrinkling caused by broadband forcing.

Different divergence-free forcing procedures will be applied to directly perturb a large number of flow scales. The alterations of the flow dynamics express themselves clearly in the kinetic energy. The transfer of energy toward smaller scales is found to increase considerably, compared to the case in which only large scales are forced. When a specific narrow band of scales is agitated by the forcing, then the locally higher spectral energy is not “compatible” with the molecular dissipation rate and an accelerated transfer is observed toward smaller scales. This effect is found for both families of forcing methods, i.e., constant energy and constant-energy input rate. The kinetic energy spectrum is also modified nonlocally, in a range of scales that are larger than the directly forced scales. Consequently the agitation of a band of small length scale features can accumulate and also induce significant alterations of the largest flow features, e.g., by contributing to an increased backscatter.

The changes in the flow dynamics due to the application of broadband forcing also has consequences for the turbulent transport properties of the flow. This may be expressed in terms of the mixing efficiency of embedded passive scalars. In particular, monitoring the surface area of level sets of the passive scalar allows to characterize changes in the large-scale sweeping of the

flow, due to the forcing. Likewise, the more localized motions directly affect the “wrinkling” of the passive scalar level sets. The dependence of these measures for the mixing efficiency on forcing parameters can be used to quantify the mixing efficiency arising from agitation of different bands of flow structures with different forcing strengths. Specifically, we investigate the dispersion of strongly localized initial scalar concentrations. The direct numerical simulation of the forced turbulence shows that the maximal surface area and wrinkling as well as the time at which such a maximum is achieved can be controlled by variation of forcing parameters. The time-integrated surface area and wrinkling are indicators of the accumulated effect. The simulations show that at small Schmidt numbers, a higher emphasis on small-scale flow agitation yields a significant increase in the time-integrated total mixing of the flow.

The organization of this paper is as follows. In Sec. 2.2 the explicit forcing strategies are introduced. Section 2.3 is devoted to the modulation of the cascading process associated with the different forcing methods. The consequences of forced turbulence for transport and dispersion in physical space will be quantified in Sec. 2.4. Concluding remarks are collected in Sec. 2.5. The simulation method, together with the code validation is presented in a separate Appendix.

## 2.2 Simulation of forced turbulence

In this section we will first introduce the governing equations (subsection 2.2.1) and subsequently describe the explicit forcing strategies that are used to drive the flow (subsection 2.2.2). Two types of deterministic forcing strategies will be included: procedures that yield constant energy in the collection of forced modes, and procedures that correspond to a constant-energy input rate for these modes.

### 2.2.1 Governing equations

The dimensionless system of nonlinear partial differential equations that governs the flow of a viscous incompressible fluid is given by

$$\begin{cases} \frac{\partial \mathbf{v}(\mathbf{x}, t)}{\partial t} + (\mathbf{v}(\mathbf{x}, t) \cdot \nabla) \mathbf{v}(\mathbf{x}, t) = -\nabla p(\mathbf{x}, t) + \nu \nabla^2 \mathbf{v}(\mathbf{x}, t) + \mathbf{f}(\mathbf{x}, t) \\ \nabla \cdot \mathbf{v}(\mathbf{x}, t) = 0, \end{cases} \quad (2.1)$$

where  $\mathbf{v}$  is the velocity field and  $p$  the pressure. The dimensionless viscosity is the inverse of the computational Reynolds number  $\text{Re}$ , i.e.,  $\nu = 1/\text{Re}$ , and  $\mathbf{f}$  is the external forcing, which we will specify in subsection 2.2.2. This system of equations may be rewritten in terms of the vorticity  $\omega(\mathbf{x}, t) = \nabla \times \mathbf{v}(\mathbf{x}, t)$ . Making use of the identity

$$\left(\mathbf{v}(\mathbf{x}, t) \cdot \nabla\right) \mathbf{v}(\mathbf{x}, t) = \omega(\mathbf{x}, t) \times \mathbf{v}(\mathbf{x}, t) + \frac{1}{2} \nabla \left( |\mathbf{v}(\mathbf{x}, t)|^2 \right), \quad (2.2)$$

we may express Eq. (2.1) as

$$\left(\frac{\partial}{\partial t} - \nu \nabla^2\right) \mathbf{v}(\mathbf{x}, t) = \mathbf{w}(\mathbf{x}, t) - \nabla \left( p(\mathbf{x}, t) + \frac{1}{2} |\mathbf{v}(\mathbf{x}, t)|^2 \right) + \mathbf{f}(\mathbf{x}, t), \quad (2.3)$$

where we introduced the nonlinear term  $\mathbf{w}(\mathbf{x}, t) = \mathbf{v}(\mathbf{x}, t) \times \omega(\mathbf{x}, t)$ .

The flow domain is assumed to be periodic with the same period in each of the three coordinate directions. An efficient representation of the solution in terms of Fourier modes can be adopted [17, 71, 110] in which the velocity  $\mathbf{v}(\mathbf{x}, t)$  is expanded as

$$\mathbf{v}(\mathbf{x}, t) = \sum_{\mathbf{k}} \mathbf{u}(\mathbf{k}, t) e^{i\mathbf{k} \cdot \mathbf{x}}, \quad (2.4)$$

and the wave vector  $\mathbf{k}$  ( $k = |\mathbf{k}|$ ) has components  $k_\alpha = 2\pi n_\alpha / L_b$ ,  $n_\alpha = 0, \pm 1, \pm 2, \dots$  for  $\alpha = 1, 2, 3$ . The dimensionless length of the periodic domain is denoted by  $L_b$  and  $u_\alpha(\mathbf{k}, t)$  is the Fourier coefficient corresponding to the  $\mathbf{k}$ th mode of  $v_\alpha(\mathbf{x}, t)$ . The equation governing the evolution of the Fourier coefficients is given by

$$\left(\frac{\partial}{\partial t} + \nu k^2\right) \mathbf{u}(\mathbf{k}, t) = \mathbf{W}(\mathbf{k}, t) - i\mathbf{k} \mathcal{F} \left( p(\mathbf{x}, t) + \frac{1}{2} |\mathbf{v}(\mathbf{x}, t)|^2, \mathbf{k} \right) + \mathbf{F}(\mathbf{k}, t), \quad (2.5)$$

where  $\mathcal{F}(a(\mathbf{x}, t), \mathbf{k})$  denotes the Fourier coefficient of the function  $a(\mathbf{x}, t)$  corresponding to wave vector  $\mathbf{k}$ :

$$\mathcal{F}(a(\mathbf{x}, t), \mathbf{k}) = A(\mathbf{k}, t) \quad \text{if} \quad a(\mathbf{x}, t) = \sum_{\mathbf{k}} A(\mathbf{k}, t) e^{i\mathbf{k} \cdot \mathbf{x}}. \quad (2.6)$$

In addition,  $\mathbf{W}(\mathbf{k}, t)$  and  $\mathbf{F}(\mathbf{k}, t)$  denote the  $\mathbf{k}$ th Fourier coefficient of the nonlinearity  $\mathbf{w}(\mathbf{x}, t)$  and forcing  $\mathbf{f}(\mathbf{x}, t)$ , respectively.

In spectral space the pressure term may be eliminated from Eq. (2.5) if use is made of the incompressibility condition. This is equivalent to the well-known practice of solving a Poisson equation for the pressure in physical space formulations [105]. If we multiply Eq. (2.5) by  $\mathbf{k}$ , use the continuity equation in spectral space, i.e.,  $\mathbf{k} \cdot \mathbf{u}(\mathbf{k}, t) = 0$ , and assume that the forcing itself is divergence-free, so that  $\mathbf{k} \cdot \mathbf{F}(\mathbf{k}, t) = 0$ , the pressure term can be written as

$$\mathcal{F}\left(p(\mathbf{x}, t) + \frac{1}{2} |\mathbf{v}(\mathbf{x}, t)|^2, \mathbf{k}\right) = \frac{\mathbf{k} \cdot \mathbf{W}(\mathbf{k}, t)}{ik^2}. \quad (2.7)$$

The equation for the Fourier coefficients of the velocity field (2.5) may now be written as

$$\left(\frac{\partial}{\partial t} + \nu k^2\right) \mathbf{u}(\mathbf{k}, t) = \mathbf{W}(\mathbf{k}, t) - \mathbf{k} \left(\frac{\mathbf{k} \cdot \mathbf{W}(\mathbf{k}, t)}{k^2}\right) + \mathbf{F}(\mathbf{k}, t). \quad (2.8)$$

This may be expressed in a more compact form in terms of the projection operator  $\mathbf{D}$  defined by

$$D_{\alpha\beta} = \delta_{\alpha\beta} - \frac{k_\alpha k_\beta}{k^2}. \quad (2.9)$$

This operator restricts the solution to the space of divergence-free fields, represented by Fourier coefficients  $\mathbf{u}(\mathbf{k}, t)$  that lie in the plane normal to the wave vector  $\mathbf{k}$ . We obtain the governing equation for the desired Fourier coefficients as

$$\left(\frac{\partial}{\partial t} + \nu k^2\right) \mathbf{u}(\mathbf{k}, t) = \mathbf{D}\mathbf{W}(\mathbf{k}, t) + \mathbf{F}(\mathbf{k}, t). \quad (2.10)$$

A more detailed discussion of this spectral approach to the Navier–Stokes equations is available in Ref. [71]. It forms the basis for the numerical treatment that will be specified in the Appendix.

In various applications the dispersion of a passive scalar by a turbulent flow is of central importance. Passive scalar transport may be used to characterize the physical space consequences of multiscale forced turbulence. The governing equation for the evolution of the scalar concentration  $C(\mathbf{x}, t)$  contains advection by the velocity field  $\mathbf{v}(\mathbf{x}, t)$  as well as diffusion. In physical space this may be expressed as

$$\frac{\partial C(\mathbf{x}, t)}{\partial t} + \left(\mathbf{v}(\mathbf{x}, t) \cdot \nabla\right) C(\mathbf{x}, t) = \kappa \nabla^2 C(\mathbf{x}, t), \quad (2.11)$$

where  $\kappa$  is the non-dimensional molecular diffusivity of the scalar. Compared to the dimensionless viscosity in Eq. (2.1) we adopt  $\kappa = \nu / \text{Sc}$  where the Schmidt number  $\text{Sc}$  characterizes the scalar diffusion. Roughly speaking, if  $\text{Sc} > 1$  then the scalar field displays a wider range of dynamically important length scales, compared to the turbulent velocity field, while values  $\text{Sc} < 1$  indicate a comparably smoother scalar field. The equation that governs the development of the Fourier coefficients  $c(\mathbf{k}, t)$  of the scalar field  $C(\mathbf{x}, t)$  can readily be found as

$$\left( \frac{\partial}{\partial t} + \kappa k^2 \right) c(\mathbf{k}, t) = Z(\mathbf{k}, t), \quad \text{where } Z(\mathbf{k}, t) = \mathcal{F} \left( (\mathbf{v}(\mathbf{x}, t) \cdot \nabla) C(\mathbf{x}, t), \mathbf{k} \right). \quad (2.12)$$

The changes in the turbulent transport properties of the flow due to the multiscale forcing can be investigated by considering the evolution of the scalar concentration at different Schmidt numbers. The structure of the left-hand side of Eq. (2.12) is identical to the Navier–Stokes equations in Eq. (2.10). This allows to adopt the same time-stepping method, as will be specified in the Appendix.

To quantify the spectral-space effect of multiscale forcing, and also to be able to concisely formulate the different forcing procedures in the next subsection, we consider the kinetic energy. The equations that govern the Fourier coefficients (2.10) can be written in index notation as

$$\left( \frac{\partial}{\partial t} + \nu k^2 \right) u_\alpha(\mathbf{k}, t) = \Psi_\alpha(\mathbf{k}, t) + F_\alpha(\mathbf{k}, t), \quad (2.13)$$

where  $\Psi_\alpha(\mathbf{k}, t) = D_{\alpha\beta} W_\beta(\mathbf{k}, t)$  is the nonlinear term. Multiplying this equation by the complex conjugate  $u_\alpha^*(\mathbf{k}, t)$  and summing over the three coordinate directions, we obtain the kinetic energy equation

$$\left( \frac{\partial}{\partial t} + 2\nu k^2 \right) E(\mathbf{k}, t) = u_\alpha^*(\mathbf{k}, t) \Psi_\alpha(\mathbf{k}, t) + u_\alpha^*(\mathbf{k}, t) F_\alpha(\mathbf{k}, t), \quad (2.14)$$

where  $E(\mathbf{k}, t) = \frac{1}{2} |\mathbf{u}(\mathbf{k}, t)|^2$  is the kinetic energy in mode  $\mathbf{k}$ . Introducing the notation for the rate of energy transfer  $T(\mathbf{k}, t) = u_\alpha^*(\mathbf{k}, t) \Psi_\alpha(\mathbf{k}, t)$ , the rate of energy injection by the forcing  $T_F(\mathbf{k}, t) = u_\alpha^*(\mathbf{k}, t) F_\alpha(\mathbf{k}, t)$  and the energy-dissipation rate  $\varepsilon(\mathbf{k}, t) = 2\nu k^2 E(\mathbf{k}, t)$ , we can write Eq. (2.14) as

$$\frac{\partial E(\mathbf{k}, t)}{\partial t} = -\varepsilon(\mathbf{k}, t) + T(\mathbf{k}, t) + T_F(\mathbf{k}, t). \quad (2.15)$$



This formulation clarifies that the rate of change of kinetic energy  $E(\mathbf{k}, t)$  is connected with dissipation, expressed by the viscous term  $\varepsilon(\mathbf{k}, t)$ , with transfer to/from different wave numbers, expressed by  $T(\mathbf{k}, t)$ , and with the forcing term  $T_F(\mathbf{k}, t)$ .

The different contributions to the rate of change of the kinetic energy typically act in distinct wave-number regions. The forcing term  $T_F(\mathbf{k}, t)$  is non-zero in the forced modes only. In this paper the collection of forced modes will always contain a low wave-number band corresponding to large-scale forcing of the flow. In addition, possible higher wave-number contributions can be included in  $T_F(\mathbf{k}, t)$ . In contrast, energy dissipation  $\varepsilon(\mathbf{k}, t)$  is defined in the entire spectral space, but it is dynamically important primarily for the high wave-number range, i.e., acting on structures below the dissipation length scale. Finally, the transfer term  $T(\mathbf{k}, t)$  is basic to the development of an energy cascade and is a dominant contribution for wave numbers in an inertial range [71]. In the multiscale forcing cases, we will also introduce forcing generally in the same region as where the transfer  $T(\mathbf{k}, t)$  is dynamically important. Hence, the effects of the multiscale forcing relate directly to the “competition” between the dynamics introduced by the forcing procedure and the “natural” transfer of energy to other modes in the spectrum.

In the formulation of forcing procedures and in the evaluation of the kinetic energy dynamics, one frequently adopts shell-averaging. The basic operation consists of averaging over spherical shells of thickness  $2\pi/L_b$  centered around the origin. The  $n$ th spherical shell is given by  $\frac{2\pi}{L_b}(n - 1/2) < |\mathbf{k}| \leq \frac{2\pi}{L_b}(n + 1/2)$  and will be denoted by  $\mathbb{K}_n$ . Applying shell-averaging to a function  $h(\mathbf{k}, t)$  defined in spectral space we obtain

$$\bar{h}(n, t) = \frac{1}{P_n} \sum_{\mathbb{K}_n} h(\mathbf{k}, t) \quad ; \quad P_n = \sum_{\mathbb{K}_n} 1, \quad (2.16)$$

where  $P_n$  is the number of modes in the  $n$ th shell. Applying the shell-averaging [Eq. (2.16)] to the energy equation (2.15) we end up with

$$\frac{\partial \bar{E}(n, t)}{\partial t} = -\bar{\varepsilon}(n, t) + \bar{T}(n, t) + \bar{T}_F(n, t), \quad (2.17)$$

which indicates that the interpretation of the various contributions to the rate of change of the kinetic energy at mode  $\mathbf{k}$  also applies to the shell-

averaged formulation. In literature it is common to introduce a numerical correction factor when averaging over shells. This is used to compensate for the nonuniform distribution of modes within the discrete spherical shells [30, 57]. We will follow the convention used in Refs. [30, 110, 108] when presenting the energy spectra. This implies that we multiply  $\bar{h}(n, t)$  by a factor  $4\pi n^2$ , which is associated with the “expected number modes” within the discrete shell. The definition of the energy spectrum that we will adopt is given by  $E_n = \left(4\pi n^2/P_n\right) \sum_{\mathbb{K}_n} E(\mathbf{k}, t)$ . Finally, summing Eq. (2.15) over all wave vectors  $\mathbf{k}$  or, equivalently, Eq. (2.17) over all shells yields the evolution equation for the total energy in the system:

$$\frac{d\widehat{E}(t)}{dt} = -\widehat{\varepsilon}(t) + \widehat{T}_F(t) \quad ; \quad \widehat{h}(t) = \sum_n P_n \bar{h}(n, t) = \sum_{\mathbf{k}} h(\mathbf{k}, t), \quad (2.18)$$

where use was made of the fact that the contribution of the transfer term  $T(\mathbf{k}, t)$  is such that it only re-distributes energy over the various modes, which implies that its sum over all wave numbers  $\widehat{T}(t) = 0$ .

Next to spherical shells, it is convenient to introduce spherical wave-number bands that consist of several adjacent shells. We denote the wave-number band that consists of  $\frac{2\pi}{L_b}(m - 1/2) < |\mathbf{k}| \leq \frac{2\pi}{L_b}(p + 1/2)$  by  $\mathbb{K}_{m,p}$ , where  $m \leq p$ . The corresponding average over  $\mathbb{K}_{m,p}$  of a function  $h(\mathbf{k}, t)$  is given by

$$\widetilde{h}^{(m,p)}(t) = \frac{1}{P_{m,p}} \sum_{n=m}^p P_n \bar{h}(n, t) = \frac{1}{P_{m,p}} \sum_{\mathbb{K}_{m,p}} h(\mathbf{k}, t) \quad ; \quad P_{m,p} = \sum_{n=m}^p P_n. \quad (2.19)$$

To complete the computational model, we will next introduce the explicit forcing strategies that will be investigated in this paper.

## 2.2.2 Explicit forcing procedures

Forced turbulence in a periodic box is one of the most basic numerically simulated turbulent flows. It is achieved by applying large-scale forcing to the Navier-Stokes equations. As a result, at sufficiently high Reynolds number the well-known turbulent cascade develops in an inertial range of scales, which are much smaller than the length scale of the forced modes [58, 59, 71]. The statistical equilibrium that is reached is characterized by a balance between the input of energy through the large-scale forcing and the viscous dissipation at scales beyond the Kolmogorov dissipation scale.

Various forcing procedures have been proposed in literature. Generally, if the forcing is restricted to large scales only, the specific details of the procedure do not have such a large effect on the properties of the developing inertial range at sufficiently finer scales. However, since we wish to extend the forcing to act on a wide range of scales simultaneously, including parts of an inertial sub-range, the differences between alternative forcing procedures become more pronounced. Investigating these differences is an essential step toward quantitative modeling of flow through complex gasket structures and forms the main focus of this paper. In this subsection, we will recover the definition and some of the motivation for several characteristic forcing procedures.

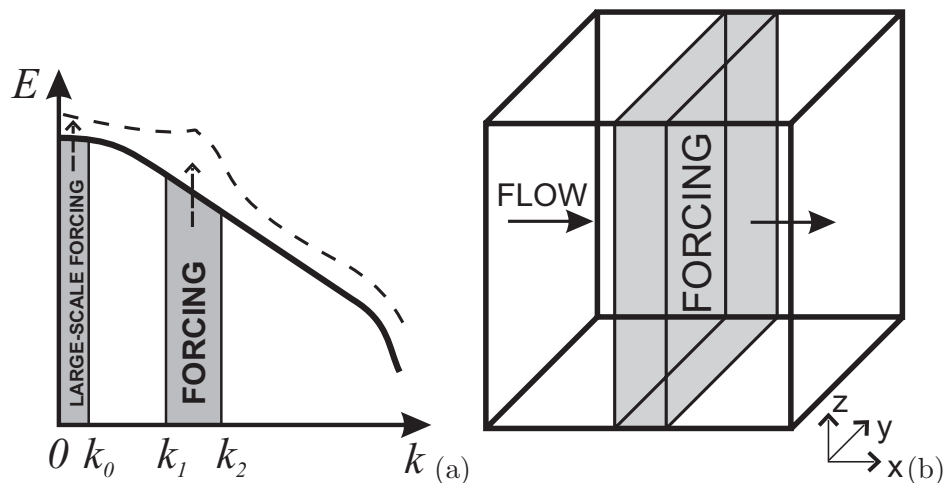


**Fig. 2.2:** Definition of two-band forcing in spectral space (a) and localization of forcing within a slab in physical space (b).

In multiscale forcing, the flow is agitated over a wide range of modes. To investigate the effects of such forcing we will focus on cases in which one additional spherical band of scales is forced, next to the common forcing of the large scales. We consider the general situation as depicted in Fig. 2.2(a). The large scales are in the range  $k \leq k_0$  and an additional band of small scales is defined by  $k_1 < k \leq k_2$ . The forcing method can also incorporate cases in which only part of the domain is occupied by a complex obstruction, as sketched for the case of a slab in Fig. 2.2(b). In fact, by introducing

an “indicator” function  $\Theta(\mathbf{x}, t)$  to locate the complex object within the flow domain ( $\Theta = 0$  outside the region occupied by the object and 1 elsewhere), the forcing can accommodate such spatial localization in a flexible manner. In spectral space, the introduction of  $\Theta(\mathbf{x}, t)$  implies that the forcing term in spectral space is represented by the convolution product of the actual forcing  $F(\mathbf{k}, t)$  and the Fourier transform of the indicator function. However, in the present paper such complications will not be included and we will only consider forcing procedures applied in the entire physical domain.

Forcing procedures may be classified in different ways. We first distinguish forcing schemes that keep the total energy in the collection of forced modes identical to its value in the initial condition. This will be referred to as class ‘A’ forcing procedures. Next, we identify forcing schemes that are characterized by a constant-energy input rate, introduced via the collection of forced modes. This group will be referred to as class ‘B’. In either class of schemes, the flows develop around a well defined statistically stationary state, but time-dependent variations in the total energy and in the energy-input rate may occur.

Apart from a distinction concerning the way energy is introduced into the flow, one may classify forcing schemes as “deterministic” or “stochastic”. Stochastic forcing schemes may introduce an element of uncorrelated randomness, e.g., by restricting the forcing to a random subset of the collection of forced modes every time the forcing is invoked. Several stochastic forcing methods were explored numerically in Refs. [1, 6, 7, 79]. These stochastic procedures were applied to a wide set of inertial-range scales and give rise to a power-law spectrum. The emphasis in these studies was put on the issue of *universality* in turbulent flows, i.e., the dependency of large and small-scale turbulent fluctuations on the adopted forcing mechanism. This issue is also at the heart of this paper. The primary question of locality of the modulation of the energy spectrum can be addressed more directly using deterministic schemes and in this paper we will restrict to these procedures. We next introduce some characteristic forcing schemes in either class ‘A’ or class ‘B’.

### **Class ‘A’: constant energy forcing**

Various methods can be formulated, which are such that the kinetic energy in the forced modes remains constant. The simplest possibility arises by

requiring that  $u_\alpha(\mathbf{k}, t)$  itself remains constant for all  $\mathbf{k}$  in the collection of forced modes. This was first proposed in Ref. [94] and implies for the forcing in spectral space

$$\text{A1 : } F_\alpha(\mathbf{k}, t) = \nu k^2 u_\alpha(\mathbf{k}, t) - \Psi_\alpha(\mathbf{k}, t). \quad (2.20)$$

One readily verifies, using Eq. (2.13), that  $\partial_t u_\alpha(\mathbf{k}, t) = 0$  and in particular this implies that  $\partial_t E(\mathbf{k}, t) = 0$  for each of the forced modes. Hence, also the total kinetic energy contained in all the forced modes stays constant in time. The energy-input rate corresponding to Eq. (2.20) is given by  $T_F(\mathbf{k}, t) = \varepsilon(\mathbf{k}, t) - T(\mathbf{k}, t)$  for each of the forced modes. This input rate may vary considerably in time, as the unsteady flow will lead to a strong time-dependence of the energy transfer  $T$  for the forced modes.

The basic method [Eq. (2.20)] has motivated the formulation of a number of extensions that relax the requirement that the Fourier coefficient is strictly constant. In Ref. [20] the method was modified to require that  $|\mathbf{u}(\mathbf{k}, t)| = \text{const}$ , i.e., equal to its initial value, for the forced modes. This allows for the possibility that the phases of the Fourier coefficients may evolve in time. The corresponding forcing is given by

$$F_\alpha(\mathbf{k}, t) = \left( \nu k^2 - \frac{T(\mathbf{k}, t)}{2E(\mathbf{k}, t)} \right) u_\alpha(\mathbf{k}, t) = (\varepsilon(\mathbf{k}, t) - T(\mathbf{k}, t)) \frac{u_\alpha(\mathbf{k}, t)}{2E(\mathbf{k}, t)}. \quad (2.21)$$

One may readily verify that this implies  $\partial_t E(\mathbf{k}, t) = 0$  for the forced modes. Forcing expressed in Eq. (2.20) or Eq. (2.21) was found to yield quite large fluctuations in the energy-input rate [101].

Typically, the forced modes are ordered according to the wave-number shell to which they belong. A shell-oriented simplification of Eq. (2.21) was proposed [56, 57]:

$$F_\alpha(\mathbf{k}, t) = (\bar{\varepsilon}(k, t) - \bar{T}(k, t)) \frac{u_\alpha(\mathbf{k}, t)}{2E(\mathbf{k}, t)}. \quad (2.22)$$

This forcing also preserves the total kinetic energy in the forced modes. The three forcing procedures [Eqs. (2.20), (2.21) and (2.22)] are quite comparable, both in terms of their fluid-physics motivation and in terms of their turbulent flow predictions. Therefore, we will only present actual simulation

results obtained with Eq. (2.20), which are quantitatively representative for the other two forcing procedures in this group.

The forcing methods described so far preserve the kinetic energy that is contained in the collection of forced modes. However, considerable variations in the total energy in the system can still arise. The reverse can also be realized, i.e., forced turbulence in which the total kinetic energy in the system is constant, but the energy in different modes may vary in time. For this purpose, the forcing should not be formulated in terms of quantities related to individual modes or shell-averaged values, but rather contain averages over all modes [38, 67]. The case of forcing in a single shell with  $P$  modes can readily be specified. Specifically, if we replace the shell-average  $\overline{(\cdot)}$  in the amplitude factor in Eq. (2.22) by the average over all modes  $\widehat{(\cdot)}$  and use the fact that  $\widehat{T} = 0$ , we obtain the forcing

$$\text{A2: } F_\alpha(\mathbf{k}, t) = \frac{\widehat{\varepsilon}(t) u_\alpha(\mathbf{k}, t)}{P \ 2E(\mathbf{k}, t)}. \quad (2.23)$$

The A2-forcing implies an energy-input rate  $\widehat{T}_F = \widehat{\varepsilon}(t)$  and thus by Eq. (2.18)  $d\widehat{E}/dt = 0$ . This method corresponds exactly to the negative viscosity procedure used to maintain quasi-steady turbulence direct numerical simulations results reported in Refs. [52, 107, 50, 54]. Extension of A2-forcing to multiple shells can be realized in a number of ways. This will be described in more detail momentarily. A2-forcing will be compared to A1-forcing in the next section.

### **Class ‘B’: constant-energy input rate forcing**

Next to forcing methods that can be associated with constant energy, one may define forcing procedures in which the total energy input rate  $\widehat{T}_F$  is constant. We first present such forcing methods with reference to a single band of forced modes. The way in which the energy input is distributed over several bands will be specified afterwards.

A central example in the class of constant-energy input rate forcing methods was presented in Ref. [36]. Changing  $\widehat{\varepsilon}(t)$  in Eq. (2.23) into the constant-energy input rate  $\varepsilon_w$ , the corresponding forcing term may be written as

$$\text{B1: } F_\alpha(\mathbf{k}, t) = \frac{\varepsilon_w u_\alpha(\mathbf{k}, t)}{P \ 2E(\mathbf{k}, t)}. \quad (2.24)$$

The energy-input rate is found to be  $\widehat{T}_F(t) = \varepsilon_w$ , as desired by construction. The total energy in the system is no longer constant but governed by  $d\widehat{E}(t)/dt = -\widehat{\varepsilon}(t) + \varepsilon_w$ , which implies that the statistically stationary state that develops will show a dissipation rate that fluctuates about  $\varepsilon_w$ . This type of forcing was also studied in Refs. [78, 19, 110]. Further extensions of the basic forcing procedure [Eq. (2.24)] can be proposed in which an extra factor  $k^{-q}$ ;  $q > 0$  arises in the definition of  $F_\alpha$ . Such an extra factor implies that the forcing of higher wave-number shells can be made to correspond to a specific shape (usually  $k^{-5/3}$  to more directly “impose” Kolmogorov turbulence). These forcing procedures will not be considered in this paper; for further details see Refs. [21, 80].

Similar to A-forcing methods, one may formulate related procedures that are defined in terms of shell-averaged quantities. For example, analogous to Eq. (2.22), we may replace  $E(\mathbf{k}, t)$  in Eq. (2.24) by  $\overline{E}(n, t)$  to define the forcing of modes in the  $n$ th shell. This type of forcing was found to yield basically the same results as those based on Eq. (2.24) and will not be presented explicitly in the rest of this paper.

The final forcing procedure that we will include in this paper was proposed recently in Ref. [70]. It was motivated as a model of flow through a fractal gasket which functions as a multiscale stirrer. This particular forcing may be associated with a constant-energy input rate for the entire system. We modified the original forcing procedure slightly and considered in particular

$$\text{B2 : } F_\alpha(\mathbf{k}, t) = \frac{\varepsilon_w k^\beta}{\sum_{\mathbf{k} \in \mathbb{K}} \sqrt{2E(\mathbf{k}, t)} k^\beta} e_\alpha(\mathbf{k}, t), \quad (2.25)$$

where  $\mathbb{K}$  denotes the set of forced modes. In this formulation, the complexity of the object is parameterized by the exponent  $\beta$  that is related to the fractal dimension  $D_f$  of the object through  $\beta = D_f - 2$ . The vector  $\mathbf{e}(\mathbf{k}, t)$  has the form:

$$\mathbf{e}(\mathbf{k}, t) = \frac{\mathbf{u}(\mathbf{k}, t)}{|\mathbf{u}(\mathbf{k}, t)|} + i \frac{\mathbf{k} \times \mathbf{u}(\mathbf{k}, t)}{|\mathbf{k}| |\mathbf{u}(\mathbf{k}, t)|}. \quad (2.26)$$

that contains a part in the direction of  $\mathbf{u}$  and a part that is perpendicular to  $\mathbf{u}$ .

Since  $u_\alpha^* e_\alpha = |\mathbf{u}| = \sqrt{2E(\mathbf{k}, t)}$  we find for the energy-input rate

$$T_F(\mathbf{k}, t) = \varepsilon_w \frac{k^\beta \sqrt{2E(\mathbf{k}, t)}}{\sum_{\mathbf{k} \in \mathbb{K}} k^\beta \sqrt{2E(\mathbf{k}, t)}}. \quad (2.27)$$

In contrast to B1-forcing in which the energy-input rate is constant in time for each of the forced modes separately, this “fractal forcing” procedure only implies a constant-energy input rate for the entire system. In fact, after summation over all forced modes the total energy-input rate is found to be equal to  $\widehat{T}_F(t) = \varepsilon_w$ . Correspondingly, we find for the evolution of the total kinetic energy  $d\widehat{E}/dt = -\widehat{\varepsilon}(t) + \varepsilon_w$ , i.e., identical as obtained before for B1-forcing. In the original formulation in Ref. [70] the energy-input rate  $\varepsilon_w$  was replaced by the total dissipation rate  $\widehat{\varepsilon}(t)$ , which implies that  $\widehat{E}$  is constant in time.

So far, the B1- and B2-forcing methods were defined with reference to a single band of modes. This band was assumed to contain  $P$  modes and was identified by  $\mathbb{K}$ . The total energy-input rate  $\varepsilon_w$  was available to this band. In case more bands are forced simultaneously, the way the energy-input rate is divided over the individual bands, and among the modes within each band, needs to be specified. For two forced bands  $\mathbb{K}_{m_1, p_1}$  and  $\mathbb{K}_{m_2, p_2}$  with  $P_{m_1, p_1}$  and  $P_{m_2, p_2}$  modes respectively, such a partitioning involves two steps. First, a fraction  $\varepsilon_{w,1} = a\varepsilon_w$  of the total energy-input rate is “allocated” to the first band and the remainder  $\varepsilon_{w,2} = (1-a)\varepsilon_w$  is used in the forcing of the second band ( $0 \leq a \leq 1$ ). Second, we divide the energy-input rate that is available for each band equally over all modes in the corresponding band. As an example, two-band B1-forcing may be defined as

$$\begin{aligned} \text{B1: } F_\alpha(\mathbf{k}, t) &= \frac{a\varepsilon_w}{P_{m_1, p_1}} \frac{u_\alpha(\mathbf{k}, t)}{2E(\mathbf{k}, t)} ; & k \leq k_0 \\ &= \frac{(1-a)\varepsilon_w}{P_{m_2, p_2}} \frac{u_\alpha(\mathbf{k}, t)}{2E(\mathbf{k}, t)} ; & k_1 < k \leq k_2 \\ &= 0 ; & \text{otherwise.} \end{aligned} \quad (2.28)$$

The two-band formulation of B2-forcing can be specified analogously, replacing  $\varepsilon_w$  by either  $a\varepsilon_w$  or  $(1-a)\varepsilon_w$  and  $\mathbb{K}$  by  $\mathbb{K}_{m_1, p_1}$  or  $\mathbb{K}_{m_2, p_2}$ , respectively. Extending A2-forcing to more bands can be done in a similar way



in which a fraction  $a\widehat{\varepsilon}(t)$  is associated with the large-scale band and the remainder with the second band. The specific choice of  $P_{m_1,p_1}$  and  $P_{m_2,p_2}$  above implies that the energy is equally distributed between all modes within a forced band. We can go one step further and require the equal distribution of  $\varepsilon_w$  over the forced shells contained in the bands. This implies changing  $P_{m_1,p_1}$  and  $P_{m_2,p_2}$  into the number of modes  $P_n$  for each forced shell. Extension to more forced bands can be formulated analogously. For completeness, the numerical method that is used in the reported simulations, and its validation, are specified in the Appendix.

In the next section we turn to the effects that different multiscale forcing procedures have on the developing turbulent flow. We will focus in particular on the modifications that arise in the kinetic energy spectrum.

## 2.3 Modulated cascading by broadband forcing

The explicit forcing in different wave-number bands can have a strong effect on the developing turbulent flow. We discuss the modifications of the energy spectrum arising from “constant energy” (class ‘A’) or “constant-energy input rate” (class ‘B’) procedures. The various forcing strategies will be shown to qualitatively correspond to each other, provided the total dissipation rate  $\varepsilon_w$  and the spectral energy distribution are commensurate for the different class ‘A’ and ‘B’ forcing strategies. We will specify this interrelation in more detail momentarily. As point of reference, we will first turn our attention to forcing of the large scales only. Subsequently, we consider two-band forcing and investigate in particular the effects of variation of the strength and location of the small-scales band on the developing flow.

In the sequel, we consider time-averaged properties of the developing turbulent flow defined by

$$\langle h \rangle_t = \lim_{t \rightarrow \infty} \frac{1}{t - t_0} \int_{t_0}^t h(\tau) d\tau \approx \frac{1}{\mathcal{T} - t_0} \int_{t_0}^{\mathcal{T}} h(\tau) d\tau, \quad (2.29)$$

where  $\mathcal{T}$  is sufficiently large. In all cases  $t_0 = 5$  in order to allow the averaging-process to start from a properly developed quasistationary state. The averaging is continued up to  $\mathcal{T} = 25$ , which corresponds to approximately 40 eddy-turnover times. This was found to provide an accurate

representation of the long-time averages, leading to relative errors below 5%, measured in terms of the ratio of the standard deviation and the mean signal. This procedure was applied to obtain the time-averaged kinetic energy spectra as well, which are very effective for monitoring changes in the kinetic energy dynamics due to the forcing.

### 2.3.1 Large-scale forcing

To create a point of reference, we first consider forced turbulence in which energy is introduced to the system only in the first shell  $\mathbb{K}_{1,1}$ . We adopt  $k_0 = 3\pi$  referring to Fig. 2.2(a) and force all 18 modes inside this band. The computational Reynolds number  $\text{Re} = 1061$  and the size of the computational domain  $L_b = 1$ . The spatial resolution was taken to be  $128^3$ , which provides ample resolution of these cases, similar to what was established in the Appendix.

In order to be able to quantitatively compare results obtained with the different forcing strategies, care should be taken of properly “assigning” a level for the energy-dissipation rate and the spectral energy distribution. For this purpose, we may consider simulations with the A2-method to be central in the sense that the other three forcing strategies may be specified with reference to it. In fact, if we generate an initial condition with a certain total kinetic energy, then A2-forcing yields an evolving flow that becomes statistically stationary after some time, while maintaining the same level of total energy. The A2-forced simulation can be used to specify the “corresponding” class-B forcing strategies. In fact, the constant dissipation rate  $\varepsilon_w$  in class ‘B’ forcing is taken equal to the time-average value of the dissipation rate that is found from the A2-forced simulation, i.e., we adopt  $\varepsilon_w = \langle \hat{\varepsilon} \rangle_t$ . This procedure was adhered to in all cases presented in this section. Finally, in the developed stages of either these A2- or B-forced flows, any instantaneous solution may be used to arrive at a full specification of the “corresponding” A1-forcing. The actual choice of this instantaneous solution is arbitrary. However, when comparing simulations based on A1-forcing that adopt different realizations of the turbulent flow field, we observed that the statistical properties of all these A1-forced cases were the same.

The evolution of the total kinetic energy  $\hat{E}(t)$  and energy-dissipation rate  $\hat{\varepsilon}(t)$  is shown in Fig. 2.3. As initial condition for the A2- and B-forced simula-

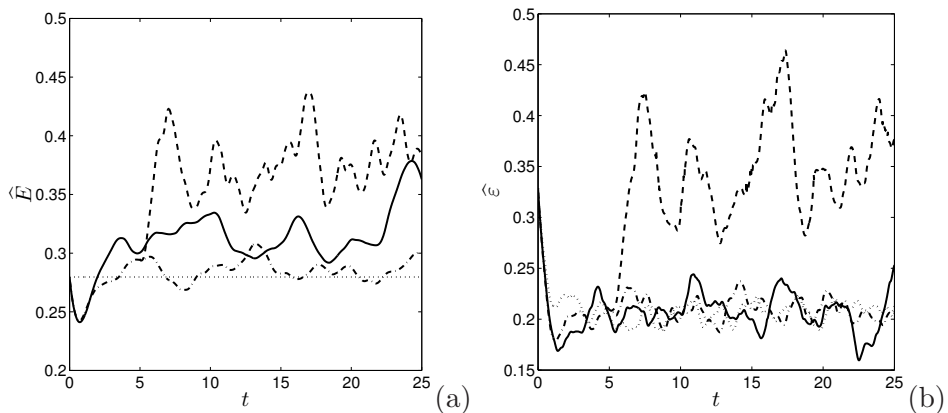


**Fig. 2.3:** The evolution of the total kinetic energy  $\widehat{E}$  (a) and energy-dissipation rate  $\widehat{\varepsilon}$  (b) for the large-scale forcing: A1 (dashed), A2 (dotted), B1 (dash-dotted), B2 (solid).

tions, we adopted the velocity field obtained at  $t = 0.5$  from the decaying homogeneous turbulence simulation discussed in the Appendix. To be able to qualitatively compare with the A1-forced flow at a similar energetic level we took as initial condition the solution from B1-forcing at  $t = 5$ . The total kinetic energy is seen to fluctuate around its long-time mean value (of course, apart from A2-forcing). As can be seen, the system rapidly develops into a statistically stationary state characterized by the input of energy, its transfer to smaller scales and dissipation in the viscous range. In A1-forcing the Fourier coefficients in the forced band are all kept constant, i.e., equal to their initial values. The energy in the system fluctuates very significantly, which was considered a disadvantage of this forcing in Ref. [30]. The energy and dissipation levels in A1-forcing differ considerably from those obtained with the other forcing strategies. To compare A2-forcing with B-forcing, the energy-dissipation rate was taken as  $\varepsilon_w = \langle \varepsilon \rangle_t \cong 0.2$ . The total kinetic energy for B1-forcing is seen to fluctuate around the constant value associated with A2-forcing. A similar impression is observed when use is made of the fractal B2-forcing in which the fractal dimension of the stirrer was taken equal to  $D_f = 2.6$  [70], which corresponds to an exponent  $\beta = 3/5$  in Eq. (2.25).

In general, when applied to the largest scales only, all forcing procedures mentioned in subsection 2.2.2 yield similar results. As a further example, the tails of the time-averaged spectra were found to be virtually identical to each other, which indicates that the properties of the smaller turbulent length scales are not very strongly dependent on the details of the specific forcing. This was also established by various other quantities that were investigated. Specifically, the Taylor-Reynolds number  $R_\lambda$  for the simulated cases was seen to fluctuate in the range between  $\approx 50$  up to  $\approx 60$  for all methods. The time-averaged value of the skewness was also investigated and found to be very close to 0.5. This indicates that a well developed isotropic flow was attained [3].

### 2.3.2 Two-band forcing

In the simulations that adopt two-band forcing we consider situations in which we introduce energy into the system in a band consisting of four shells, next to the already described large-scale forcing in the first shell. We first compare the different class ‘A’ and ‘B’ forcing strategies, within this two-band setting. As second, forced band we consider  $\mathbb{K}_{17,20}$ . This band corresponds to  $k_1 = 33\pi$  and  $k_2 = 41\pi$  in Fig. 2.2(a) and contains in total 17284 different modes that are all explicitly forced. The comparison of the different forcing strategies shows that the flow predictions are qualitatively comparable. Subsequently, we therefore focus on the B2-forcing strategy and investigate the effects arising from changes in the strength or the location of the second forced band.

Forcing of a second band implies that we need to additionally specify how the energy input is distributed over the bands, the shells within the bands and, finally, the modes within the shells. The specification of the A2-forcing requires the fraction of the energy input that is allocated to the different bands. We consider the case in which  $a = 1/5$  in Eq. (2.28), which corresponds to equi-partitioning of the energy input over the five shells that are forced. The forcing within the second band is further specified by assigning an equal energy-input rate to each of the four shells contained in it. Finally, each of the modes in a particular shell  $n$  receives an equal share of the energy input to that shell, taking the number  $P_n$  of modes in the particular shell into account. To compare the ‘A’ with ‘B’ forcing strategies we adopt the same method as above for specifying the parameter  $\varepsilon_w$ .

Specifically, the total energy injection for the ‘B’ methods was given as  $\varepsilon_w = \langle \hat{\varepsilon} \rangle_t \cong 1$ , in terms of the time-average of the total dissipation rate in the A2-forcing. Moreover, the same equi-partitioning of the energy input as in A2-forcing was adopted. Finally, the A1-forcing is derived from the field that was obtained at  $t = 5$  with the B1-forcing. We verified that the statistical properties of the A1-forced flow are insensitive to the particular choice of initial field used to define this forcing method.

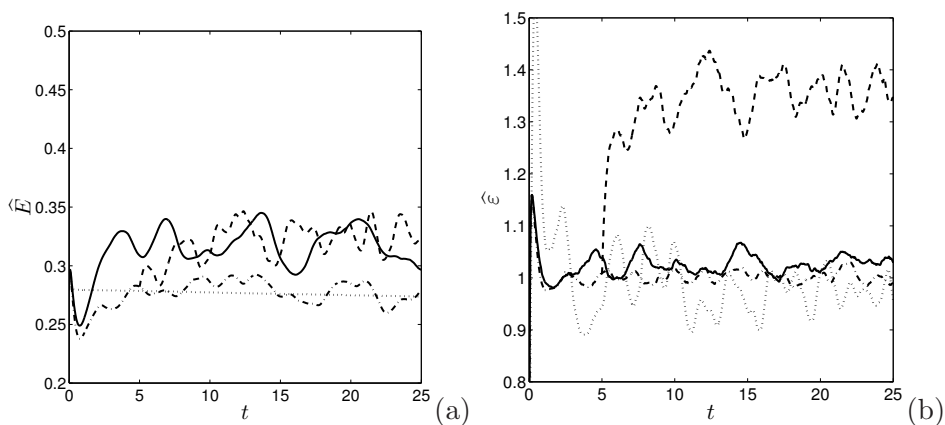


**Fig. 2.4:** The evolution of the total kinetic energy  $\hat{E}$  (a) and energy-dissipation rate  $\hat{\varepsilon}$  (b) for two-band forcing: A1 (dashed), A2 (dotted), B1 (dash-dotted), B2 (solid).

As may be noticed by comparing Fig. 2.3 with Fig. 2.4, the two-band forcing leads to a strong increase in the total energy-dissipation rate, while the total kinetic energy present in the flow is quite unaffected by the second forced band. The increase in the dissipation rate is particularly strong for A1-forcing. Hence, the high- $k$  forcing changes mainly the *distribution* of energy over the scales and not so much the actual energy content. By changing the strength and location of the forcing, we have the possibility to control, and to some extent manipulate the way the energy is distributed and hence indirectly influence the large- and small-scale transport properties of the flow. We turn to this aspect next, by focusing explicitly on the kinetic energy spectrum.

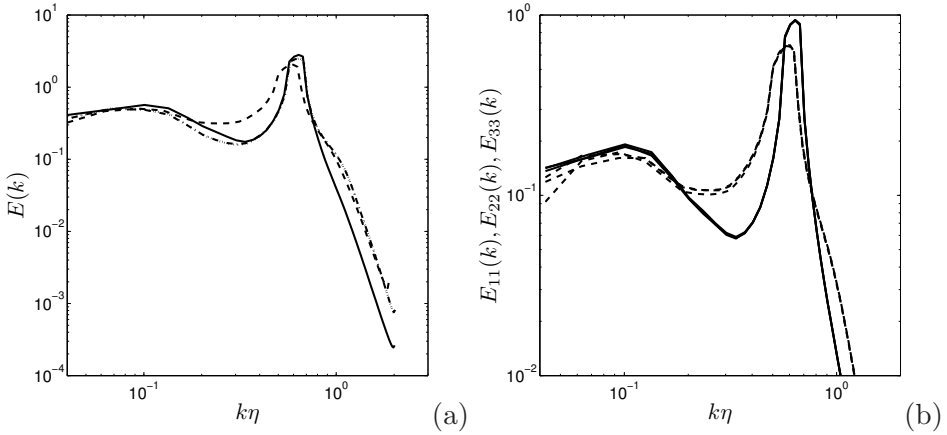


**Fig. 2.5:** (a) Compensated energy spectrum for two-band forced turbulence ( $k \leq 3\pi$  and  $33\pi < k \leq 41\pi$ ) with different methods: A1 (dashed), A2 (dotted), B1 (dash-dotted), B2 (solid). (b) Compensated energy co-spectra  $E_{11}$ ,  $E_{22}$ ,  $E_{33}$  for the A1- and B2-forcing methods. All three curves obtained with B2 are found to collide (solid), while the three curves found with A1 differ at the large scales (dashed).

The compensated kinetic energy spectra  $E(k) = \langle \widehat{\varepsilon} \rangle_t^{-2/3} k^{5/3} \langle E_k \rangle_t$  that are obtained with the different two-band forcing methods are collected in Fig. 2.5(a). The modifications in the spectrum, relative to the case of large-scale forcing only, are localized primarily in the region close to the forced band. All forcing methods are seen to yield qualitatively quite similar results. Next to the expected modifications near the explicitly forced band, we observe that the two-band forcing also affects a much wider set of larger scale modes. In fact, a significant depletion of the kinetic energy in a range of scales “ahead of” the forced region, is readily appreciated. This indicates that the agitation of a small band of modes can induce large changes in a rather wide part of the spectrum, which further characterizes the type of turbulence-control that one may achieve with explicit forcing.

Some of the forcing methods induce a low level of anisotropy in the large-scale turbulence fluctuations. In Fig. 2.5(b) we show the energy co-spectra  $E_{11}$ ,  $E_{22}$ ,  $E_{33}$  for the A1 and B2 forcing methods. In case of perfect isotropy, these co-spectra should coincide. The strong energy oscillations observed earlier in conjunction with the A1 forcing method are seen to be also related

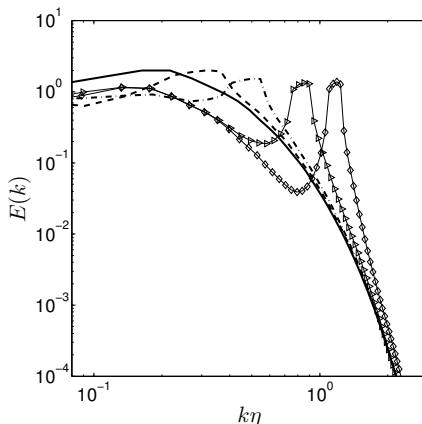


**Fig. 2.6:** Compensated energy spectrum for two-band forced turbulence with the B2-method and the same energy inputs  $\varepsilon_{w,1} = \varepsilon_{w,2} = 0.15$  to the  $k \leq 3\pi$  band and various locations of the second band:  $9\pi < k \leq 17\pi$ ,  $17\pi < k \leq 23\pi$ ,  $33\pi < k \leq 41\pi$ ,  $49\pi < k \leq 57\pi$  (dashed, dash-dotted,  $\triangleright$ ,  $\diamond$ ). The spectrum obtained with large-scale forcing at  $\varepsilon_w = 0.15$  in  $k \leq 3\pi$  band (solid).

to some anisotropy at the largest scales of motion. Such anisotropic energy distributions at large scales may affect the small-scale statistics as was noticed in various numerical experiments, e.g., Refs. [92, 8, 64]. Other forcing methods (e.g., B2-forcing) were not found to induce significant anisotropy at the largest scales.

We next turn to the second part of this section and consider the effects of varying the spectral support and the strength of the second forced band. The qualitative similarity of the different two-band forcing methods as seen in Fig. 2.5 allows to concentrate on only one of the forcing methods. We adopt B2-forcing in the sequel. In Fig. 2.6 we illustrate the effect of variation of the spectral support of the second band. Relative to the case of large-scale forcing only, we observe that the tails of the spectra are quite unaffected. However, the injection of energy in the second band is seen not only to increase the energy in the forced scales but also to deplete the energy in all the larger scales. Moreover, the “up-scale” effect of energy depletion is more pronounced in case the second band is moved toward smaller scales.

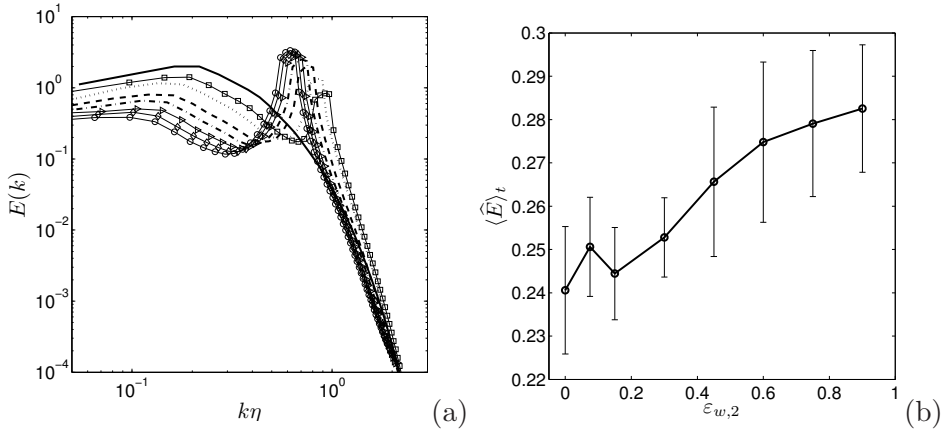


**Fig. 2.7:** (a) Compensated energy spectrum for two-band forced turbulence with the B2-forcing method and energy-input rate  $\varepsilon_{w,1} = 0.15$  in  $k \leq 3\pi$  band for different strengths of forcing in the  $33\pi < k \leq 41\pi$  band:  $\varepsilon_{w,2} = 0.075, 0.15, 0.30, 0.45, 0.60, 0.75, 0.90$  ( $\square$ , dotted, dashed, dash-dotted,  $\triangleright$ ,  $\diamond$ ,  $\circ$ ). Large-scale forcing with  $\varepsilon_w = 0.15$  in the  $k \leq 3\pi$  band is denoted by the solid line. (b) Corresponding time-averaged total kinetic energy with standard deviations.

The control over the flow that is available with two-band forcing is examined further by investigating the effects of varying the strength of the forcing in the second band. We kept the energy input rate for the first  $k \leq 3\pi$  band equal to  $\varepsilon_w = 0.15$  and varied the strength of forcing in the second  $33\pi < k \leq 41\pi$  band adopting  $\varepsilon_w = 0.075 \dots 0.90$ . The corresponding compensated energy spectra from these simulations are shown in Fig. 2.7(a). We observe that a higher energy-input rate in the second band leads to a more pronounced peak in the spectrum that shifts to lower values of  $k\eta$  with increasing  $\varepsilon_w$  of the second band. Simultaneously, the value of  $E(k)$  decreases for the low- $k$  modes with increasing  $\varepsilon_w$ . This forcing of the second band allows to quite independently control the spectrum, at roughly the same total energy content in the flow. In fact, variation of  $\varepsilon_w$  of the second band by a factor of about 10 is seen to lead to a comparably strong increase in the peak value of the spectrum while the total energy level  $\langle \hat{E} \rangle_t$  is increased by only  $\approx 15\%$  as seen in Fig. 2.7(b).



We also investigated properties of the simulated turbulence in case forcing is applied to the high- $k$  range only. In this way, we can separately appreciate some of the backscatter of energy in a 3D turbulent flow. Such backscatter is known to be particularly important in two dimensions, where the inverse energy cascade mechanism is responsible for a significant transfer of energy to the larger scales [9]. We found that forcing in the high- $k$  band only, corresponds to a strongly reduced turbulence intensity, e.g., expressed in a significantly reduced Taylor Reynolds number. The *fraction* of the energy that is backscattered appears quite independent of whether or not the large scales are also explicitly forced. Studying the energy transfer (see, e.g., Ref. [71]), the range of scales that is primarily affected by the high- $k$  forcing was found insensitive to adding large scale forcing or not. More detailed investigations are needed to reveal the properties of energy backscatter in 3D. This requires a separate study and we will not consider this issue further in this paper.

In the next section we will examine how the changes in the flow properties due to the two-band forcing in *spectral space* influence the *physical space* mixing efficiency of a passive scalar.

## 2.4 Small and large scale mixing efficiency

The consequences of explicit broadband forcing not only express themselves in modulated energy cascades. The mixing properties of the evolving turbulent flow in physical space also depend significantly on the forcing that is applied. In this section we quantify the mixing efficiency by monitoring geometric properties of evolving level sets of an embedded passive scalar. The numerical integration method that is used to determine these level set properties is described in subsection 2.4.1. The ensemble-averaged simulation results are discussed in subsection 2.4.2; we establish to what extent the two-band forcing can be used to control the maximal rate of mixing and the total accumulated degree of mixing.

### 2.4.1 Level set evaluation to quantify mixing

To illustrate and quantify the influence of two-band forcing on the turbulent dispersion of a passive scalar field we analyze the evolution of basic geometric properties of its level sets. As a result of the turbulent flow these

level sets become highly distorted and dispersed across the flow domain. Specifically, we concentrate on the surface area and the wrinkling of these level sets. We adopt a specialized integration method to determine these geometric properties, as developed in Ref. [33]. This method is based on the Laplace transform and avoids the explicit construction and integration over the complex and possibly fragmented scalar level sets. With this method an accurate and efficient evaluation of the evolving mixing efficiency can be achieved, which allows to quantify the increased complexity of the flow in relation to the two-band forcing that is used.

Basic geometric properties of a level set  $S(a, t) = \{\mathbf{x} \in \mathbb{R} \mid C(\mathbf{x}, t) = a\}$  of the scalar  $C(\mathbf{x}, t)$  may be evaluated by integrating a corresponding “density function”  $g$  over this set. In fact, we have

$$I_g(a, t) = \int_{S(a, t)} dA g(\mathbf{x}, t) = \int_V d\mathbf{x} \delta(C(\mathbf{x}, t) - a) |\nabla C(\mathbf{x}, t)| g(\mathbf{x}, t), \quad (2.30)$$

where the volume  $V$  encloses the level set  $S(a, t)$  [68]. Setting  $g(\mathbf{x}, t) = 1$ ,  $g(\mathbf{x}, t) = \nabla \cdot \mathbf{n}(\mathbf{x}, t)$  or  $g(\mathbf{x}, t) = |\nabla \cdot \mathbf{n}(\mathbf{x}, t)|$ , we can determine the global surface area, curvature or wrinkling of  $S(a, t)$  respectively. Here  $\mathbf{n}(\mathbf{x}, t) = \nabla C(\mathbf{x}, t) / |\nabla C(\mathbf{x}, t)|$  is a unit normal vector, locally perpendicular to the level set. The divergence of this vector field is directly related to the local curvature of the level set.

We will focus on the evolution of the surface area  $A$  and the wrinkling  $W$ . The scalar  $C$  is scaled to be between 0 and 1; we will primarily consider the level set  $a = 1/4$ . In particular we monitor

$$\vartheta_A(a, t) = \frac{I_A(a, t)}{I_A(a, 0)} \quad ; \quad \vartheta_W(a, t) = \frac{I_W(a, t)}{I_W(a, 0)}. \quad (2.31)$$

By determining  $\vartheta_A$  and  $\vartheta_W$  we may quantify the rate at which surface area and wrinkling develop, the maximal values that are obtained and the time-scale at which these are achieved. The corresponding cumulative effects are given by

$$\zeta_A(a, t) = \int_0^t \vartheta_A(a, \tau) d\tau \quad ; \quad \zeta_W(a, t) = \int_0^t \vartheta_W(a, \tau) d\tau. \quad (2.32)$$

These cumulative measures express the total surface area and wrinkling that has developed in the course of time. In particular applications, e.g.,

involving combustion in diffusion flames, the cumulative surface area and wrinkling express the total “chemical processing capacity”. Here, we will determine these cumulative effects in order to characterize the different two-band forcing procedures.

To establish the influence of forcing on turbulent mixing properties we simulated the spreading of a passive tracer at Schmidt number  $Sc = 0.7$ . The simulations were started from a spherical tracer distribution of radius  $r = 3/16$ . The scalar concentration was set equal to 1 inside this sphere and 0 outside. A localized Gaussian smoothing of this  $C$ -distribution was applied near the edge of the initial sphere to avoid resolution problems. The fractal forcing B2-procedure as defined in Eq. (2.25) was adopted. We performed numerical simulations in which the energy-input rate  $\varepsilon_w$  and the spectral support of this two-band forcing were varied.

As point of reference we adopted large-scale forcing in the  $\mathbb{K}_{1,1}$  shell with an energy-injection rate  $\varepsilon_w = 0.6$ . The resolution requirements were satisfactorily fulfilled:  $k_{\max}\eta$  ranges from 2.3 to 3.5 using a resolution in the range  $128^3 - 192^3$  grid cells. For the passive scalar these resolutions correspond to  $k_{\max}\eta_{OC}$  in the range from 3 to 4.5, where  $\eta_{OC}$  is the Obukhov-Corrsin scale [104]. To study the influence of two-band B2-forcing we applied supplementary forcing either in a region situated near the largest scales of the flow, i.e.,  $\mathbb{K}_{5,8}$  or further separated, i.e.,  $\mathbb{K}_{13,16}$ . In case two bands are forced, the energy-input rate for the  $\mathbb{K}_{1,1}$  shell is  $\varepsilon_{w,1} = 0.15$ , while the second band is forced using  $\varepsilon_{w,2} = 0.45$ . In this way the total energy level is kept at comparable levels in the different cases. A qualitative impression of the effect of these forcing procedures may be observed from the snapshots shown in Fig. 2.8. The velocity and passive scalar display considerably more small-scale features in case of two-band forcing, particularly in case of high- $k$  forcing. To quantify this qualitative impression we apply the level set analysis discussed above. The results will be presented in the next subsection.

## 2.4.2 Surface area and wrinkling

In this subsection, we compare instantaneous and accumulated mixing properties for large-scale forcing and different two-band forcing. The total energy-input rate to the flow is kept constant at 0.6; a fraction  $\varepsilon_{w,1}$  is allocated to the first shell and  $\varepsilon_{w,2}$  to the second band such that  $\varepsilon_{w,1} + \varepsilon_{w,2} = 0.6$

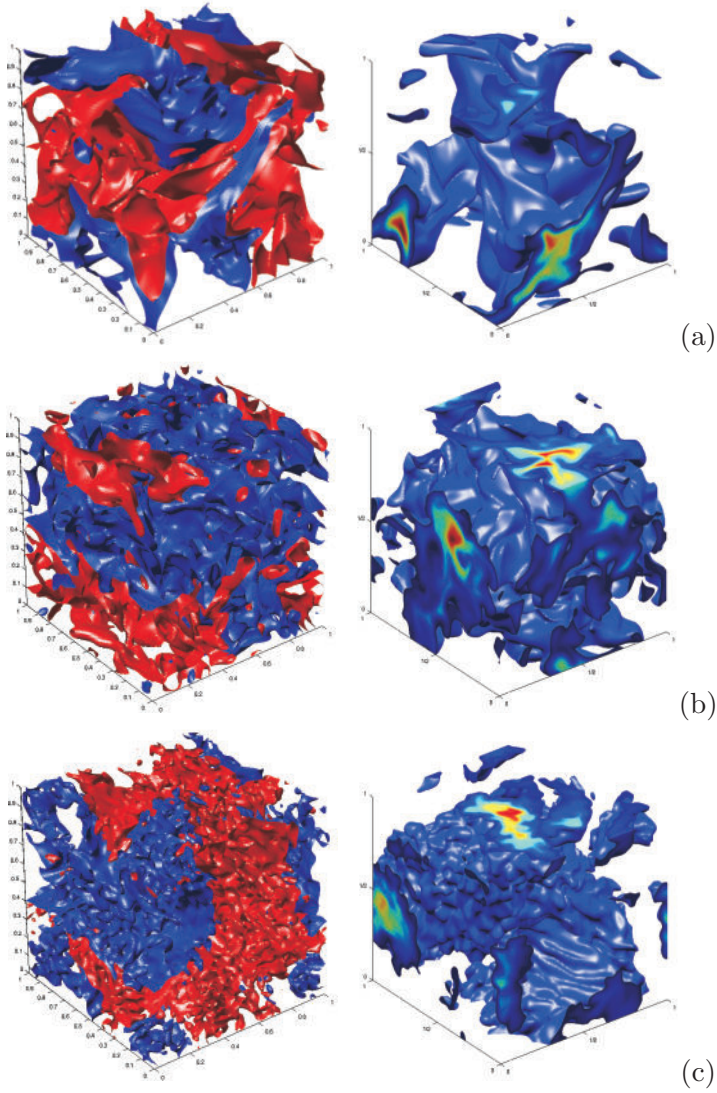


**Fig. 2.8:** Snapshot of vertical velocity field iso-surfaces (left) and passive scalar concentration (right) at  $t = 0.5$  for large-scale forcing  $\mathbb{K}_{1,1}$  with  $\varepsilon_w = 0.6$  (a), or with  $\varepsilon_{w,1} = 0.15$  in the first shell and complementary forcing  $\varepsilon_{w,2} = 0.45$  in  $\mathbb{K}_{5,8}$  (b) or  $\mathbb{K}_{13,16}$  (c). In the velocity field snapshots the red iso-surface corresponds to  $u_2 = 0.2$  and the blue iso-surfaces to  $u_2 = -0.2$ . The iso-surface at  $C = 0.25$  is shown for the passive scalar.

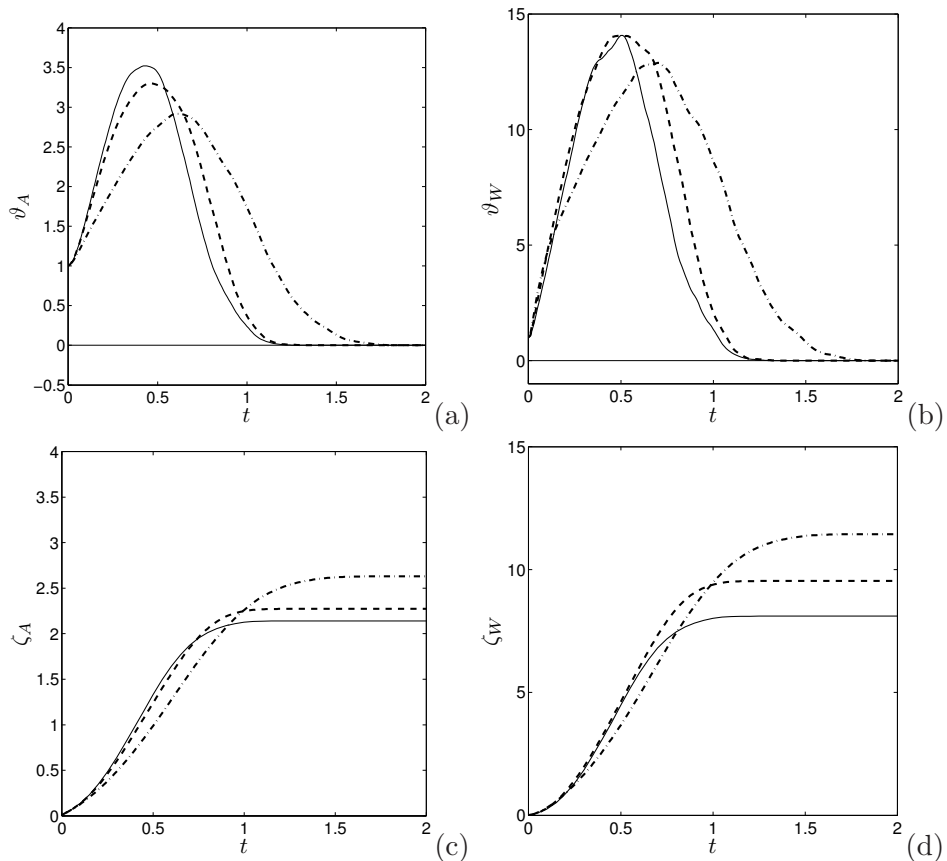


**Fig. 2.9:** Evolution of decaying passive scalar growth parameters: a) surface area  $\vartheta_A$ , b) wrinkling  $\vartheta_W$ , c) accumulated surface area  $\zeta_A$ , d) accumulated wrinkling  $\zeta_W$ . Large-scale forcing  $\mathbb{K}_{1,1}$  with  $\varepsilon_w = 0.60$  (solid) and complementary two-band forcing ( $\varepsilon_{w,1} = 0.15$  and  $\varepsilon_{w,2} = 0.45$ ) in  $\mathbb{K}_{5,8}$  (dashed),  $\mathbb{K}_{13,16}$  (dash-dotted).

and  $\varepsilon_{w,1}$  is varied from 0.05 up to 0.6. The characterization of the mixing efficiency was based on averaging 20 simulations, each starting from an independent realization of the initial velocity field. The different initial conditions were each separated by two eddy-turnover times.

The instantaneous and cumulative effects arising from both the large-scale and the two-band forcing are shown in Fig. 2.9. The development of the

instantaneous surface area and wrinkling is qualitatively similar in each case. The concentrated initial tracer distribution is in the first stages primarily dispersed by convective sweeping in the turbulent flow. As a result, the level set corresponding to  $a = 1/4$  becomes distorted and both  $\vartheta_A$  and  $\vartheta_W$  show a rapid increase. However, since no source of scalar was included in the computational model, molecular diffusion dominates the long-time behavior and leads to  $\vartheta_A$  and  $\vartheta_W$  to decrease to zero as  $t \rightarrow \infty$ . In between,  $\vartheta_A$  and  $\vartheta_W$  reach their maximum. The rapid initial growth is also clearly expressed in Figs. 2.9(c) and (d). In addition, the cumulative measures  $\zeta_A$  and  $\zeta_W$  show a clear saturation as  $t \gtrsim 1$ .

We observe from Figs. 2.9(a) and (b) that forcing of the large scales only, creates the highest growth rate of surface area and wrinkling. The surface area reaches its maximum value both sooner and at a higher value in this case. In the initial stages convective spreading of the tracer dominates over the decay caused by molecular diffusion; hence in these stages the agitation of the larger scales plays a crucial role in the evolution of the surface area. The higher band forcing needs to compete more directly with the viscous effects and does not induce very strong sweeping motions over large distances. Correspondingly, high- $k$  forcing is found less effective in producing surface area. The more localized distortions of the scalar level sets, as expressed by the development of the wrinkling, are less affected by the competition with viscosity, as seen in Fig. 2.9(b).

The interpretation of the effectiveness of the mixing in relation to the specific forcing alters if we compare the accumulated values for surface area and wrinkling. As may be appreciated from Figs. 2.9(c) and (d), a significant enhancement of the accumulated long-time surface area and wrinkling arises as a result of the explicit agitation of the smaller scales in the flow. Evidently, forcing of the smaller scales does not yield a more intense mixing, judging from the instantaneous values, but does yield an increase in the total surface area and wrinkling, accumulated over time.

To measure the influence of variations in the strength of the forcing in the high- $k$  band, we focus on the  $\mathbb{K}_{1,1}$  and  $\mathbb{K}_{13,16}$  two-band forcing. In particular, we keep  $\varepsilon_{w,1} + \varepsilon_{w,2} = 0.6$  and vary the values of  $\varepsilon_{w,2}$ . The effects on the cumulative mixing efficiency are shown in Fig. 2.10(a). We observe that an increase in  $\varepsilon_{w,2}$  implies a slight decrease in the initial growth rate

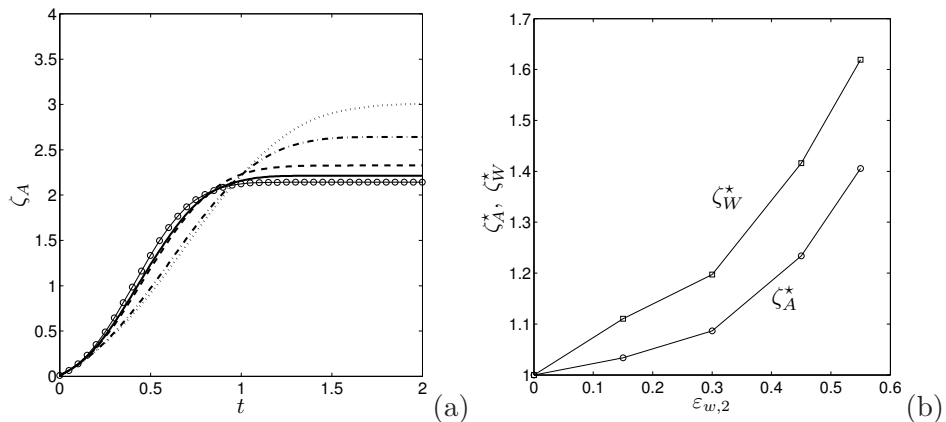


**Fig. 2.10:** (a) Evolution of the decaying passive scalar accumulated surface-area parameter  $\zeta_A$  for two-band forcing ( $\mathbb{K}_{1,1} - \mathbb{K}_{13,16}$ ) with different equipartitions of energy between bands: (0.60 – 0.00) ( $\circ$ ), (0.45 – 0.15) (solid), (0.30 – 0.30) (dashed), (0.15 – 0.45) (dot-dashed), (0.05 – 0.55) (dotted). (b) Total surface area  $\zeta_A^*$  and wrinkling  $\zeta_W^*$  at  $t = 2$  for different  $\varepsilon_{w,2}$  in  $\mathbb{K}_{13,16}$  (results normalized by the total surface area and wrinkling for the large-scale forcing).

of instantaneous surface area, but an increase in the long-time cumulative effect. The dependence of the long-time cumulative effect on  $\varepsilon_{w,2}$  is clarified in Fig. 2.10(b). These simulation results establish the degree of control that may be achieved with two-band forcing and the feasibility of such computational modeling. This approach may help to identify optimal stirring procedures to which future research will be devoted.

## 2.5 Conclusions

Various deterministic forcing methods that perturb a turbulent flow in a chosen range of length scales were examined. The presented modeling framework incorporates the explicit forcing as an integral part. We have shown that with a relatively simple forcing model basic properties of complex flows can be captured. For example, an enhancement of the energy dissipation by small-scale forcing was seen to produce so-called spectral shortcut features, quite similar to what was observed experimentally in flow over canopies [31] where the kinetic energy is immediately transferred

to the smallest scales of the flow. Forcing methods agitating the flow in a wide range of scales induce significant differences in the developing flow, compared to the case obtained classically in which only the large scales are forced. Various forcing methods were introduced and shown to produce qualitatively similar results, provided the forcing parameters correspond to turbulence at comparable total kinetic energies. We classified the methods according to constant energy or constant-energy input rate and examined these procedures by simulating forced turbulence with energy injected in two different bands. The modulation of the turbulent flow was investigated for various locations of the second high- $k$  band in spectral space. It was shown that the forcing in the second band induces nonlocal modulation of the energy spectrum. This was further examined by simulations done with different strength of forcing in the high- $k$  band controlled by the energy-injection rate.

We devoted special attention to a recently proposed multiscale forcing that models a flow under the influence of an additional perturbation by a multiscale object [70]. We performed numerical simulations of the dispersion of a passive scalar field in a turbulent flow that is driven by such forcing. A level set integration method was adopted to quantify general characteristics of mixing quality and efficiency. It was found that broadband forcing causes additional production of smaller scales in the flow, which is directly responsible for the localized enhancement of the wrinkling of the level set. In contrast, the surface area of a level set of the tracer is found to be mainly governed by convective sweeping by the larger scales in the flow and hence it is governed to a greater extent by the energy-input rate allocated to the small- $k$  range. Future study will include the spatial localization of the forcing. This can help to model flows that are more closely related to realistic physical situation observed in experiments and applications.

## Appendix: Computational method

In this appendix, we describe the computational method and parallelization in some detail. First, we specify the time-stepping method, then we sketch some aspects of the implementation of the pseudo-spectral method and subsequently the validation of the method is described along with its parallel performance.



## Time evolution

To simulate the spectral solution governed by Eqs. (2.10) and (2.12) we first rewrite these equations in a more general form having in mind that the evolution due to the diffusive terms can be computed exactly by introducing integrating factors  $e^{\nu k^2 t}$  and  $e^{\kappa k^2 t}$ , respectively [17]. In fact, Eqs. (2.10) and (2.12) may be expressed as

$$\frac{\partial \mathbf{U}(\mathbf{k}, t)}{\partial t} = \mathbf{G}(\mathbf{U}(\mathbf{k}, t)), \quad (2.33)$$

$$\text{where } \mathbf{U} = \begin{bmatrix} \mathbf{u}(\mathbf{k}, t) e^{\nu k^2 t} \\ c(\mathbf{k}, t) e^{\kappa k^2 t} \end{bmatrix}; \quad \mathbf{G} = \begin{bmatrix} (\mathbf{D}\mathbf{W}(\mathbf{k}, t) + \mathbf{F}(\mathbf{k}, t)) e^{\nu k^2 t} \\ Z(\mathbf{k}, t) e^{\kappa k^2 t} \end{bmatrix}.$$

We use a constant time-step  $\Delta t$  to obtain the solution at times  $t_n = t_0 + n\Delta t$ . A four-stage, second-order, compact-storage Runge-Kutta method was implemented. The advancement of the solution over a full time-step requires four steps of the form

$$\mathbf{U}(\mathbf{k}, t_{n+\gamma}) = \mathbf{U}(\mathbf{k}, t_n) + \gamma\Delta t \mathbf{G}(\mathbf{U}(\mathbf{k}, t_{n+\xi})). \quad (2.34)$$

The intermediate solutions in the different stages can be found as follows. In stage 1 we adopt  $(\gamma, \xi) = (1/4, 0)$ , stage 2 requires  $(\gamma, \xi) = (1/3, 1/4)$ , stage 3 uses  $(\gamma, \xi) = (1/2, 1/3)$  and stage 4 completes the step with  $(\gamma, \xi) = (1, 1/2)$  [34].

We consider turbulence in a cubic box of side  $L_b$  with periodic boundary conditions and assume that the flow is statistically isotropic, which implies that we require the same resolution in each coordinate direction. The direct numerical simulations will employ a resolution of  $N^3$ , where  $N$  is the number of spectral space grid points that is used in each direction. This restricts the set of wave numbers to  $n_\alpha = 0, \pm 1, \pm 2, \dots, \pm(N/2 - 1), -N/2$ . The cutoff wave number is given by  $k_{\max} = \pi N/L_b$ . In physical space this corresponds to a uniform grid  $x_\alpha = jL_b/N$ , where  $j = 0, 1, 2, \dots, N - 1$  in each coordinate direction. We use the pseudo-spectral discretization method, i.e., the spatial derivative terms in the Navier–Stokes and passive scalar equations are computed via simple multiplications in the spectral space. The nonlinear terms in the equations are evaluated in physical

space to avoid the evaluation of several computationally intensive convolution sums [17]. This procedure requires three steps. First, the Fourier coefficients  $\mathbf{u}(\mathbf{k}, t)$  and  $c(\mathbf{k}, t)$  are used to obtain the velocity and scalar fields in the physical space. Subsequently, the velocity-velocity products and the velocity-scalar products are determined in physical space and finally the associated Fourier coefficients of these products are obtained.

### Aliasing error

The finite resolution may give rise to well-known aliasing errors. In fact, the product of two Fourier series based on a resolution with  $N$  points gives rise to more small-scale modes than can be supported by the grid. As a result, these contributions can appear on the  $N$ -point resolution as seemingly lower wave-number modes. A detailed discussion of techniques allowing the partial or full removal of the aliasing error can be found in Ref. [17]. To eradicate the aliasing error we study in more detail *(i)* the random phase shifts method and *(ii)* the method employing two-shifted grids with spherical truncation, closely following [88, 89]. In the first case, the aliasing error is only partially removed. With additional truncation of the Fourier velocity field coefficients the remaining error can be reduced to  $\mathcal{O}(\Delta t^2)$ . In the method employing two-shifted grids and spherical truncation, the aliasing error can be fully removed from the simulations. This specific approach doubles the computational costs and memory requirements, compared to the random shifts method. The well-known 3/2 method can be used as well, by going to higher resolution and truncating the field. This can be done with the lowest number of operations, but has higher memory requirements. The aliasing error for higher-resolution runs affects mainly the small-scale statistics. This is visualized in Fig. 2.11 where we have shown the Taylor-Reynolds number and the longitudinal skewness for decaying turbulence simulations with initial  $R_\lambda = 100$  and two resolutions  $128^3$  and  $192^3$ . The partial dealiasing removes the main aliasing error and with the additional truncation reduces it to the accuracy associated with the adopted Runge-Kutta scheme. There is a small difference between the full and partial removal of the aliasing error for the lower resolution of  $128^3$ , but this largely vanishes for the well-resolved  $192^3$  case. The method of two shifted grids and spherical truncation was used in actual simulations. This removes the aliasing error completely, which was found to be essential, especially to maintain the characteristics of the small turbulent scales.

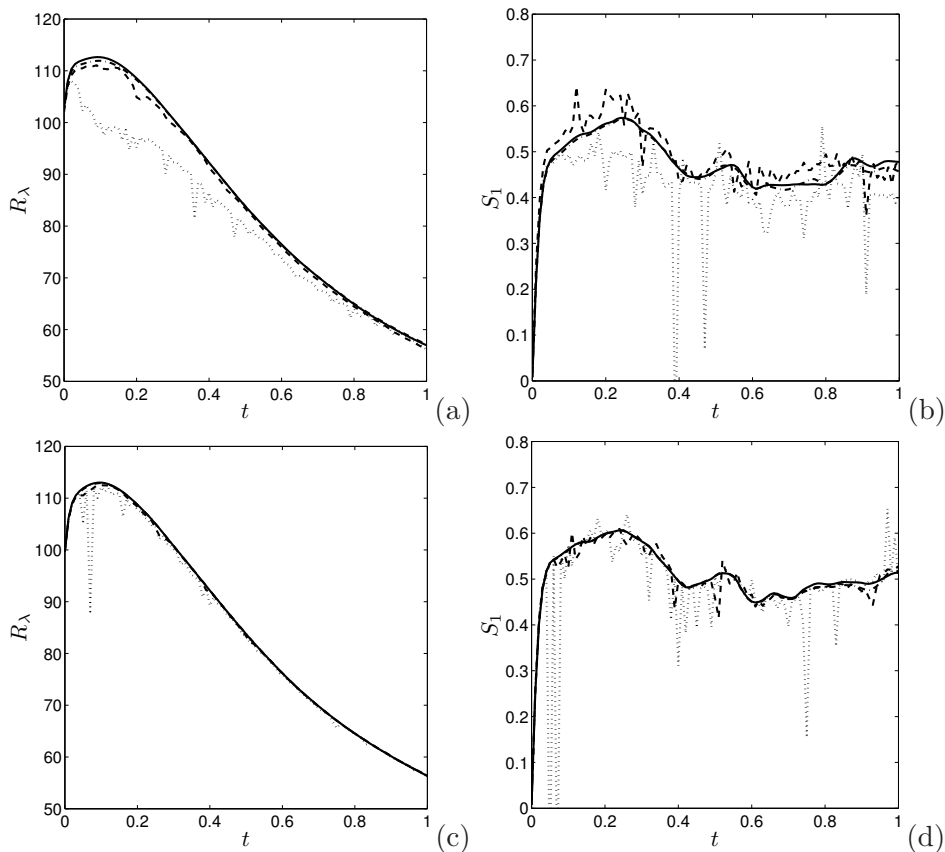


**Fig. 2.11:** Influence of aliasing error for resolution  $128^3$  (a-b) and  $192^3$  (c-d) on Taylor-Reynolds number  $R_\lambda(t)$  and longitudinal skewness  $S_1(t)$  at an initial  $R_\lambda = 100$  case. Simulations with aliasing error (dotted), partial dealiasing without truncation (dashed), partial dealiasing with the truncation (dash-dotted), full dealiasing by two grid shifts (solid). Results for the partial dealiasing with truncation (dash-dotted) are almost identical to fully dealiased results (solid).

### Data decomposition and fast Fourier transforms

The simulation software was implemented in Fortran 90 and parallelized based on the framework given in Ref. [110] using the Message Passing Interface (MPI) [83]. Data are stored using the Hierarchical Data Format

(HDF5) [42], which is a file format and library designed for scientific data storage and handling. The choice of HDF5 was motivated by the flexible data exchange between different platforms and its support of parallel I/O. High performance computations were done at SARA Computing and Networking Services (Amsterdam) on Silicon Graphics (SGI) Altix 3700 and Origin 3800 CC-NUMA systems (for more details see Ref. [91]). The critical

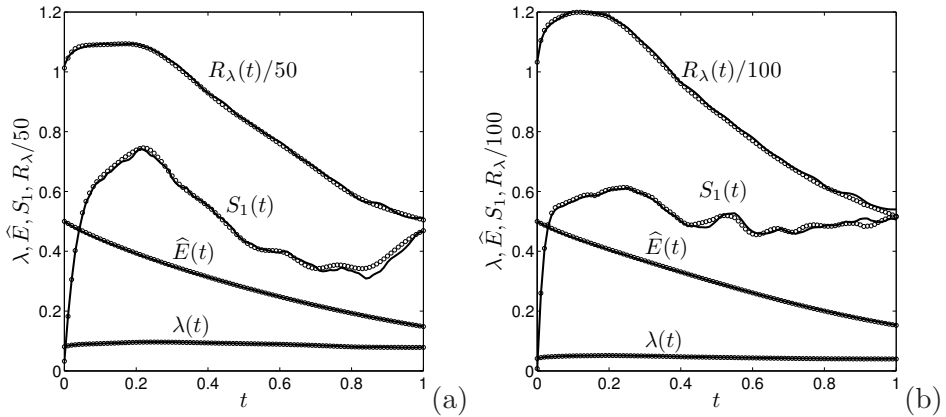


**Fig. 2.12:** Prediction of total energy  $\widehat{E}$ , Taylor microscale  $\lambda$ , Taylor Reynolds number  $R_\lambda$  and longitudinal skewness  $S_1$  at an initial  $R_\lambda = 50$  (a) and  $R_\lambda = 100$  (b) with a finite-volume [77] (solid) and the present pseudo-spectral (dotted) code.

performance factors in the parallel implementation of the pseudo-spectral discretization method are the domain decomposition and the algorithm for the three-dimensional Fast Fourier Transform (FFT). These two implementation decisions are essential since they determine almost all aspects of the data exchange between domains and most of the floating point operations. It is important to obtain a data decomposition, which permits for fast transfer of data between processors. To obtain parallel Fourier transforms we adopted procedures from two libraries: SCSL [37] and FFTW [32]. Moreover, since access to memory and the number and speed of available CPU-s may differ considerably among different computational platforms, significant improvements in the processing time can be achieved by platform-dependent optimization. The speedup of the parallel implementation was checked by simulating decaying turbulence at a resolution

of  $256^3$ . A time interval  $0 \leq t \leq 0.05$  was considered. This case corresponds to 28 time-steps with 5 data evaluation and reporting stages. In a non-dedicated SGI Altix 3700 environment we obtained on 4, 8, 16, 32, 64 processors the following speedup numbers: 3.9, 7.5, 14, 26, 47, respectively. The best performance results were obtained by a cache-unfriendly parallelization along the second array dimension. This gives the opportunity of minimal data exchange and reshuffling between processors and illustrates that the speed of the processors overwhelms the abilities of direct access to the memory. This was found to be the critical issue for the hardware that was available.

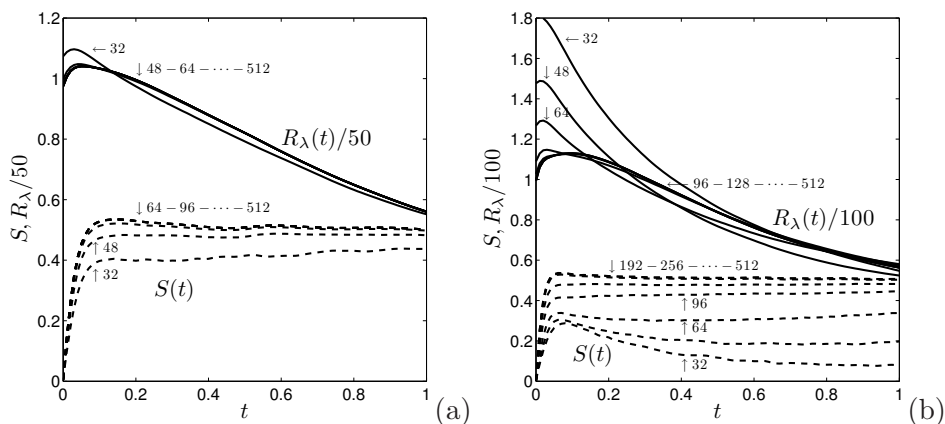


**Fig. 2.13:** Convergence of predictions for the Taylor-Reynolds number  $R_\lambda$  and the skewness  $S$  at an initial  $R_\lambda = 50$  (a) and  $R_\lambda = 100$  (b) for different resolutions  $N = 32 \cdot 48 \cdot 64 \cdot 96 \cdot 128 \cdot 192 \cdot 256 \cdot 384 \cdot 512$ .

## Code validation

To validate the implementation of the pseudo-spectral method, decaying homogeneous isotropic turbulence was simulated at two different Reynolds numbers. The initial condition was taken from Ref. [77], which was generated on the basis of the Pao spectrum [86]. For further details we refer to Ref. [76]. This flow was studied extensively using high-order finite-volume discretization and explicit Runge-Kutta time-stepping. Special attention was given to the degree of convergence that could be achieved using the

finite volume approach. These data provide a clear point of reference with which the present pseudo-spectral flow solver can be compared. A first,

$R_\lambda/N^3$	$32^3$	$48^3$	$64^3$	$96^3$	$128^3$	$192^3$	$256^3$	$384^3$	$512^3$
50	0.56	0.83	<u>1.11</u>	1.67	2.22	3.34	4.45	6.67	8.90
100	0.20	0.29	0.39	0.59	0.79	<u>1.18</u>	1.57	2.36	3.15

**Table 2.1:** The value of  $k_{\max}\eta$  associated with different resolutions. The Kolmogorov scales are  $\eta = 5.87 \cdot 10^{-3}$  and  $\eta = 2.07 \cdot 10^{-3}$  for  $R_\lambda = 50$  and  $R_\lambda = 100$ .

global assessment of the resolution that is achieved may be inferred by evaluating the product of the cutoff wave number and the observed Kolmogorov dissipation length scale  $\eta = L(3R_\lambda^2/20)^{-3/4}$  in terms of the Taylor-Reynolds number  $R_\lambda$  computed for the initial condition (see Eq. (2.37) for the definition) and integral length  $L = 1/2$ . In order to resolve all dynamically relevant length scales, including the dissipation length scale it is required that  $k_{\max}\eta$  is sufficiently large. A commonly accepted criterion of adequate spatial resolution is that  $k_{\max}\eta > 1$ . When the focus is on higher-order statistics, it is preferred to use larger values ( $k_{\max}\eta > 3/2$ ) [103, 30]. In Table 2.1 the values of  $k_{\max}\eta$  are presented for the two computational Reynolds numbers considered  $Re = 1061$  and  $Re = 4243$  that correspond to  $R_\lambda = 50$  and  $R_\lambda = 100$ , respectively. We observe that in the first case a resolution of at least  $64^3$  is required to achieve full resolution, while in the second case the minimal required resolution moves up to  $192^3$ .

For validation of the code, the flow was simulated for more than two eddy-turnover times and a number of quantities were monitored:

$$\text{Total energy :} \quad \widehat{E}(t) = \sum_{\mathbf{k}} E(\mathbf{k}, t) \quad (2.35)$$

$$\text{Taylor microscale :} \quad \lambda(t) = \left( 5\widehat{E}(t) / \sum_{\mathbf{k}} k^2 E(\mathbf{k}, t) \right)^{1/2} \quad (2.36)$$

$$\text{Taylor Reynolds :} \quad R_\lambda(t) = \lambda(t)u(t)/\nu; \quad u(t) = \sqrt{\frac{2}{3}\widehat{E}(t)} \quad (2.37)$$

$$\text{Longitudinal skewness :} \quad S_1(t) = -\frac{\langle (\partial v_1(\mathbf{x}, t) / \partial x_1)^3 \rangle}{\langle (\partial v_1(\mathbf{x}, t) / \partial x_1)^2 \rangle^{3/2}} \quad (2.38)$$

The operator  $\langle \cdot \rangle$  in Eq. (2.38) refers to volume averaging.

In Fig. 2.12, a comparison is made between simulation results obtained with the pseudo-spectral method at  $N = 512$ , and with the high-order finite-volume discretization method [77]. For each of the quantities an almost perfect agreement may be observed. In Fig. 2.13 we assessed the convergence of the predictions as function of the spatial resolution. In this figure we replaced the longitudinal skewness  $S_1$  by the skewness

$$S(t) = \frac{2}{35} \left( \frac{\lambda(t)}{u(t)} \right)^3 \sum_{\mathbf{k}} k^2 T(\mathbf{k}, t). \quad (2.39)$$

For homogeneous isotropic turbulence the value of  $S$  should be equal to 0.5 [3], which is quite well approximated in the simulations. This quantity is quite sensitive to the spatial resolution and is therefore a good indicator of appropriate spatial resolution. We observe that the different predictions display a clearly distinguishable convergence toward the grid independent solution. Specifically, results obtained for resolutions higher than  $64^3$  at  $R_\lambda = 50$  and  $192^3$  at  $R_\lambda = 100$  are quite indistinguishable, consistent with the criterion that  $k_{\max}\eta > 1$ .

## Acknowledgments

The work is supported by the Foundation for Fundamental Research on Matter (FOM), Utrecht, the Netherlands. Simulations were performed at SARA; special thanks go to Willem Vermin for support with the parallelization. The computations were made possible through grant SC-213 of the Dutch National Computing Foundation (NCF). AKK would like to thank David McComb for many stimulating discussions during research visits at the University of Edinburgh. BJK gratefully acknowledges support from the Turbulence Working Group (TWG) at the Center for Non-Linear Studies (CNLS) at Los Alamos National Laboratory which facilitated an extended research visit in 2005 and allowed many fruitful discussions. Special thanks go to Darryl Holm.





# Chapter 3

## Energy dynamics in broadband-forced turbulence<sup>†</sup>

Classically, large-scale forced turbulence is characterized by a transfer of energy from large to small scales via nonlinear interactions. We have investigated the changes in this energy transfer process in *broadband*-forced turbulence where an additional perturbation of flow at smaller scales is introduced. The modulation of the energy dynamics via the introduction of forcing at smaller scales occurs not only in the forced region but also in a broad range of length scales outside the forced bands due to nonlocal triad interactions. Broadband forcing changes the energy distribution and energy transfer function in a characteristic manner leading to a significant modulation of the turbulence. We studied the changes in this transfer of energy when changing the strength and location of the small-scale forcing support. The energy content in the larger scales was observed to decrease, while the energy transport power for scales in between the large and small scale forcing regions was enhanced. This was investigated further in terms of the detailed transfer function between the triad contributions and observing the long-time statistics of the flow. The energy is transferred toward smaller scales not only by wave numbers of similar size as in the case of large-scale forced turbulence, but by a much wider extent of scales that can be externally controlled.

---

<sup>†</sup>“*Nonlocal modulation of energy cascade in broadband-forced turbulence*” by A. K. Kuczaj, B. J. Geurts, and W. D. McComb appeared in *Physical Review E*, 74, 016306, 2006 [63].

### 3.1 Introduction

The dynamics of kinetic energy plays a central role in turbulent flows. The nonlinear term in the Navier–Stokes equations is responsible for the transfer of energy between any three wave vectors that form a triad in spectral space [71]. Along with the viscous and forcing terms this controls the production, transfer, and dissipation of energy in the system. The triadic interactions have been studied for decaying and forced turbulence by many authors (for a review, see Ref. [113]). Throughout the years various types of large-scale forcing methods [93, 56, 30, 21, 52, 36, 67, 85, 54] have been proposed to sustain quasistationarity in numerical turbulence as an idealized form of turbulent flow. The aim of such numerical experiments was to investigate the basic concept of the Kolmogorov (K41) theory [58] that proposes an inertial range in the kinetic energy spectrum and local transfer of energy within this range. The turbulent kinetic energy is on average transferred locally from larger to neighboring smaller scales.

The purpose of this paper is to numerically investigate the processes associated with the flow of energy in a turbulent flow. Specifically, we consider *modulated* turbulence in which the modifications involve the supplementary forcing in a wide range of modes located in an inertial range of the flow. In the literature, mainly turbulence with forcing restricted to the large scales has been examined in detail [113]. The small scale behavior was found to be energetically quite insensitive to the type of forcing and at sufficiently high Reynolds numbers a well-developed inertial range was observed [111]. Against this background, we extend the use of forcing methods and investigate their application directly in the inertial range, thereby focusing particularly on the competition between transfer and forcing. We quantify the dominant alterations due to the broadband forcing in terms of changes in the energy cascading processes. We pay attention to the energy transfer function and consider changes that arise in the contributions from “local”, “nonlocal”, and “distant” triadic interactions. Compared to traditional large-scale forced turbulence, we observe a strengthening of the contributions of nonlocal interactions, leading to a modification of the inertial range spectrum.

High-resolution direct numerical simulations of turbulence that measure the influence of individual terms in the Navier–Stokes equations on the

triadic interactions have been reported [27, 24, 28, 25, 26, 84, 102]. It was found that the energetically dominant triadic interactions involve sets of three modes in which the magnitude of the wave vector of one of the modes differs considerably from the other two. This suggests that statistics of smaller scales may be affected by larger scales. These dominant processes are not in contradiction with the Kolmogorov theory because the energy is mainly exchanged between the two modes of quite similar wave-vector size [84]. Only a small net energy transfer toward larger wave numbers arises that involves a detailed cancellation between many individual triad transfers [102]. The spectral space dynamics is characterized by a multitude of separate transfer processes among various modes. These contributions can be collected in pairs with opposite sign and almost the same magnitude. In total, this leads to a large number of “near-cancellations” and hence only a comparably small net effect remains that constitutes the well-known “downward cascading” toward higher wave numbers in spectral space. This was confirmed with the use of helical mode decomposition in Ref. [102].

The dynamics of actual turbulent flows seen in nature is usually characterized by an enormous number of interacting scales, often perturbed by geometrically complex boundaries and influenced by additional forces such as rotation and buoyancy. This can lead to inhomogeneity and anisotropy, which are not covered directly in the classical view of the Kolmogorov energy cascade and may express themselves in nonlocal interactions of various particular scales of motion. The complexity of such systems motivated us to study in more detail forcing methods that simultaneously perturb a prescribed range of scales [60]. Such “broadband” agitation of various scales of motion is observed experimentally in turbulent drag reduction by fiber suspension [72, 73], flows through porous media [11], and over tree canopies [31]. In these cases the energy is transferred abruptly to small scales when the flow reaches an obstruction. Various other types of flows also exhibit turbulent motions that coexist at different scales [87].

To explore the possibilities of a broader application of forcing methods in turbulence modeling and concurrently examine the energy dynamics in flows that do not directly follow the classical Kolmogorov  $-5/3$  scaling we employ numerical simulations of *broadband*-forced turbulence. The forcing studied in this paper represents a continual addition/removal of energy from a broad range of scales in the system, thereby providing the possibility of

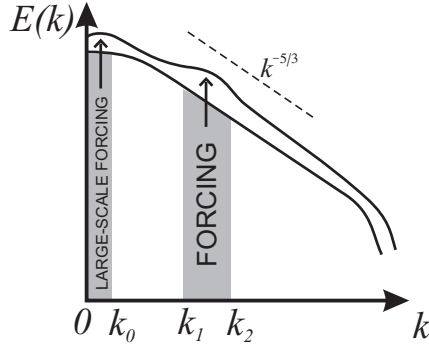


**Fig. 3.1:** Broadband forcing in spectral space. Large-scale forcing  $k \leq k_0$  with an additional high- $k$  forced region  $k_1 < k \leq k_2$ .

altering the characteristic  $-5/3$  slope in the kinetic energy spectrum as predicted by the K41 theory. Specifically, as indicated in Fig. 3.1, we apply the forcing to two regions. The large-scale forcing  $k \leq k_0$  classically agitates the largest scales in a flow while the additional band  $k_1 < k \leq k_2$  is located in a region of the inertial regime, to allow a direct competition with the nonlinear transfer term. For inertial-range scales broadband forcing introduces explicit energy injection next to the transfer term. We varied the spectral support and strength of the high- $k$  band to investigate the modulation of the turbulence that develops. This distinguishes it from the classical forcing of large scales only.

In this paper we compute changes in the energy distribution associated with the broadband forcing and observe a characteristic alteration in the spectral energy transfer compared to the classical Kolmogorov cascading. This alteration expresses itself by additional local minima and maxima in the transfer function. It is well known that in cases with large-scale forcing only, negative values are found for the transfer at the smallest wave numbers indicating the energy injection at these scales. The positive values for the transfer that arise for all other wave numbers indicates the energy cascading process to smaller scales. In our case of broadband forcing in the inertial range, additional negative regions appear in the transfer function. These coincide with the additional local injection of energy. Such a negative region is bordered by nearby additional maxima in the transfer. These characterize

the associated increased energy transfer to scales just larger or just smaller than the broadband-forced region.

Forcing applied to different spatial scales simultaneously allows a nonlocal modulation of the energy distribution compared to the reference Kolmogorov case. To quantify the alterations in the energy transfer we use a decomposition of the velocity field closely following Ref. [28] and investigate the magnitude of the contributions from various spatial scales to the overall energy transfer.

The main finding of this study pertains to the role of broadband inertial range forcing in modifying the natural energy cascading process. This is understood explicitly in terms of changes in the detailed nonlocal energy transfer. In addition, we illustrate and quantify the mechanism of enhancement of the total energy transfer to smaller scales arising from broadband forcing and the depletion of the energy content in the large scales. Agitation of certain high wave numbers can affect well separated low wave-number components in a flow. These findings may be relevant for problems that involve the control of turbulent flow in complex geometries in which various scales of motions are simultaneously agitated, e.g., in compact heat exchangers [11]. Further applications of such broadband forcing may be connected with the observed modulations of transport properties in physical space leading to an enhanced scalar dispersion rate [60].

The organization of this paper is as follows. The mathematical formulation of the problem is given in Sec. 3.2 where the computational method and the energy transfer terms are also described. The energy spectra of broadband-forced turbulence and the modulation of the energy transfer are investigated in Sec. 3.3. In Sec. 3.4 we present a more detailed view of the energy transfer processes by computing partitioned energy transfer function over various spatial scales. The paper closes with a summary in Sec. 3.5.

## 3.2 Computational flow model

### 3.2.1 Equations of motion

The incompressible Navier–Stokes equations in spectral (Fourier) representation can be written as

$$(\partial_t + \nu k^2) u_\alpha(\mathbf{k}, t) = \Psi_\alpha(\mathbf{k}, t) + F_\alpha(\mathbf{k}, t), \quad (3.1)$$

where  $u_\alpha(\mathbf{k}, t)$  is the velocity field coefficient at wave vector  $\mathbf{k}$  ( $k = |\mathbf{k}|$ ) and time  $t$  [71]. The nondimensional kinematic viscosity  $\nu$  is the inverse of the computational Reynolds number ( $\text{Re} = 1/\nu$ ). The nonlinear term reads

$$\Psi_\alpha(\mathbf{k}, t) = M_{\alpha\beta\gamma} \sum_{\mathbf{p}+\mathbf{q}=\mathbf{k}} u_\beta(\mathbf{p}, t)u_\gamma(\mathbf{q}, t), \quad (3.2)$$

and the forcing term  $F_\alpha(\mathbf{k}, t)$  is specified in Sec. 3.2.2. The tensor  $M_{\alpha\beta\gamma}$  in Eq. (3.2) accounts for the pressure and incompressibility effects:

$$M_{\alpha\beta\gamma} = \frac{1}{2l} \left( k_\beta D_{\alpha\gamma} + k_\gamma D_{\alpha\beta} \right), \quad (3.3)$$

in which

$$D_{\alpha\beta} = \delta_{\alpha\beta} - k_\alpha k_\beta / k^2. \quad (3.4)$$

Taking the inner product of (3.1) and  $u_\alpha^*(\mathbf{k}, t)$ , where the asterisk denotes the complex conjugate, we obtain the energy equation

$$(\partial_t + 2\nu k^2) E(\mathbf{k}, t) = T(\mathbf{k}, t) + T_F(\mathbf{k}, t). \quad (3.5)$$

The spectral energy density is denoted by  $E(\mathbf{k}, t) = \frac{1}{2} u_\alpha^*(\mathbf{k}, t) u_\alpha(\mathbf{k}, t)$ . The rate of energy exchanged at wave vector  $\mathbf{k}$  with all other modes in the system is characterized by the energy transfer function

$$T(\mathbf{k}, t) = u_\alpha^*(\mathbf{k}, t) \Psi_\alpha(\mathbf{k}, t). \quad (3.6)$$

The rate of energy provided by the forcing term is

$$T_F(\mathbf{k}, t) = u_\alpha^*(\mathbf{k}, t) F_\alpha(\mathbf{k}, t), \quad (3.7)$$

and the energy dissipation rate present in Eq. (3.5) reads

$$\varepsilon(\mathbf{k}, t) = 2\nu k^2 E(\mathbf{k}, t). \quad (3.8)$$

The three terms  $T(\mathbf{k}, t)$ ,  $T_F(\mathbf{k}, t)$  and  $\varepsilon(\mathbf{k}, t)$  represent the energy dynamics in the system that each typically act in distinct wave-number regions. The forcing term  $T_F(\mathbf{k}, t)$  is nonzero in the forced modes only. In this paper the collection of forced modes will always contain a low wave-number band corresponding to large-scale forcing of the flow. In addition, higher wave-number contributions will be included in  $T_F(\mathbf{k}, t)$ . In contrast, the energy

dissipation rate  $\varepsilon(\mathbf{k}, t)$  is defined in the entire spectral space, but it is dynamically important primarily for the high wave-number range. Finally, the transfer term  $T(\mathbf{k}, t)$  is basic to the development of an energy cascade and is a dominant contribution for wave-numbers in an inertial range [71].

The change of the total energy  $\widehat{E}$  in the system is connected with its viscous dissipation and the total effect of the forcing. In fact, introducing

$$\widehat{E}(t) = \sum_{\mathbf{k}} E(\mathbf{k}, t), \quad (3.9)$$

we find

$$\partial_t \widehat{E}(t) = \widehat{T}_F(t) - \widehat{\varepsilon}(t), \quad (3.10)$$

where  $\widehat{\varepsilon}(t) = \sum_{\mathbf{k}} \varepsilon(\mathbf{k}, t)$  and  $\widehat{T}_F(t) = \sum_{\mathbf{k}} T_F(\mathbf{k}, t)$ . We used the fact that the total energy transfer  $\widehat{T}(t) = \sum_{\mathbf{k}} T(\mathbf{k}, t) = 0$ . The injection of energy occurs only in the forced region. This keeps the whole system in a quasistationary state. Normally, the forced region is restricted to the largest scales in a flow represented by the smallest wave numbers [30, 85]. The energy introduced in the large scales is transferred to smaller scales and dissipated primarily in very localized flow features of viscous length scales. By the introduction of an additional source of energy in the inertial range we will study the perturbation of the energy cascading process by the forcing.

### 3.2.2 Forcing method

Forcing is achieved by applying an additional driving  $F_\alpha(\mathbf{k}, t)$  to the velocity field in Fourier space, cf. Eq. (3.1). Conventionally, the turbulent cascade develops as a statistical equilibrium is reached, characterized by the balance between the input of kinetic energy through the forcing and its removal through viscous dissipation. In literature [93, 56, 30, 21, 52, 36, 67, 85, 54], we may distinguish several numerical approaches to forced turbulence that all refer to the agitation of the largest scales of motion. Here, we modify such classical forcing procedures by allowing for the simultaneous agitation of a broader range of intermediate- $k$  modes as depicted in Fig. 3.1.

We study two ranges of forcing: the classical large-scale forcing ( $k \leq k_0$ ) and small-scale forcing localized in the spectral region where the transfer of energy  $T(\mathbf{k}, t)$  is important ( $k_1 < k \leq k_2$ ). By narrowing or widening

the width of the forced bands, along with a change in their location in spectral space we can control several aspects of the energy-dynamics. The strength of forcing is controlled by the amount of energy introduced to various regions in spectral space.

We expect the small-scale forcing band to influence the interscale energy transfer process not only between scales of similar size but at a wider spectrum of scales. This may be understood globally as follows. The process of energy cascading is mainly interpreted via the resulting local transfer of energy in spectral space [84]. However, this total energy transfer results from many nonlocal contributions and these may be directly altered by the additional small-scale forcing. Correspondingly an influence on the overall energy cascading process may occur over an extended wave-number range. We quantify this effect by evaluating the nonlinear interactions among the various modes while they are being perturbed by the broadband forcing.

In this paper we adopt the recently proposed fractal forcing [70], which involves a power-law dependence of  $F_\alpha$  on the wave number:

$$F_\alpha(\mathbf{k}, t) = \tilde{\varepsilon}_w(\mathbf{k}) \frac{k^\beta e_\alpha(\mathbf{k}, t)}{\sum_{\mathbf{k} \in \mathbb{K}} k^\beta \sqrt{2E(\mathbf{k}, t)}}, \quad (3.11)$$

where the coefficient  $\beta = D_f - 2$  is connected with the fractal dimension  $D_f$  of the stirrer and  $\tilde{\varepsilon}_w(\mathbf{k})$  is the energy input rate at mode  $\mathbf{k}$ . The fractal forcing is based on a simple argument of drag enhancement associated with flow passing through complex “porous” regions, e.g., a metal foam or the canopy of a tree. The complexity of such obstructing objects may be captured to some extent in terms of their fractal dimension  $D_f$  as elaborated in literature (see, e.g., Refs. [31, 70] and references therein). In Ref. [60] the effect of various deterministic forcing methods was compared and a qualitative independence of the particular type of forcing was observed, both in case of large-scale forcing only and when broad band forcing was adopted. In this paper we selected the fractal forcing as a characteristic forcing procedure for further investigation of the nonlocal alterations in the energy transfer. The fractal dimension  $D_f$  is taken equal to 2.6, close to the experimental value found for fractal grids reported in Ref. [69]. Variation of  $D_f$  by about 20% was considered and found to yield only small effects on the spectrum.



The set of forced modes  $\mathbb{K}$  is composed of bands  $\mathbb{K}_{m,p}$  ( $m \leq p$ ) which consist of  $p - m + 1$  adjacent spherical shells  $\mathbb{S}_n = \frac{2\pi}{L_b}(n - 1/2) < |\mathbf{k}| \leq \frac{2\pi}{L_b}(n + 1/2)$ :  $m \leq n \leq p$ , in terms of the size of the computational domain denoted by  $L_b$ . In the simulations we always force the first shell  $\mathbb{S}_1$  and a single high- $k$  band  $\mathbb{K}_{m,p}$ , if not stated otherwise. The classical large-scale forcing of the first shell  $\mathbb{S}_1$  has a constant energy injection rate  $\varepsilon_{w,1}$  in Eq. (3.11) while  $\mathbb{K}_{m,p}$  has a constant strength  $\varepsilon_{w,2}$  and a support in spectral space controlled by  $m$  and  $p$ :

$$\tilde{\varepsilon}_w(\mathbf{k}) = \begin{cases} \varepsilon_{w,1} & \text{if } \mathbf{k} \in \mathbb{S}_1, \\ \varepsilon_{w,2} & \text{if } \mathbf{k} \in \mathbb{K}_{m,p}, \\ 0 & \text{otherwise.} \end{cases} \quad (3.12)$$

The vector  $\mathbf{e}$  in Eq. (3.11) is given by [70]

$$\mathbf{e}(\mathbf{k}, t) = \frac{\mathbf{u}(\mathbf{k}, t)}{|\mathbf{u}(\mathbf{k}, t)|} + i \frac{\mathbf{k} \times \mathbf{u}(\mathbf{k}, t)}{|\mathbf{k}| |\mathbf{u}(\mathbf{k}, t)|}. \quad (3.13)$$

This vector consists of two parts, either parallel or perpendicular to the vector  $\mathbf{u}(\mathbf{k}, t)$ . In this forcing procedure, we have control over the energy input rate, the range of forced modes and the effective geometrical complexity of the stirrer represented by the fractal dimension.

The summation over all forced modes of  $u_\alpha^*(\mathbf{k}, t)F_\alpha(\mathbf{k}, t)$  yields a total energy input rate given by

$$\widehat{T}_F(t) = \sum_{\mathbf{k}} T_F(\mathbf{k}, t) = \sum_{\mathbf{k}} u_\alpha^*(\mathbf{k}, t)F_\alpha(\mathbf{k}, t) = \varepsilon_w, \quad (3.14)$$

where  $\varepsilon_w = \varepsilon_{w,1} + \varepsilon_{w,2}$ . The energy input leads to a quasistationary state described by the energy equation

$$\partial_t \widehat{E}(t) = \varepsilon_w - \widehat{\varepsilon}(t). \quad (3.15)$$

This characterizes the energy dynamics in the system at the most global level. We observe that this forcing implies a constant energy injection rate that results in a fluctuating total energy  $\widehat{E}$  and a fluctuating total energy dissipation rate with mean  $\varepsilon_w$ .

### 3.2.3 Energy transfer

A detailed investigation of the energy transfer in large-scale forced turbulence [84] shows that the dominant triadic interactions occur between

wave vectors of quite different lengths. Hence large-scale forcing may be directly involved in the dynamics of much smaller scales [108]. The interactions are roughly classified as “local” when the sizes of all wave vectors in a triad are similar, “nonlocal” when the scale separation is about a factor 10–15 and “distant” when the separation is much larger [12]. It was shown that the transfer of energy reaches maximum values for triads with two wave vectors of similar size and one with quite different length [84]. Although, the interactions between triads can be seen mainly as nonlocal, the dominant net energy transfer is local, i.e., occurring between similar scales [111, 112, 114]. The interactions produce forward and backward energy transfer that combined result in a small net forward energy transfer because of the detailed balance between contributions that virtually cancel each other [102]. The forward cascade in the inertial range was found to be dominated by local and nonlocal interactions, while the distant interactions do not significantly transfer energy [12]. All these findings concern the classical turbulence forced at the largest scales.

Against this background, we ask what the turbulence response will be to a broadband perturbation of the energy transfer processes? In recent literature a somewhat related study was reported in Ref. [95]. Decaying turbulence that starts from an initial condition with an energetically strongly enhanced small-scale band of modes was studied. The presence of the extra small-scale band was found to reduce the intensity of the developing turbulence by enhancing the *nonlocal energy cascade* directly towards smaller scales. This removes the kinetic energy more efficiently. The energy feeding mechanisms and energy transfer also attract much attention in transitional and turbulent flows with an active control [81]. The modulation induced by the broadband forcing has its consequences not only in the spectral space dynamics of a flow but also in its physical space transport properties [60].

To analyze the response of turbulence to the additional broadband perturbation in more detail we apply previously developed methods used in the examination of energy transfer in large-scale forced turbulence [28]. Referring to Fig. 3.2, the energy transfer between a wave vector  $\mathbf{k} = (k_1, k_2, k_3)$  and all pairs of wave vectors  $\mathbf{p}$  and  $\mathbf{q} = \mathbf{k} - \mathbf{p}$  with  $\mathbf{p}$ ,  $\mathbf{q}$  chosen in some prescribed regions  $\mathbb{P}$  and  $\mathbb{Q}$  will be investigated. Such a decomposition allows measuring the contribution of separate scales to the transfer function  $T(\mathbf{k}, t)$ . The precise specification requires a few steps that are presented

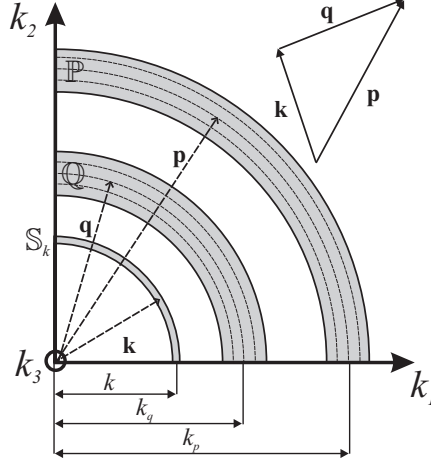


**Fig. 3.2:** Schematic triadic interaction that occurs between wave vector  $\mathbf{k}$  in shell  $\mathbb{S}_k$  and wave vectors  $\mathbf{p}$ ,  $\mathbf{q}$  taken from regions  $\mathbb{P}$  and  $\mathbb{Q}$  of spectral space that each consist of four shells with central wave numbers  $k_p$  and  $k_q$ .

next. First, we define the truncated velocity field as

$$u_\alpha^{(\mathbb{P},\mathbb{Q})}(\mathbf{k}, t) = \begin{cases} u_\alpha(\mathbf{k}, t) & \text{if } \mathbf{k} \in \mathbb{P} \text{ or } \mathbf{k} \in \mathbb{Q}, \\ 0 & \text{otherwise.} \end{cases} \quad (3.16)$$

Based on this truncated velocity field we may compute the energy transfer involving the wave vector  $\mathbf{k}$  and all wave vectors  $\mathbf{p}$  and  $\mathbf{q}$ :

$$T_{\mathbb{P}\mathbb{Q}}(\mathbf{k}, t) = \begin{cases} \tilde{T}_{\mathbb{P}\mathbb{P}}(\mathbf{k}, t) & \text{if } \mathbb{P} = \mathbb{Q}, \\ \frac{1}{2} [\tilde{T}_{\mathbb{P}\mathbb{Q}}(\mathbf{k}, t) - \tilde{T}_{\mathbb{P}\mathbb{P}}(\mathbf{k}, t) \\ - \tilde{T}_{\mathbb{Q}\mathbb{Q}}(\mathbf{k}, t)] & \text{if } \mathbb{P} \neq \mathbb{Q}, \end{cases} \quad (3.17)$$

where

$$\tilde{T}_{\mathbb{P}\mathbb{Q}}(\mathbf{k}, t) = u_\alpha^*(\mathbf{k}, t) \Psi_\alpha^{(\mathbb{P},\mathbb{Q})}(\mathbf{k}, t). \quad (3.18)$$

The nonlinear term  $\Psi_\alpha^{(\mathbb{P},\mathbb{Q})}(\mathbf{k}, t)$  is defined by the convolution of the truncated fields:

$$\Psi_\alpha^{(\mathbb{P},\mathbb{Q})}(\mathbf{k}, t) = M_{\alpha\beta\gamma} \sum_{\mathbf{p}+\mathbf{q}=\mathbf{k}} u_\beta^{(\mathbb{P},\mathbb{Q})}(\mathbf{p}, t) u_\gamma^{(\mathbb{P},\mathbb{Q})}(\mathbf{q}, t), \quad (3.19)$$

where the sum is over all triads with  $\mathbf{p} \in \mathbb{P}$  and  $\mathbf{q} \in \mathbb{Q}$  such that  $\mathbf{p} + \mathbf{q} = \mathbf{k}$ .

For a statistically isotropic, homogeneous turbulence it is convenient to average over spherical shells in wave-vector space. In addition, in view of the considerable computational effort involved in computing all interactions between the very large number of scales present in the flow, we introduced a slight coarse graining in terms of the regions  $\mathbb{P}$  and  $\mathbb{Q}$  as shown in Fig. 3.2. Specifically, it was found adequate to group together contributions from four adjacent shells. Other more coarse “groupings” of wave numbers have been considered in the literature with the aim of extracting the dominant interaction processes at a reasonable computational effort. As an example a “logarithmic” grouping was adopted in Ref. [28] combining contributions from bands with a width of  $2^k$ . In this paper we will look at the interactions of four shells  $\mathbb{P}$  at distance  $k_p$  (cf. Fig. 3.2) with four shells  $\mathbb{Q}$  at distance  $k_q$  that contribute to the nonlinear energy transfer to shell  $\mathbb{S}_k$  characterized by the wave number  $k$ .

In terms of the transfer function  $T_{\mathbb{P}\mathbb{Q}}(\mathbf{k}, t)$  we may now define the required spectral transfer functions. The energy transfer term (3.17) gives the exchange of energy by the triad  $(\mathbf{k}, \mathbf{p}, \mathbf{q})$  where the latter two wave vectors are specified by the sets  $\mathbb{P}$  and  $\mathbb{Q}$  and the triangle constraint. Summing over all modes  $\mathbf{k}$  in shell  $\mathbb{S}_k$  we obtain the exact exchange of energy in the  $k$ th shell between  $k$ ,  $k_p$ , and  $k_q$ :

$$T_{pq}(k, k_p, k_q, t) = \sum_{\mathbf{k} \in \mathbb{S}_k} T_{\mathbb{P}\mathbb{Q}}(\mathbf{k}, t). \quad (3.20)$$

We refer to  $T_{pq}$  as the “three-mode” transfer. The total energy transfer function  $T(k, t)$  can be computed directly from Eq. (3.6) or as sum of the contributions from Eq. (3.20):

$$T(k, t) = \sum_{k_p} T_p(k, k_p, t), \quad (3.21)$$

in which the “two-mode” transfer  $T_p$  is given by

$$T_p(k, k_p, t) = \sum_{k_q} T_{pq}(k, k_p, k_q, t). \quad (3.22)$$

The individual transfer terms  $T(k, t)$ ,  $T_p(k, k_p, t)$ , and  $T_{pq}(k, k_p, k_q, t)$  give, respectively, more detailed characteristics of the energy transfer. The total

transfer  $T(k, t)$  expresses the amount of energy transferred from (negative) or to (positive) shell  $\mathbb{S}_k$ . All three transfer terms  $T$ ,  $T_p$ , and  $T_{pq}$  will be used to investigate the transfer of energy in the sequel.

### 3.2.4 Simulation details

The numerical integration of the Navier–Stokes equations (3.1) is done via a four-stage, second-order, compact-storage, Runge-Kutta method [35]. To fully remove the aliasing error we applied a method that employs two shifted grids and spherical truncation [17]. We consider the canonical problem of forced turbulence in a cubic box of side  $L_b$  with periodic boundary conditions. Direct numerical simulations are characterized by  $N^3$  computational points, where  $N$  is the number of grid points used in each direction. A detailed description of the simulation setup and the validation of the numerical procedure can be found in Ref. [60]. The components of the wave vector  $\mathbf{k}$  are  $k_\alpha = (2\pi/L_b)n_\alpha$  where  $n_\alpha = 0, \pm 1, \pm 2, \dots, \pm(N/2 - 1), -N/2$  for  $\alpha = 1, 2, 3$ . The numerical simulations are defined further by the size of the domain ( $L_b=1$ ), the computational Reynolds number  $\text{Re}$  and the energy injection rates to the two distinct bands ( $\varepsilon_{w,1}, \varepsilon_{w,2}$ ).

We will study this homogeneous turbulent flow at two different computational Reynolds numbers, i.e.,  $\text{Re} = 1061$  and  $\text{Re} = 4243$ . In case of homogeneous, decaying turbulence these Reynolds numbers correspond to  $R_\lambda = 50$  or  $100$ , in terms of the initial Taylor-Reynolds number [60]. The large-scale forcing of  $\mathbb{S}_1$  has an energy injection rate  $\varepsilon_{w,1} = 0.15$  that is used as a reference case. For all simulations the fractal dimension was kept constant and equal to  $D_f = 2.6$  [70]. The smallest length scale that should be accurately resolved depends on the size of the box, viscous dissipation, and energy injection rate. Usually it is required that  $k_{\max}\eta > 1$  [30, 109, 74] in terms of the Kolmogorov length scale  $\eta$  and the maximal magnitude of the wave vector  $k_{\max} = \pi N/L_b$  that enters the computations. In our simulations  $k_{\max}\eta \gtrsim 2$  indicating that the small scales are well resolved.

We consider time-averaged properties of the turbulent flow. For a function  $h$  these are defined by

$$\langle h \rangle_t = \lim_{t \rightarrow \infty} \frac{1}{t - t_0} \int_{t_0}^t h(\tau) d\tau \approx \frac{1}{T - t_0} \int_{t_0}^T h(\tau) d\tau, \quad (3.23)$$

where  $\mathcal{T}$  is sufficiently large. We start the averaging at  $t_0 = 5$  which corresponds to about 10 eddy-turnover times for the simulated cases. The final time was taken equal to  $\mathcal{T} = 30$ , so all results are averaged over approximately 50 eddy-turnover times. The accuracy of this approximation to the long-time average, measured as the ratio of the standard deviation and the mean signal, is less than 5% for all investigated quantities.

The energy spectra presented in this paper are shell and time averaged. Moreover, we focus on compensated spectra  $E_c$  in which we use nondimensional Kolmogorov units:  $E_c(k) = \langle \hat{\varepsilon} \rangle_t^{-2/3} k^{5/3} \langle E_s(k, t) \rangle_t$  in terms of the shell-averaged spectrum  $E_s(k, t) = \sum_{\mathbf{k} \in \mathbb{S}_k} E(\mathbf{k}, t)$ . The compensation of the spectrum is not strictly required to observe the characteristic changes in the energy distribution, but as it gives more information about the dominant scales present in a flow it will be used throughout.

### 3.3 Broadband-forced turbulence

#### 3.3.1 Energy distribution in forced turbulence

We first concentrate on the application of the high- $k$  forcing band at *different locations* in spectral space. We apply a constant energy input rate  $\varepsilon_{w,2} = 0.15$  to this band. Simultaneously, the large-scale forcing to the first shell  $\mathbb{S}_1$  is  $\varepsilon_{w,1} = 0.15$ . The computational Reynolds number is  $\text{Re} = 1061$ . We forced the bands  $\mathbb{K}_{p,p+3}$  for  $p = 5, 9, 17, 25$ . The parameters of these simulations with some of the statistics are further presented in the Appendix (runs 1 and 14–17 in Tables 3.1 and 3.2 are concerned here).

The total kinetic energy, energy dissipation rate, and Taylor-Reynolds number are shown in Fig. 3.3 as a function of the location of the left-boundary  $p$  of the high- $k$  forced band  $\mathbb{K}_{p,p+3}$ . The first data point refers to the classical large-scale forcing only (run 1). Application of broadband forcing in the different bands changes the characteristics of the flow modifying primarily the amount of small scales. This forcing in the second band is seen to increase the energy dissipation in the system. The Kolmogorov dissipation scale and the Taylor-Reynolds number decrease, suggesting that the characteristic scale at which dissipation plays an important role is shifted to smaller scales. We notice that the total energy in the system is only slightly af-

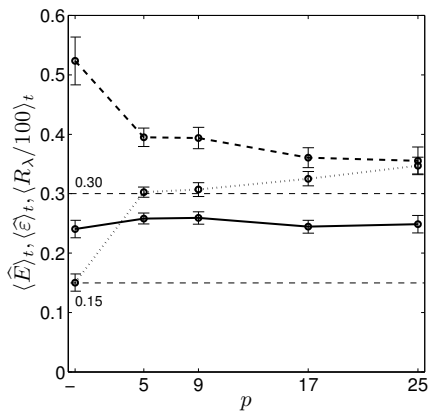


**Fig. 3.3:** Time-averaged total kinetic energy  $\widehat{E}$  (solid), total energy dissipation rate  $\widehat{\varepsilon}$  (dotted), and Taylor-Reynolds number  $R_\lambda$  (dashed) for forced turbulence with different locations of the second band at  $\text{Re} = 1061$ .

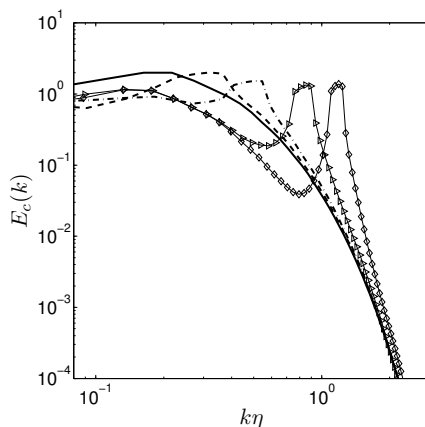


**Fig. 3.4:** Compensated shell- and time-averaged energy spectrum  $E_c(k)$  for two-band forcing:  $\mathbb{S}_1$  and  $\mathbb{K}_{p,p+3}$ . Large-scale forcing  $\mathbb{S}_1$  (solid), additional forcing in the second band  $\mathbb{K}_{5,8}$  (dashed),  $\mathbb{K}_{9,12}$  (dash-dotted),  $\mathbb{K}_{17,20}$  ( $\triangleright$ ),  $\mathbb{K}_{25,28}$  ( $\diamond$ ) at  $\text{Re} = 1061$ .

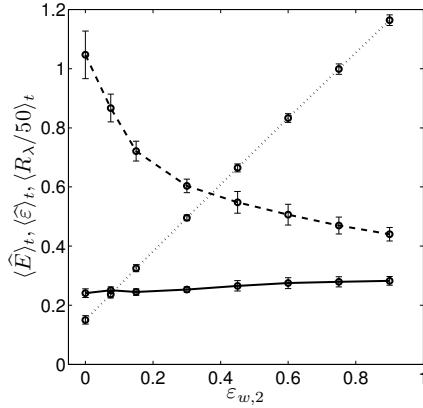


**Fig. 3.5:** Time-averaged total energy  $\widehat{E}$  (solid), total energy dissipation rate  $\widehat{\varepsilon}$  (dotted), and Taylor-Reynolds number  $R_\lambda$  (dashed) for two-band forced turbulence with varying strength in the second band  $\varepsilon_{w,2}$  at  $\text{Re} = 1061$ .

ected by the introduction of forcing. Moving the broadband forcing to very small scales implies that there is no longer a strong influence on the flow because the energy injected in the small scales appears to be also dissipated immediately.

The compensated, shell-, and time-averaged energy spectra for different locations of the forced region  $\mathbb{K}_{p,p+3}$  are shown in Fig. 3.4. We may observe that the forcing causes a nonlocal depletion in the energy spectrum for the larger scales while the tail of the spectrum is less affected. The pileup in the energy spectrum near the forcing region is characteristic of the explicit high- $k$  forcing and is suggestive of a “blocking” or reverse cascading. If the separation between  $\mathbb{S}_1$  and the high- $k$  band is reduced, then the interaction is stronger and a considerable depletion of the energy levels in the largest scales arises. This is in agreement with the large-scale forced turbulence results, where the local and nonlocal interactions were found to be energetically dominant while the distant interactions were mainly responsible for transferring structural information [12].

An effective modulation of turbulent quantities is possible not only by a change in the range of forced modes but also via a change in the energy input rate. To investigate this we adopted an energy injection rate  $\varepsilon_{w,1} = 0.15$



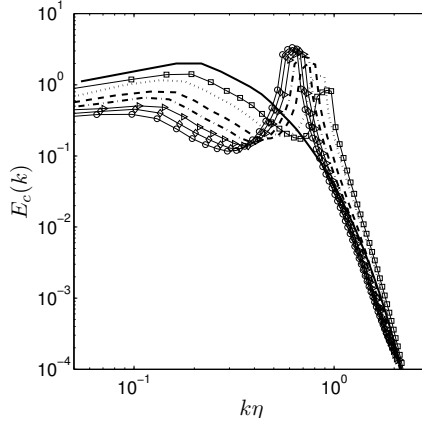


**Fig. 3.6:** Compensated shell- and time-averaged energy spectrum  $E_c(k)$  for forced turbulence in the band  $\mathbb{K}_{17,20}$  at different strengths of forcing  $\varepsilon_{w,2}$  and  $\text{Re} = 1061$ . Large-scale forcing only (solid), additional second band forcing with  $\varepsilon_{w,2} = 0.07, 0.15, 0.30, 0.45, 0.60, 0.75, 0.90$  denoted as  $\square$ , dotted, dashed, dash-dotted,  $\triangleright$ ,  $\diamond$ ,  $\circ$ , respectively. In each case  $\varepsilon_{w,1} = 0.15$ .

for the large-scale forcing in  $\mathbb{S}_1$  and we vary the intensity of forcing in the second band by changing  $\varepsilon_{w,2}$ . We adopted the following values for  $\varepsilon_{w,2}$ : 0.07, 0.15, 0.30, 0.45, 0.60, 0.75 or 0.90 and considered forcing of four or eight shells in  $\mathbb{K}_{17,20}$  or  $\mathbb{K}_{17,24}$ , respectively. The parameters and characteristic quantities can be found in Tables 3.1 and 3.2 as runs 2–7 and 8–13.

The total energy in the system is only slightly affected by the forcing strength in the second band as shown in Fig. 3.5. An increased forcing strength introduces additional energy into the flow at small scales that is dissipated very efficiently. This is expressed by the linear increase in  $\langle \hat{\varepsilon} \rangle_t$ . In Fig. 3.6 we present the compensated energy spectrum for various strengths of the forcing  $\varepsilon_{w,2}$ . The energy in the forced region reaches higher values with increasing  $\varepsilon_{w,2}$ . Changing the strength of the broadband forcing induces a characteristic depletion in the larger scales. This suggests that the additional forcing term enhances the nonlinear interactions, which influence various scales quite far away from the forced region. The energy that is injected at the larger scales is transferred even more effectively through

the cascade as  $\varepsilon_{w,2}$  increases. This effect appears similar to the so-called spectral shortcut observed in nature and experiments [31]. In the case of such a shortcut the energy from larger scales is diverted quite directly to fine scales largely bypassing the traditional cascading. This mechanism was explained in the case of flow over forest canopies in Ref. [31]. We will investigate it in more detail in the next section.

A final quantification of the nonlocal effect on the spectrum that arises from the high- $k$  forcing is collected in Fig. 3.7. Here we displayed the normalized accumulated energy

$$S_E(k) = \frac{\sum_{k' \leq k} E_c(k')}{\sum_k E_c(k)} \quad (3.24)$$

in the consecutive shells. As pointed out, varying the properties of a flow in a specified spectral region can change the behavior of a flow well outside this region. In terms of  $S_E(k)$  we notice that close to 90% of the energy is present in the first ten shells (Fig. 3.7) when only the large-scale forcing is applied. Influencing the flow at smaller scales in  $\mathbb{K}_{17,24}$  is seen to remove most of the energy from these larger scales while there is only a slight impact on the dynamics of small scales. This effect becomes more pronounced with increasing  $\varepsilon_{w,2}$ . The underlying changes in the energy transfer will be considered in more detail in Sec. 3.4.

### 3.3.2 Energy transfer spectra

The transfer of energy in turbulence can be described in spectral space as interactions of triads of wave vectors  $(\mathbf{k}, \mathbf{p}, \mathbf{q})$  that form triangles, i.e.,  $\mathbf{k} = \mathbf{p} + \mathbf{q}$ . Direct numerical simulation with large-scale forcing shows that nonlocal interactions between wave vectors combine into a local energy flow [111, 112]. By applying forcing that is located in a high- $k$  range of spectral space we perturb the “natural” cascading process. The associated changes in the transfer of energy will be investigated in more detail in this subsection. Specifically, we focus on the energy transfer and energy transport power spectra.

In large-scale forced turbulence energy is injected into the first shell and removed by the transfer term. This gives rise to negative values for the energy transfer in the forced region. In the higher shells the transfer function

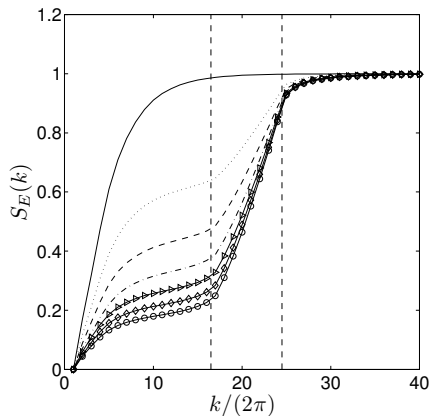


**Fig. 3.7:** Normalized accumulated energy  $S_E(k)$  for two-band  $\mathbb{S}_1$  and  $\mathbb{K}_{17,24}$  forced turbulence at  $Re = 1061$ . Large-scale forcing at  $\varepsilon_{w,1} = 0.15$  (solid) with additional second band forcing at  $\varepsilon_{w,2} = 0.15, 0.30, 0.45, 0.60, 0.75, 0.90$  is denoted by the dotted, dashed, dash-dotted,  $\triangleright$ ,  $\diamond$ , and  $\circ$  curves, respectively.

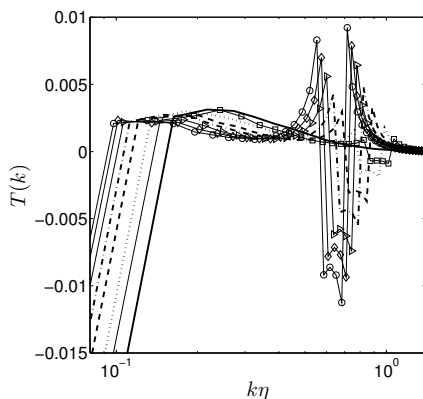


**Fig. 3.8:** Time-averaged energy transfer  $T(k)$  for two-band  $\mathbb{S}_1$  and  $\mathbb{K}_{17,20}$  forced turbulence for different strengths of forcing in the second band  $\varepsilon_{w,2}$  at  $Re = 1061$ . Large-scale forcing (solid) with additional second band forcing at  $\varepsilon_{w,2} = 0.07, 0.15, 0.30, 0.45, 0.60, 0.75, 0.90$  denoted by  $\square$ , dotted, dashed, dash-dotted,  $\triangleright$ ,  $\diamond$ , and  $\circ$  curves, respectively.

takes on positive values which illustrates the transfer of energy through the cascade toward higher  $k$ . By invoking the broadband forcing we influence this basic energy cascade. This is clearly seen in the energy transfer spectrum which develops distinctive regions where  $T(k) = \langle T(k, t) \rangle_t$  is negative. Figure 3.8 characterizes changes in the transfer function due to an increased forcing strength of the high- $k$  band. The transfer function reaches lower values between the low- and high- $k$  forcing regions compared to the large-scale forced case. The reverse situation appears near the high- $k$  forced band where the transfer increases with an increase of the forcing intensity. This is in agreement with the energy spectra presented earlier, where we observed the depletion of energy between the forced regions. This effect can be observed more directly from spectra of energy transport power that will be presented next.

The energy transport power gives the rate at which energy is transferred from shells  $k' < k$  to those with  $k' > k$ :

$$\Pi(k, t) = \int_k^{k_{\max}} T(k', t) dk' = - \int_0^k T(k', t) dk', \quad (3.25)$$

where  $k_{\max} = \pi N/L_b$  is the cutoff wave number. We present the time-averaged transport power spectrum  $\Pi(k) = \langle \Pi(k, t) \rangle_t$  in Fig. 3.9 for forcing with various strengths in the  $\mathbb{K}_{17,24}$  band. In case of large-scale forcing only, the transport power is positive for all  $k$  as the energy is transferred toward smaller scales and reaches zero for large  $k$  indicating the general property of the total transfer function  $\widehat{T}(t) = 0$ . The application of high- $k$  forcing for  $k_1 < k \leq k_2$  changes this well-known picture. First, we note that the values of the transport power are all similar in the largest scales, where the flow is governed by the same energy input. The transport power for  $0 < k \leq k_1$  becomes larger at higher  $\varepsilon_{w,2}$ . A striking change of the behavior arises for  $k$  near and inside the high- $k$  forced region. The transport power spectrum even assumes negative values for  $k \approx k_1$ .

The observed behavior of the transport power in Fig. 3.9 is partly due to the relatively low Reynolds number that was used. At sufficiently high Reynolds numbers, the dissipation scales are much more separated from the high- $k$  forced scales. In this case a plateau of  $\Pi$  will arise at low wave numbers:  $\Pi(k, t) \approx \varepsilon_{w,1}$  for  $k$  low enough [71]. This property is not observed

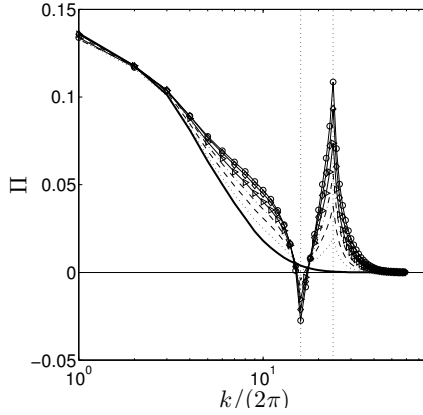


**Fig. 3.9:** Time-averaged transport power spectra for broadband-forced turbulence in the  $\mathbb{K}_{17,24}$  band at  $\text{Re} = 1061$ . Large-scale forcing (solid) with additional second band forced at  $\varepsilon_{w,2} = 0.15, 0.30, 0.45, 0.60, 0.75, 0.90$  denoted as dotted, dashed, dash-dotted,  $\triangleright$ ,  $\diamond$ ,  $\circ$  curves, respectively. The supplementary forced region  $k_1 < k \leq k_2$  is denoted with dotted lines.

at the computational Reynolds number considered so far.

In cases specified by runs 18 and 19 we consider the flow at a four times higher computational Reynolds number. The overall results for the energy spectra and energy transfer were found to be qualitatively the same as in the lower Reynolds number cases. However, a plateau may now be observed in Fig. 3.10, where we present the transport power for the higher Reynolds number. In this case the transport power does not decrease below zero in the forced region. The second forcing band is well separated from the dissipation region and the transport power in this band is much larger, approaching a maximum 0.23 that is near the energy injection rate  $\varepsilon_{w,2}$ .

In this section we have looked at the effect of high- $k$  modulation of the energy cascading process that leads to an increased energy dissipation in small scales. This process is supported by an increased energy transfer to smaller scales via nonlocal triad interactions. The effect of increased energy rate by the application of broadband forcing is seen in the energy transfer and transport power spectra. In the next section we will look more closely at the interactions of various scales of motion under the influence

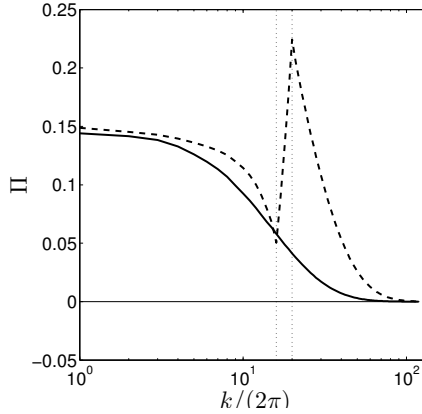


**Fig. 3.10:** Time-averaged transport power spectra for Reynolds number  $Re = 4243$  and forcing in the  $\mathbb{K}_{17,20}$  band. Large-scale forcing (solid), additional broadband forcing in the  $\mathbb{K}_{17,20}$  band with  $\varepsilon_{w,2} = 0.30$  (dashed).

of broadband forcing by considering the two- and three-mode transfers  $T_p$  and  $T_{pq}$  introduced in Eqs. (3.22) and (3.20).

### 3.4 Two- and three-mode interaction of scales

The energy dynamics of turbulent flow is generally discussed in terms of the transfer of kinetic energy from larger to smaller scales through nonlinear interactions. The statistical properties of turbulence are determined by these interactions. In the previous section we have shown how additional broadband forcing of inertial range scales can modify the classical picture of the Kolmogorov cascade. To investigate the observed turbulence modulation effects in more detail we consider the underlying two- and three-mode energy transfer terms in this section. This will clarify to some extent the changes in the various nonlinear interactions that give rise to the observed alterations in the spectra and energy transfer.

We start with the three-mode transfer that is averaged in time  $T_{pq}(k, k_p, k_q) = \langle T_{pq}(k, k_p, k_q, t) \rangle_t$  and split this term into its positive and negative parts:

$$T_{pq}(k, k_p, k_q) = T_{pq}^-(k, k_p, k_q) + T_{pq}^+(k, k_p, k_q), \quad (3.26)$$

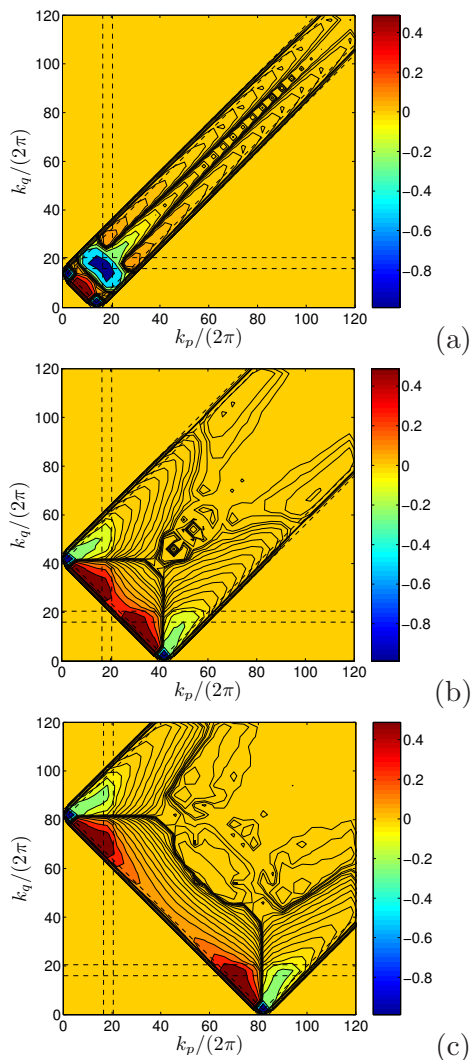


**Fig. 3.11:** The normalized triad energy transfer function  $\overline{T}_{pq}(k, k_p, k_q)$  for  $k/(2\pi) = 14, 42, 82$  in (a)–(c), respectively. The dashed lines correspond to the lower ( $k_1$ ) and upper ( $k_2$ ) wave numbers used in the broadband forcing at  $\text{Re} = 4243$ . The contour levels are  $\pm 1/2^n$ ,  $n = 0, \dots, 18$  that are the same for all three pictures.

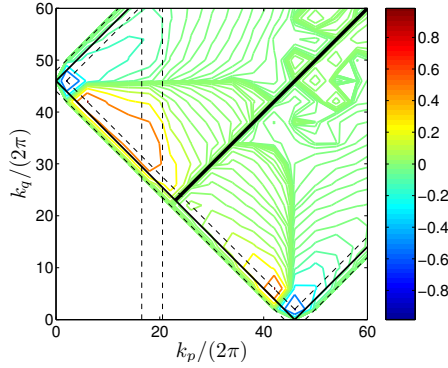


**Fig. 3.12:** The normalized triad energy transfer function  $\overline{T}_{pq}(k, k_p, k_q)$  for  $k/(2\pi) = 46$  at  $\text{Re} = 4243$ . The upper (bottom) rectangle presents broadband (large-scale) forced turbulence, respectively. The contour levels are  $\pm 1/2^n$ ,  $n = 0, \dots, 24$ .

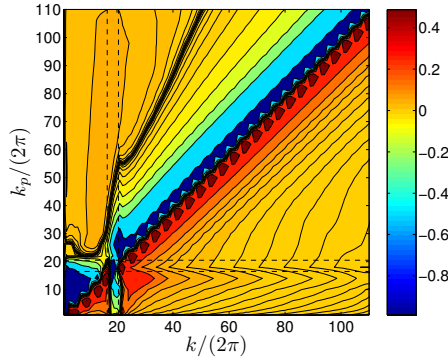


**Fig. 3.13:** The normalized triad energy transfer function  $\overline{T}_p(k, k_p)$  at  $\text{Re} = 4243$  (run 19). The contour levels are  $\pm 1/2^n$ ,  $n = 0, \dots, 18$ . The supplementary forced region  $k_1 < k \leq k_2$  denoted with dashed lines.

in which

$$T_{pq}^+(k, k_p, k_q) = \begin{cases} T_{pq}(k, k_p, k_q) & \text{if } T_{pq}(k, k_p, k_q) \geq 0, \\ 0 & \text{otherwise,} \end{cases} \quad (3.27)$$



with a similar definition for the negative part:

$$T_{pq}^-(k, k_p, k_q) = \begin{cases} T_{pq}(k, k_p, k_q) & \text{if } T_{pq}(k, k_p, k_q) < 0, \\ 0 & \text{otherwise.} \end{cases} \quad (3.28)$$

In terms of these contributions we examine the normalized triad energy transfer

$$\bar{T}_{pq}(k, k_p, k_q) = \frac{T_{pq}^-(k, k_p, k_q)}{T_{\min}(k)} + \frac{T_{pq}^+(k, k_p, k_q)}{T_{\max}(k)}, \quad (3.29)$$

where

$$\begin{aligned} T_{\min}(k) &= -\min_{k_p, k_q} (T_{pq}^-(k, k_p, k_q)), \\ T_{\max}(k) &= \max_{k_p, k_q} (T_{pq}^+(k, k_p, k_q)). \end{aligned} \quad (3.30)$$

Through the scaling of  $T_{pq}^-$  and  $T_{pq}^+$  with  $T_{\min}$  and  $T_{\max}$ , respectively, the normalized transfer is well suited to characterize the overall structure of the three-mode transfer function, even in cases in which the order of magnitude of  $T_{pq}$  varies considerably. The normalized energy transfer  $\bar{T}_{pq}(k, k_p, k_q)$  is plotted in Fig. 3.11 for three different wave numbers  $k/(2\pi) = 14, 42, 82$ , based on Run 19 in which  $R_\lambda \cong 75$ . The three  $k$  values that are selected correspond to wave numbers below the forced region [ $k/(2\pi) = 14$ ] or to wave numbers that are considerably larger. Such contour maps for  $\bar{T}_{pq}$  can also be found in Ref. [84] for the case of large-scale forced turbulence. For completeness, we also presented the results from such large-scale forced turbulence (run 18) comparing these directly to the broadband-forced turbulence (run 19). This contour map is shown in Fig. 3.12 for  $k/(2\pi) = 46$ .

The strongest interactions are observed for modes with wave numbers between the largest forced scales and the high- $k$  forced region as can be seen in Fig. 3.11(a). As in the case of large-scale forcing only we observe very strong interactions between Fourier modes of considerably different scales. These are located in the corners of the rectangular domains in the  $k_p$ - $k_q$  plane. Distant interactions are well separated from the origin in these figures. Their contribution to the transfer is seen to be very small, as also noticed earlier in the literature [84]. The change of sign in the transfer function that occurs at  $k_p = k$  and  $k_q = k$ , respectively, on the  $k_p$ - $k_q$  planes indicates that in this region the energy is mainly transferred to higher  $k$ .

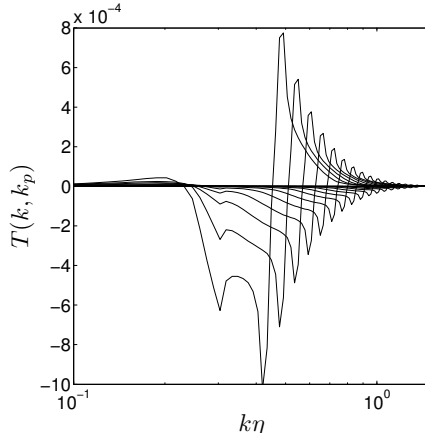


**Fig. 3.14:** The triad energy transfer function  $T_p(k, k_p)$  at  $k_p/(2\pi) = 30, 34, \dots, 94$  and  $\text{Re} = 4243$  (run 19).

The most efficient transfer takes place between two wave vectors of similar size and one of quite different size as seen in the corners of the rectangular area in Fig. 3.11. This is in agreement with previous numerical experiments reported by various authors [28, 84, 113]. However, compared to the case of large-scale forcing only, we now observe quite extended, highly energetic interactions with the high- $k$  forced region. The second forced band causes regions with high intensity of interactions to be much wider compared to the case of large-scale forcing only. This is visible directly in Fig. 3.12. The regions with positive and negative transfer are extended from the corners to the wave-number regions where the actual application of forcing in the second band occurs. The energy is exchanged predominantly between scales that are more separated than in case of the large-scale forced flow where the dominant interactions occur only in the corners. This is a clear indication of the stronger nonlocal interactions, mentioned earlier.

For further clarification of energy transfer processes we turn to the time-averaged two-mode energy transfer  $T_p(k, k_p) = \langle T_p(k, k_p) \rangle_t$ , which gives information about the interactions involving a sum over all  $k_q$  wave numbers at fixed  $k$  and  $k_p$ . The sum involves all  $k_q$  wave numbers that are constrained by the triadic interactions, i.e., their length may vary between

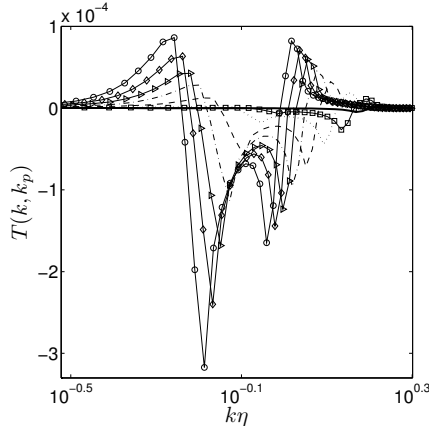


**Fig. 3.15:** The triad energy transfer function  $T_p(k, k_p)$  at  $k_p/(2\pi) = 30$  and  $\text{Re} = 1061$ . Large-scale forcing (solid) with additional second band forced at  $\varepsilon_{w,2} = 0.07, 0.15, 0.30, 0.45, 0.60, 0.75, 0.90$  denoted as  $\square$ , dotted, dashed, dash-dotted,  $\triangleright$ ,  $\diamond$ ,  $\circ$ , respectively.

$|\mathbf{k} - \mathbf{p}|$  and  $|\mathbf{k} + \mathbf{p}|$ . We normalized the two-mode transfer function  $T_p(k, k_p)$  in a similar manner as  $T_p(k, k_p, k_q)$ :

$$\bar{T}_p(k, k_p) = \frac{T_p^-(k, k_p)}{T_{\min}(k)} + \frac{T_p^+(k, k_p)}{T_{\max}(k)}, \quad (3.31)$$

where  $T_p^\pm$ ,  $T_{\min}$ , and  $T_{\max}$  are defined in terms of  $T_p$  in a manner analogous to the definitions in Eqs. (3.26), (3.27), (3.28) and (3.30). In Fig. 3.13 we plotted the contour map of  $\bar{T}_p(k, k_p)$ . For larger wave numbers this quantity was found to look quite similar to the case of large-scale forced turbulence. The two-mode transfer function changes sign from negative to positive at  $k = k_p$  indicating a downward energy flow. Comparing this to the large-scale forced turbulence we observe (i) strong influence of forcing in the regions where it is applied (denoted with dashed lines), (ii) extended negative energy transfer region with comparatively high magnitude above the  $k = k_p$  line, (iii) amplification of the backward energy transfer indicated by the positive region for small  $k$  and large  $k_p$ . This region is separated from the intense negative energy transfer region by the indicated accumulation of contour lines above the  $k = k_p$  line appearing as the curved black line.

A more quantitative overview is plotted in Fig. 3.14 displaying the two-mode transfer function in the range  $k_p/(2\pi) = 30, 34, \dots, 94$ . This clearly shows the cascading character of the energy flow from larger to smaller scales in the system. The modification due to the high- $k$  forcing expresses itself by the sequence of one slightly positive, two quite negative and one quite positive local extrema. The intensity of the energy transfer decreases with increasing wave numbers as less energy needs to be transferred. This corresponds directly to the magnitude of  $T_{\min}(k)$  and  $T_{\max}(k)$  used in the normalization of  $T_p(k, k_p)$  [Eq. 3.31]. The part in which the transfer is negative is much wider in the broadband-forced case compared to the large-scale forced turbulence results.

We conclude by considering the effect of varying the forcing strength  $\varepsilon_{w,2}$  at a characteristic wave number  $k_p/(2\pi) = 30$  on the two-mode energy transfer function  $T_p(k, k_p)$  [Fig. 3.15]. In the large-scale forced case at  $\varepsilon_{w,2} = 0$  the transfer is very small compared to the cases in which the high- $k$  forcing is active. In addition, the effect is very localized (solid line in Fig. 3.15). The forcing in the high- $k$  band completely changes this behavior. The intensity of the energy transfer is directly related to the value of  $\varepsilon_{w,2}$ . Additional extrema appear in the two-mode transfer function. The high- $k$  forced cases display two pairs in which a negative minimum is combined with a positive maximum, while large scale forcing only yields one such combination. Correspondingly, the min-max pair at high  $k$  is associated with the large scale forcing in  $\mathbb{S}_1$  while the min-max pair at lower  $k$  originates from the additional forcing in the second band. We also investigated three-band forcing and observed further peaks in the energy transfer spectra.

### 3.5 Conclusions

We performed direct numerical simulations of broadband-forced turbulence to explore accumulated effects on the time-averaged energy transfer in isotropic homogeneous turbulence. Using broadband forcing based on a recently proposed mathematical model for a fractal stirrer [70] we have shown how the application of such forcing modulates turbulence both qualitatively and quantitatively. The modulation is similar to that observed in experiments based on flows through porous media or canopies. Specifically

the perturbation of a flow arising from the contact with complex physical boundaries enhances the dissipation and causes an abrupt energy drain from large to small scales. This aspect of simultaneous perturbation of a flow on a spectrum of length scales is retained in the cases studied here.

We found that broadband forcing that perturbs a turbulent flow at smaller scales enhances nonlocal triad interactions and alters the detailed cancellation processes that occur in the traditional large-scale forced flows. This leads to nonlocal modifications in the energy transfer spectrum and the energy distribution among scales. We verified this by partitioning the nonlinear term in the Navier–Stokes equations in terms of different triad contributions to the total transfer function. The energy transport power is found to be enhanced in the spectral region in between the large-scale and the high- $k$  forced bands. This characteristic may be influenced via the control parameters of the applied forcing, i.e., its strength and extent of agitated scales, and allows optimizing transport processes of turbulent flows.

Future study will involve the examination of the consequences of forcing in the physical space context. We will investigate the geometrical statistics of broadband-forced turbulence looking at the interactions of strain and vorticity and their modulation by the applied forcing. This may help understanding which physical processes are responsible for the observed modulations and how to exploit this to enhance physical space mixing.

## Appendix

The main parameters of the simulations are collected in Table 3.1. The corresponding statistics of the velocity fields are summarized in Table 3.2. The quantities compiled in Table 3.2 are the Kolmogorov dissipation wave number  $k_d$  which is the inverse of the Kolmogorov length scale  $\eta$ , the product  $k_{\max}\eta$ , the Taylor microscale  $\lambda = [5\hat{E}/\sum_{\mathbf{k}} k^2 E(\mathbf{k}, t)]^{1/2}$ , the Taylor-microscale Reynolds number  $R_\lambda = \lambda u'/\nu$ , the integral length scale  $L = 3\pi/(4\hat{E}) \sum_{\mathbf{k}} k^{-1} E(\mathbf{k}, t)$ , the integral Reynolds number  $R_L = Lu'/\nu$ , the rms velocity  $u' = (2\hat{E}/3)^{1/2}$ , the energy-dissipation rate  $\varepsilon = \sum_{\mathbf{k}} 2\nu k^2 E(\mathbf{k}, t)$ , the eddy-turnover time  $\tau = L/u'$  and the skewness  $S = 2/35 (\lambda/u')^3 \sum_{\mathbf{k}} k^2 T(\mathbf{k}, t)$ . All these quantities in Table 3.2 are time averaged  $\langle \cdot \rangle_t$  as described in Sec. 3.2.4.

Run	$\varepsilon_w$	$m$	$p$	Run	$\varepsilon_w$	$m$	$p$
1	0.15*	—	—				
2	0.07	17	20	8	0.15	17	24
3	0.30	17	20	9	0.30	17	24
4	0.45	17	20	10	0.45	17	24
5	0.60	17	20	11	0.60	17	24
6	0.75	17	20	12	0.75	17	24
7	0.90	17	20	13	0.90	17	24
14	0.15	5	8	18	0.15*	—	—
15	0.15	9	12	19	0.30	17	20
16	0.15	17	20				
17	0.15	25	28				

**Table 3.1:** Direct numerical simulation parameters using a resolution of  $N = 128$  and  $\text{Re} = 1061$  in runs 1–17, and a resolution of  $N = 256$  at  $\text{Re} = 4243$  in runs 18–19. The cases with large-scale forcing only are denoted by  $\star$ . In this table  $\varepsilon_w$  denotes the energy input rate in the high- $k$  band, except runs 1 and 18 in which it corresponds to the energy input rate in  $\mathbb{S}_1$ . Moreover,  $m$  and  $p$  characterize the spectral support of the high- $k$  band  $\mathbb{K}_{m,p}$ .

We also checked that the alteration of the cascading process caused by the high- $k$  forcing does not influence the isotropy of the flow field. A measure of isotropy was suggested in Ref. [23] given by  $I^2(t) = \psi_1(t)/\psi_2(t)$  where  $\psi_1(t) = \langle |\mathbf{e}_1(\mathbf{k})\mathbf{u}(\mathbf{k}, t)|^2 \rangle$ ,  $\psi_2(k, t) = \langle |\mathbf{e}_2(\mathbf{k})\mathbf{u}(\mathbf{k}, t)|^2 \rangle$  are the kinetic energy along the components of two orthogonal solenoidal unit vectors  $\mathbf{e}_1(\mathbf{k}) = \mathbf{k} \times \mathbf{z}(\mathbf{k})/|\mathbf{k} \times \mathbf{z}(\mathbf{k})|$ ,  $\mathbf{e}_2(\mathbf{k}) = \mathbf{k} \times \mathbf{e}_1(\mathbf{k})/|\mathbf{k} \times \mathbf{e}_1(\mathbf{k})|$  where  $\mathbf{z}(\mathbf{k})$  is a randomly oriented unit vector. The operator  $\langle \cdot \rangle$  denotes averaging over these random unit vectors. For isotropic turbulence one can expect to find  $I = 1$ , i.e.,  $\psi_1 = \psi_2$  which was confirmed to close approximation in all simulations. Deviations from the expected value for  $I$  were found to be of the order of 1%.

Run	$k_d$	$k_{\max}\eta$	$\lambda$	$R_\lambda$	$L$	$R_L$	$u'$	$\varepsilon$	$\tau$	$S$
1	116	3.26	0.123	52	0.23	97	0.40	0.15	0.57	0.49
2	130	2.91	0.100	43	0.23	100	0.41	0.24	0.56	0.35
3	156	2.42	0.069	30	0.23	98	0.41	0.50	0.54	0.21
4	168	2.25	0.061	27	0.23	101	0.42	0.66	0.54	0.17
5	178	2.12	0.056	25	0.22	102	0.43	0.83	0.52	0.15
6	186	2.03	0.051	23	0.22	102	0.43	1.00	0.52	0.14
7	193	1.95	0.048	22	0.22	100	0.43	1.16	0.50	0.13
8	140	2.68	0.085	37	0.23	99	0.41	0.33	0.56	0.29
9	156	2.41	0.070	31	0.23	102	0.41	0.50	0.56	0.22
10	169	2.24	0.060	26	0.22	98	0.41	0.68	0.54	0.18
11	178	2.11	0.054	24	0.22	100	0.42	0.85	0.53	0.16
12	187	2.02	0.049	22	0.22	97	0.42	1.03	0.52	0.15
13	194	1.94	0.046	21	0.21	96	0.42	1.20	0.50	0.13
14	138	2.73	0.090	39	0.22	96	0.41	0.30	0.52	0.44
15	138	2.72	0.089	39	0.23	102	0.42	0.31	0.56	0.39
16	140	2.69	0.084	36	0.22	96	0.40	0.33	0.55	0.28
17	143	2.64	0.082	36	0.23	98	0.41	0.35	0.56	0.22
18	325	2.32	0.065	115	0.21	368	0.42	0.15	0.50	0.51
19	432	1.74	0.040	75	0.21	394	0.44	0.46	0.47	0.38

**Table 3.2:** Direct numerical simulations statistics of the different cases studied.

## Acknowledgments

This work is part of the research program ‘‘Turbulence and its role in energy conversion processes’’ of the Foundation for Fundamental Research of Matter (FOM). The authors wish to thank NCF (Dutch Foundation for National Computing Facilities) for supporting the computations. These were executed at SARA Computing and Networking Services in Amsterdam.





# Chapter 4

## Response maxima in periodically forced turbulence<sup>†</sup>

The response of turbulent flow to time-modulated forcing is studied by direct numerical simulations of the Navier–Stokes equations. The large-scale forcing is modulated via periodic energy-input variations at frequency  $\omega$ . The response is maximal for frequencies in the range of the inverse of the large-eddy turnover time, confirming the mean-field predictions of von der Heydt, Grossmann and Lohse (Phys. Rev. E 67, 046308 (2003)). In accordance with the theory the response maximum shows only a small dependence on the Reynolds number. At sufficiently high frequencies the amplitude of the kinetic energy response decreases as  $1/\omega$ . For frequencies beyond the range of maximal response, a significant change in the phase-shift relative to the time-modulated forcing is observed. For large  $\omega$  the phase shift approaches roughly  $90^\circ$  for the total energy and  $180^\circ$  for the energy-dissipation rate.

### 4.1 Introduction

Recently, response maxima in time modulated turbulence have been predicted within a mean field theory of turbulence [44]. Subsequently, such response maxima were found [45] in numerical simulations of simplified dynamical turbulence models such as the GOY model [5, 10, 53] or the reduced wave vector approximation (REWA) [29, 39, 40, 41].

---

<sup>†</sup>“*Response maxima in time-modulated turbulence: Direct Numerical Simulations*” by A. K. Kuczaj, B. J. Geurts, and D. Lohse appeared in Europhysics Letters 73 (6), 2006 [61].

However, these response maxima computed in Ref. [45] were not pronounced at all, due to the approximate treatment of the small scales in either of these approaches. Indications of response maxima resulting from time-modulated forcing have subsequently also been seen in experiment [15]. The experimental observations were done by introducing a time-dependent swirl to fluid in a closed container and monitoring the energy injection rate. The selected set-up did not allow to identify possible flow structuring under resonance conditions, nor to conclusively distinguish such resonance phenomena from flow organization associated with the size of the container. Earlier, response functions of jet turbulence and thermally driven turbulence were measured [18, 16]. The response of various space dependent quantities in turbulent channel flow to periodically forced oscillations was examined in Ref. [96]. There the boundary layers and thus the anisotropy of the flow play a major role, but go beyond the scope of presented work; their role is a possible direction of further numerical investigations.

The purpose of this paper is to complement these theoretical, numerical, and experimental observations by direct numerical simulations (DNS) of turbulence, subject to time-modulated large-scale forcing. In a turbulent flow whose large-scale forcing is periodically modulated in time, all typical flow properties develop a complex time-dependence. However, averaging such turbulent time-dependence, conditioned on the phase of the periodic modulation, yields a clear and much simpler periodic pattern [45]. The dependence of the conditionally averaged response on the frequency of the modulation may be quantified by monitoring changes in flow properties such as total energy, energy-dissipation rate, or Taylor-Reynolds number. In case of a fast modulation with a frequency  $\omega \gg \omega_L$ , where  $\omega_L$  is the inverse large-eddy turnover time, only a modest effect on the flow is expected, or none at all. Likewise, if  $\omega \ll \omega_L$  the modulation is quasistationary and the flow may be expected to closely resemble the corresponding unmodulated case. In between these extremes a more pronounced response may develop, which is the subject of this investigation.

The DNS approach allows to investigate in detail the response of turbulent flow properties to periodic modulation of the forcing. In particular, we present a parameter study involving a large range of modulation frequencies for two different Reynolds numbers, and establish response maxima in a variety of flow properties. The response is found to be signifi-

cantly increased at modulation frequencies on the order of the inverse of the eddy-turnover time. Near resonance, the “activity” of the turbulent flow is found to be considerably higher than in the unmodulated case. At high frequencies  $\omega$  the amplitude of the modulation-specific response of the kinetic energy is found to uniformly decrease to zero as  $\omega^{-1}$ . This type of external control of turbulence may offer new opportunities with relevance to technological applications, e.g., increased mixing efficiency.

First, the computational flow model is introduced. Subsequently, an overview of the ensemble averaging procedure and data extraction is given. Then the main result, the response of various flow properties to time-modulated forcing, is presented.

## 4.2 Computational flow model

The full Navier–Stokes equations for incompressible flow are numerically solved in a periodic flow domain with a pseudo-spectral code. In spectral space, the Navier–Stokes equations read

$$\left(\frac{\partial}{\partial t} + \nu|\mathbf{k}|^2\right) u_\alpha(\mathbf{k}, t) = M_{\alpha\beta\gamma}(\mathbf{k}) \sum_{\mathbf{p}+\mathbf{q}=\mathbf{k}} u_\beta(\mathbf{p}, t) u_\gamma(\mathbf{q}, t) + F_\alpha(\mathbf{k}, t), \quad (4.1)$$

with  $M_{\alpha\beta\gamma}(\mathbf{k}) = \frac{1}{2i} \left( k_\beta D_{\alpha\gamma}(\mathbf{k}) + k_\gamma D_{\alpha\beta}(\mathbf{k}) \right)$  and  $D_{\alpha\beta}(\mathbf{k}) = \delta_{\alpha\beta} - k_\alpha k_\beta / |\mathbf{k}|^2$ . Here,  $\nu$  is the kinematic viscosity,  $u_\alpha(\mathbf{k}, t)$  is the Fourier coefficient of the velocity field at wave vector  $\mathbf{k}$  and time  $t$ , and  $F_\alpha$  is the time-modulated forcing.

First, we recall that traditional agitation of the large-scale structures in a turbulent flow may be achieved by introducing a forcing term restricted to wave vectors with  $|\mathbf{k}| \leq k_F$ , i.e., identifying a forcing range through the upper-limit  $k_F$ . Specifically, we force the turbulence similarly as in Refs. [41, 36],

$$f_\alpha(\mathbf{k}, t) = \frac{\varepsilon_w}{N_F} \frac{u_\alpha(\mathbf{k}, t)}{|\mathbf{u}(\mathbf{k}, t)|^2} \quad ; \quad |\mathbf{k}| \leq k_F, \quad (4.2)$$

where  $\varepsilon_w$  is the constant energy injection rate and  $N_F = N_F(k_F)$  is the total number of forced modes. For convenience, the wave vectors are grouped in

spherical shells with the  $n$ th shell containing all modes such that  $\frac{2\pi}{L_b}(n - 1/2) < |\mathbf{k}| \leq \frac{2\pi}{L_b}(n + 1/2)$ , where  $L_b$  is the box-size in physical space. We apply large-scale forcing either in the first shell (i.e.,  $k_F = 3\pi/L_b$ , which implies  $N_F = 18$ , the case considered in Ref. [45]) or in the first two shells (i.e.,  $k_F = 5\pi/L_b$ , which implies  $N_F = 80$ ). The second step in specifying the forcing  $F_\alpha$  introduces the periodic time modulation

$$F_\alpha(\mathbf{k}, t) = f_\alpha(\mathbf{k}, t) \left(1 + A_F \sin(\omega t)\right), \quad (4.3)$$

where  $A_F$  is the amplitude of modulation and  $\omega$  its angular frequency. The modulated forcing corresponds to a total energy-input rate, which oscillates around  $\varepsilon_w$  with amplitude  $A_F$ ,

$$T_F(\omega, t) = \sum_{\mathbf{k}} u_\alpha^*(\mathbf{k}, t) F_\alpha(\mathbf{k}, t) = \varepsilon_w \left(1 + A_F \sin(\omega t)\right). \quad (4.4)$$

The length and time scales of the numerical simulation are chosen by picking  $L_b = 1$  for the box size in physical space, and  $\varepsilon_w = 0.15$  for the energy injection rate. The Reynolds number is then determined by the dimensionless viscosity  $\nu$ . Choosing  $\nu^{-1} = 1061$  and  $\nu^{-1} = 4243$  result in respective Taylor-Reynolds numbers  $R_\lambda \cong 50$  and  $R_\lambda \cong 100$ . We use these two cases as references denoted by  $R_{50}$  and  $R_{100}$ .

The spatial resolution needed may be estimated by requiring  $k_{\max}\eta > 1$  [86] with  $\eta$  the Kolmogorov dissipation scale and  $k_{\max}$  the highest wave number included in the spatial discretization. For the  $R_{50}$  case a resolution of at least  $64^3$  computational points is required while for  $R_{100}$  a higher resolution of  $192^3$  points is necessary. The latter poses a strong computational challenge in view of the extensive ensemble averaging and large number of modulation frequencies. However, it was found that many large scale quantities, such as the total energy, do not depend too sensitively on resolution. As an example, a resolution of  $64^3$  points corresponds to  $k_{\max}\eta \approx 0.4$  for the  $R_{100}$  case. Still, this resolution is quite adequate for studying the response of the total energy. This was verified by repeating the analysis at a selection of modulation frequencies with resolutions  $128^3$  and  $192^3$ . The predictions of quantities that rely more on small scales, such as the dissipation rate, contain a higher numerical uncertainty for  $R_{100}$  case and  $64^3$  computational points, but still allow a clear interpretation of the main turbulence response. This was separately assessed using

the higher resolution data at selected characteristic frequencies. The direct numerical simulation for the unmodulated case starts from an initial condition that was generated on the basis of the Pao spectrum [86]. We adopt exactly the same initial conditions as in Ref. [77], which allow a separate validation of the simulations. Explicit second order compact-storage Runge-Kutta time-stepping [35] with fully de-aliased pseudo-spectral discretization is used. The unmodulated turbulent flows provide the point of reference for investigating the effect of modulated forcing, to which we turn next.

### 4.3 Averaging procedure and simulation setting

In order to analyze the response to a time-modulated forcing, the precise extraction of the amplitude and phase of the conditionally averaged variations is a key issue. Two steps can be distinguished, i.e., the computation of the conditionally averaged signal itself and the subsequent determination of amplitude and phase characteristics of this signal, see Fig. 4.1.

We adopt ensemble averaging to determine the conditionally averaged signal  $S(\omega, t)$ , where  $S(\omega, t)$  is the total energy  $E(\omega, t)$ , the Taylor-Reynolds number  $R_\lambda(\omega, t)$ , or the energy-dissipation rate  $\varepsilon(\omega, t)$ . Ensemble averaging requires a sufficiently large sample of statistically independent signals  $\{S_j(\omega, t)\}$  to be generated. We compute the unmodulated flow and store  $N_r$  realizations of the turbulent solution corresponding to  $t > 10$ . The latter condition allows transients related to the initial condition to become negligible. The time separation between these snapshots is larger than two eddy-turnover times. Subsequently, each of these  $N_r$  realizations was taken as the initial condition for a simulation with time-modulated forcing at a particular frequency  $\omega$ . This provides  $N_r$  sample signals that need to be averaged to obtain the conditionally averaged signal  $S(\omega, t)$ . Repeating this procedure for a range of frequencies yields the total response characteristics. Given the conditionally averaged response signal  $S(\omega, t)$ , there are various ways in which amplitude and phase information can be extracted. In Ref. [15] the signal  $S(\omega, t)$  is first averaged over time to yield  $\overline{S}(\omega)$ . Subsequently, the normalized variation defined as  $Q_S^{(a)}(\omega, t) = S(\omega, t)/\overline{S}(\omega)$  is studied using the Fourier transform ( $\mathcal{F}$ ) in which time  $t$  is transformed into frequency  $f$ . Correspondingly, the power

amplitude spectrum  $\widehat{Q}_S^{(a)}(\omega, f) = \mathcal{F}(Q_S^{(a)}(\omega, t) - 1)$  can be obtained, which assumes a maximum value  $A_S(\omega) = \max\{|\widehat{Q}_S^{(a)}(\omega, f)|\}_{f=f_A(\omega)}$ , as denoted in Fig. 4.1 for forcing  $A_F(\omega)$ , total energy  $A_E(\omega)$ , and energy-dissipation rate  $A_\varepsilon(\omega)$ . The maximum  $A_S(\omega)$  as the amplitude at dominant frequency can be used to quantify the response as function of the modulation frequency  $\omega$ . This approach is accurate if the Fourier transformation is applied to an integer number of modulation periods. The method used in Ref. [45] is based on a fitting procedure in which it is assumed that  $S(\omega, t) \approx \bar{S} + A_S \sin(\omega t + \Phi_S)$ . The dependence of the parameters  $\{\bar{S}, A_S, \Phi_S\}$  on  $\omega$  may be obtained from a least squares procedure. This evaluation method assumes that the conditionally averaged signal has the same frequency as the forcing.

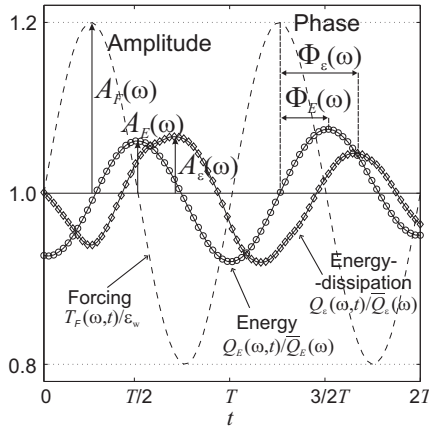


**Fig. 4.1:** The amplitudes  $A_F(\omega)$ ,  $A_E(\omega)$ ,  $A_\varepsilon(\omega)$  and phase-shifts  $\Phi_F(\omega) \equiv 0$ ,  $\Phi_E(\omega)$ ,  $\Phi_\varepsilon(\omega)$  of the forcing  $T_F(\omega, t)$  (dashed line), the energy  $Q_E(\omega, t)$  (labeled  $\circ$ ), and the energy-dissipation rate  $Q_\varepsilon(\omega, t)$  (labeled  $\diamond$ ) normalized by their respective means  $\bar{T}_F = \varepsilon_w$ ,  $\bar{Q}_E(\omega)$ , and  $\bar{Q}_\varepsilon(\omega)$  obtained from simulations at the modulation frequency  $\omega = 0.8\pi$ .

At modest ensemble size  $N_r$  it is beneficial to explicitly incorporate variations in the unmodulated reference signal to improve the data evaluation. This motivates an alternative method in which we determine  $N_r$  sample signals  $\{S_j(\omega, t)\}$  corresponding to the modulated case, as well as  $N_r$  unmodulated signals  $\{s_j(t)\}$  that start from the same set of initial conditions.

This allows to generate different “normalized” signals such as  $Q_S^{(b)}(\omega, t) = \sum_j S_j / \sum_j s_j$  or  $Q_S^{(c)}(\omega, t) = \sum_j S_j / s_j / N_r$ . These normalized signals provide estimates that compensate to some degree for the relatively small number of samples or for an unknown mean component but have the drawback that they cannot be applied in the context of a physical experiment. Additionally, we divided these signals by its means (time-averages) and removed the constant component corresponding to the zero-frequency response. Application of the Fourier transform,  $\widehat{Q}_S^{(b)} = \mathcal{F}(Q_S^{(b)} / \overline{Q}_S^{(b)} - 1)$  and  $\widehat{Q}_S^{(c)} = \mathcal{F}(Q_S^{(c)} / \overline{Q}_S^{(c)} - 1)$ , provides direct access to amplitude and phase information. Each of these methods yields the same general impression of response maxima in time-modulated turbulence. Differences arise only on a more detailed level of the processed data but these do not obscure the interpretation of the main features of the response. Therefore we only present results extracted from the normalized signal  $Q_S / \overline{Q}_S \equiv Q_S^{(c)} / \overline{Q}_S^{(c)}$ , unless explicitly stated otherwise.

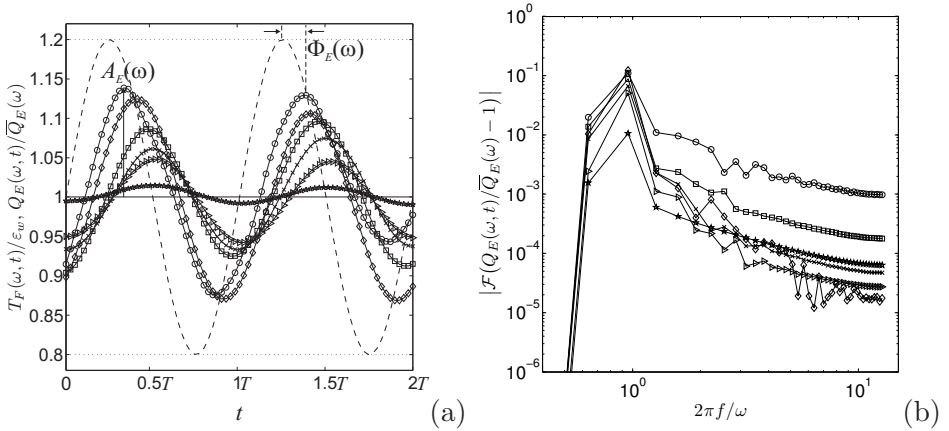


**Fig. 4.2:** The response  $Q_E(\omega, t) / \overline{Q}_E(\omega)$  for the  $R_{50}$  case recorded at different modulation frequencies  $\omega$  is shown in (a) together with the modulation of the forcing  $T_F(\omega, t) / \varepsilon_w$  (dashed). The corresponding power spectra of the Fourier transform as function of the transformed frequency  $f$  are collected in (b). Modulation frequencies  $\omega / (2\pi) = 0.1, 0.2, 0.3, 0.4, 0.5, 2.0$  are included and labeled by  $\circ, \diamond, \square, \times, \triangleright, \star$ , respectively.

The simulations were performed in the frequency range  $\pi/5 \leq \omega \leq 80\pi$  with time-modulated forcing at an amplitude  $A_F = 1/5$ . For each of the  $N_r$  unmodulated initial conditions,  $n_T = 4$  periods of the modulated forcing were simulated, i.e., each sample signal was computed for  $n_T T$  time-units with modulation-period  $T = 2\pi/\omega$ . Since an explicit time-stepping method was adopted, the cases at low  $\omega$  add particularly to the total computational cost. The number of realizations required in the ensemble was investigated separately. Results for several modulation frequencies were compared at  $N_r = 10, 30$  and  $50$ ; it was found that 30 independent samples provide adequate statistical convergence for our purposes. We stored  $N_t = 40$  points per modulation period and present results obtained by evaluating the last two recorded periods, i.e.,  $2T \leq t \leq 4T$ . Comparison with results obtained by evaluating data on  $0 \leq t \leq 4T$  yielded only minor differences. Finally, the phase  $\Phi_S(\omega)$  between the forcing and the response can be computed from the Fourier-transformed data as well. At the dominant frequency  $f_A$  of the transformed signal  $\widehat{Q}_S(\omega, f) = \mathcal{F}(Q_S(\omega, t))/\overline{Q}_S(\omega, t) - 1$ , the phase becomes  $\Phi_S(\omega) = \arctan(\text{Im}(\widehat{Q}_S(\omega, f_A))/\text{Re}(\widehat{Q}_S(\omega, f_A)))$ .

## 4.4 Modulated turbulence

In Fig. 4.2(a) the conditionally averaged signal  $Q_E(\omega, t)/\overline{Q}_E(\omega)$  based on total energy is shown at a number of modulation frequencies. The conditionally averaged response has a clear oscillatory behavior. The Fourier transform of the data from Fig. 4.2(a) is shown in Fig. 4.2(b) and displays a dominant maximum corresponding to the forcing frequency  $f_A = \omega/(2\pi)$ . This observation confirms that the least-squares fitting procedure adopted in Ref. [45] is justified.

We now focus on the amplitude of the total energy response as function of the modulation frequency  $\omega$ . The amplitude  $A_E(\omega)$  computed as maximum of the Fourier-transformed normalized signal for each modulation frequency is shown in Fig. 4.3(a). The maximum response appears at  $\omega_{\max} \approx 1.5$ , in accordance with the expectation [44, 44] that it should be close to the inverse large-eddy turnover time. In addition, the location of the maximum is not very sensitive to  $R_\lambda$ , reflecting that the response maximum is mainly associated with the large-scale features in the flow. At high modulation frequencies  $\omega > \omega_{\max}$  the decay of  $A_E$  is proportional to  $\omega^{-1}$ , which be-



comes particularly visible in the compensated response  $\omega A_E(\omega)$ , Fig. 4.3(b). At very low modulation frequencies  $\omega < \omega_{\max}$  a plateau in  $A_E(\omega)$  must of course develop [44, 45], as the turbulence then completely follows the forcing. Our simulations do not achieve small enough  $\omega$  to observe a pronounced plateau. The maximum of  $\omega A_E(\omega)$  is about 35% higher as compared to the value at high  $\omega$ . This is as expected lower than predicted by the mean-field theory described in Ref. [44] as the fluctuations slightly smear out the mean-field maximum, but it is much more pronounced compared to results based on the GOY or REWA simulations [45]. The reason is that, although the appearance of the response maxima is a large-scale effect, the correct resolution of the small scales is important for a proper quantitative representation of the effect, because the small-scale resolution affects the energy flux downscale. We also calculated the response curves for the Taylor-Reynolds number; the results are quite similar.

Can such a dependence on the type of forcing also be observed in our numerical simulations? To find out we force a higher wave-number band of modes ( $k_F \leq 5\pi/L_b$ ) instead of restricting us entirely to low wave-number forcing. The result is seen in Fig. 4.3(b) indicated by ( $\diamond$ ). Indeed, for this type of forcing the response maximum is seen to shift to higher  $\omega$  and becomes less pronounced. Further quantitative connections with physical experiments such as the influence of anisotropy [96] are currently being investigated.

The phase difference between the forcing modulation and the conditionally averaged total energy response is shown in Fig. 4.3(a) as inset. We observe a strong variation in this phase difference for modulation frequencies near the most responsive modulation frequency. It appears that the maximum response as shown in Figs. 4.3(a) and (b) occurs at a modulation frequency where also the variation in the phase difference is largest. Very recently, a strong phase shift was also found in windtunnel experiments in which a time-modulation is introduced via a periodic cycling of an upstream active grid. In these experiments the maximum response was found to shift to higher frequencies in case the characteristic length scales of the forcing were reduced [97].

The energy-dissipation rate in the system is a quantity that is accessible to direct physical experimentation. In Figs. 4.3(c) and (d) we show the energy-

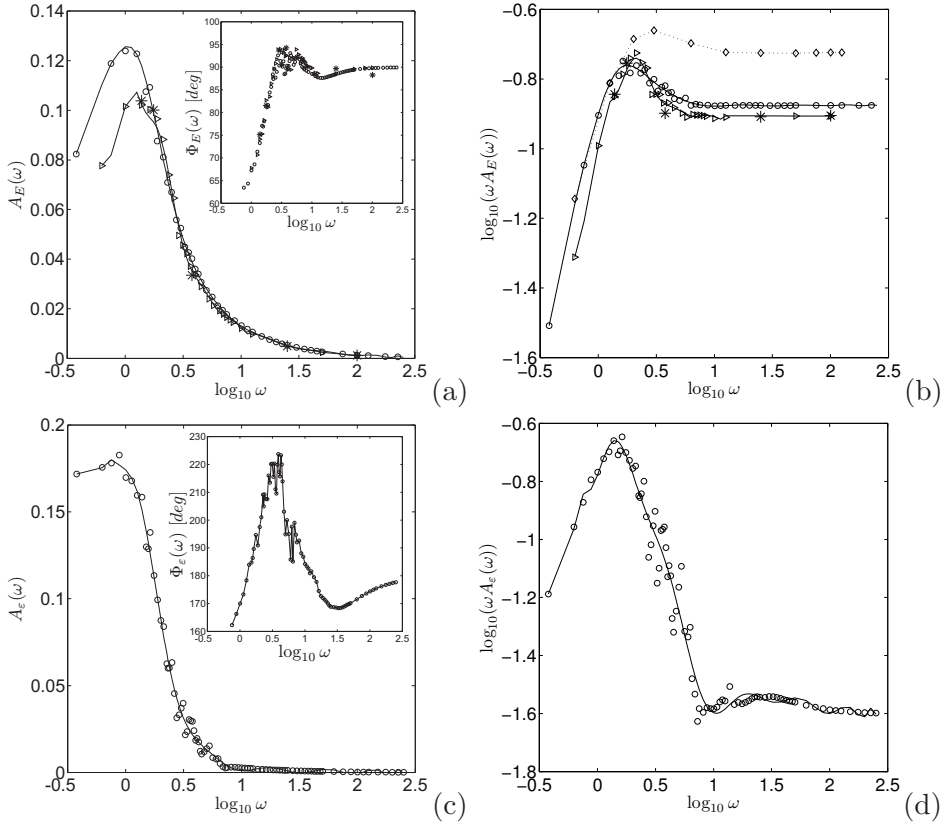


**Fig. 4.3:** Amplitudes:  $A_E(\omega)$  (a),  $A_\varepsilon(\omega)$  (c) and compensated amplitudes:  $\omega A_E(\omega)$  (b),  $\omega A_\varepsilon(\omega)$  (d) for the energy and energy-dissipation rate obtained for  $R_{50}$  (labeled  $\circ$ ) and  $R_{100}$  (labeled  $\triangleright$ ) cases. Verification at selected frequencies for resolution  $128^3$  and  $R_{100}$  case (labeled  $\star$ ). Results for  $R_{50}$  case forced in two first shells (labeled  $\diamond$ ). The insets show the phase-shift between the energy  $\Phi_E(\omega)$  (a) and energy-dissipation rate responses  $\Phi_\varepsilon(\omega)$  (b), and the forcing modulation.

dissipation rate amplitudes  $A_\varepsilon(\omega)$ ,  $\omega A_\varepsilon(\omega)$ . We notice that at high modulation frequency  $\omega$  the amplitude approaches zero, consistent with the expectation that the modulation of the forcing is not effective in this range. More importantly, the energy-dissipation rate amplitude displays a strong response maximum at the level of 85% compared to the amplitude of mod-

ulation. The total mean energy dissipation  $T^{-1} \int_0^T \varepsilon(\omega, t) dt$  for each modulation frequency  $\omega$  is almost constant. It differs from the energy-input rate  $\varepsilon_w = 0.15$  at the level of 1% for most of the frequencies, reaching the maximum difference of 5% for the lowest simulated frequency, confirming good numerical convergence. This is in agreement with boundary layer experiments [96] where the *time-averaged* quantities are only slightly affected by the imposed oscillations.

## 4.5 Conclusions

The direct numerical simulation of the response of turbulence to time-modulated forcing confirms the existence of a response maximum. The simulation findings are in general agreement with predictions based on a mean-field theory [44]. The mean-field theory predicts the decrease of the response amplitude proportional to  $\omega^{-1}$  as the modulation frequency is sufficiently large that was observed in the simulations as well. The response maxima in the total energy and the Taylor-Reynolds number occur at the forcing frequencies of the order of the inverse large-eddy turnover time scale. The phase difference between the modulation of the forcing and the conditionally averaged response displays a strong dependence on the modulation frequency as well. The modulation frequency at which the response maximum arises depends only weakly on the Reynolds number but shows a dependence on the scales included in the forcing as well as on the flow property that is considered. In general, if the particular quantity of interest shows a stronger dependence on the smaller scales in a turbulent flow, then the response maximum arises at a somewhat higher frequency. These findings may be independently assessed in physical experiments, e.g., conducted in wind tunnels combined with the use of active grids cycled in a periodic sequence [97].

## Acknowledgments

Stimulating discussions with Willem van de Water (Eindhoven University of Technology) are gratefully acknowledged. This work is sponsored by the Foundation for Fundamental Research on Matter (FOM). The authors wish to thank SARA Computing and Networking Services for providing the computational resources.



# Turbulence modification by time-periodic forcing<sup>†</sup>

The response of turbulent flow to time-modulated forcing is studied by direct numerical simulation of the Navier–Stokes equations. The forcing is modulated via periodic energy-input variations at a frequency  $\omega$ . Harmonically modulated forcing of the large scales is shown to yield a response maximum at frequencies in the range of the inverse of the large-eddy turnover time, as well as a characteristic rapid change of the phase-angle between forcing and response. Harmonically modulated broadband forcing is also studied in case a wide spectrum of length scales is forced simultaneously. If smaller length-scales are also explicitly agitated by the forcing, the response maximum is found to occur at higher frequencies and to become less pronounced. In case the explicitly forced spectrum is sufficiently wide, a response maximum was not observed. At high modulation frequencies the amplitude of the kinetic energy response decreases as  $1/\omega$ , consistent with theoretical predictions. The amplitude response to intense pulses of energy injected via a square-wave modulated forcing at the largest scales was also studied. This forcing protocol induces a more complicated response structure that also displays a maximum in the kinetic energy amplitude response at a modulation frequency comparable to the harmonically modulated case.

---

<sup>†</sup>“*Turbulence modification by periodically modulated scale-dependent forcing*” by A. K. Kuczaj, B. J. Geurts, D. Lohse, and W. van de Water submitted to a special issue of *Computers & Fluids* associated with Conference on Turbulence and Interactions (TI2006) held in Porquerolles, France, May 29 - June 2, 2006 [62].

## 5.1 Introduction

Forcing of turbulent flow has been applied since many years in computational models, primarily aimed at studying basic problems of turbulence dynamics such as properties of inertial range scales, universality and intermittency [86, 8]. However, variations and modulations of the type of forcing rarely been taken into account in modeling of turbulent flows that are of more direct interest to industrial applications. Examples in which part of the flow modeling may involve explicit forcing of a range of length scales simultaneously are flow through a complex three-dimensional metal foam to understand heat-transfer [11] or flow through fractal gaskets to investigate mixing enhancement [55]. These problems involve more elaborate forcing protocols. It is the purpose of this paper to investigate the consequences of flow agitation, with particular emphasis put on time-modulation and broadband forcing.

Recently, turbulence driven by a time-periodic, i.e., harmonic energy-input rate was theoretically analyzed [44, 45] and resonance maxima were predicted, based on mean-field theory and simulations involving the Gledzer-Ohkitani-Yamada (GOY) model [4] and the reduced wave vector approximation (REWA) [40]. This resonance phenomenon was confirmed by direct numerical simulations of the full Navier–Stokes equations [61].

On the experimental side, recent work concerning a time-periodic energy-injection rate to a fluid in the von Kármán swirl geometry [98], or, concerning flows that are periodically driven by two counter-rotating stirrers [15], provides evidence that modulation in time of the external forcing can lead to different degrees of turbulence responsiveness. The magnitude of the response depends on the modulation frequency and can develop maxima that may be relevant to technological processes, e.g., to control mixing efficiency. Also windtunnel experiments [97] suggest a striking frequency dependency of the responsiveness of the flow that appears connected directly to the structure of turbulence. In these windtunnel experiments the modulation of the forcing was introduced via an active grid placed upstream of the measuring section. This active grid was cycled in a particular periodic sequence that was repeated with frequency  $\omega$ . Several aspects of the response of the turbulent flow, such as the frequency dependence, were found to rely on the particular sequence traversed by the active grid. This additional sensitivity

to the spatial structure of the forcing represents a further complexity that may be represented by introducing time-modulation to forcing in which a range of flow scales is agitated simultaneously. This brings about an interest in time-modulation of broadband forcing, which is central to this paper.

These experiments further motivate the extension of existing large-scale forcing strategies to also describe turbulent flows under the influence of periodically driven forces. In this paper we report direct numerical simulations of turbulent flow under the influence of periodically modulated forcing and investigate the changes that occur in the location and magnitude of the response maxima when forcing-specific parameters are varied. Specifically, the emphasis is placed on *(i)* multiscale perturbation of a flow, investigating effects due to the spectral support of the forcing, *(ii)* the influence of the modulation amplitude on the response and *(iii)* the robustness of the response to variations in the forcing protocols.

We found that harmonically modulated forcing of the large scales yields a response maximum at frequencies in the range of the inverse of the large-eddy turnover time. Consistent with theoretical predictions, at high modulation frequencies the amplitude of the kinetic energy response decreases as  $1/\omega$ . Near the maximal response a rapid change of the phase-angle between forcing and response was observed. Explicit agitation of smaller length scales causes that the response maximum shifts to higher frequencies and becomes less pronounced. In case of sufficiently wide explicitly forced spectrum, a response maximum was not observed. We also studied the amplitude response to intense pulses of energy injected via a square-wave modulated forcing at the largest scales. This forcing protocol induces a more complicated response structure that also yields a maximum amplitude response.

The organization of this paper is as follows. In Sec. 5.2 we briefly present the computational flow model. The results are described and analyzed in Sec. 5.3, discussing harmonically modulated large-scale forcing (see also Ref. [61]) and small-scale forcing as well as the effect of square-wave modulation. The conclusions are given in Sec. 5.4.

## 5.2 Computational flow model

The incompressible Navier–Stokes equations are solved numerically in a periodic flow domain with a pseudo-spectral code [60]. We consider

$$\left(\partial_t + \nu k^2\right)u_\alpha(\mathbf{k}, t) = \Psi_\alpha(\mathbf{k}, t) + F_\alpha(\mathbf{k}, t), \quad (5.1)$$

with kinematic viscosity  $\nu = \text{Re}^{-1}$ , in terms of the Reynolds number  $\text{Re}$ , and  $u_\alpha(\mathbf{k}, t)$  the Fourier coefficient of the velocity field in the  $x_\alpha$ -direction, at wave vector  $\mathbf{k}$  ( $k = |\mathbf{k}|$ ) and time  $t$ . The nonlinear term  $\Psi_\alpha$  incorporates the incompressibility constraint [71]. Finally,  $F_\alpha$  represents the forcing.

The agitation of the flow is achieved by introducing an explicit forcing  $F_\alpha(\mathbf{k}, t)$ . The specification of the forcing proceeds in two steps, first addressing the basic wave number dependent forcing  $f_\alpha$  and then describing its temporal modulation to arrive at  $F_\alpha$ .

The basic forcing  $f_\alpha$  is defined with reference to all modes in the band  $\mathbb{K}_{m,p}$  ( $m \leq p$ ), which consists of  $p - m + 1$  adjacent spherical shells  $\mathbb{S}_n = \frac{2\pi}{L_b}(n - 1/2) < |\mathbf{k}| \leq \frac{2\pi}{L_b}(n + 1/2)$ :  $m \leq n \leq p$ . Here,  $L_b$  is the box-size in physical space. The basic forcing  $f_\alpha(\mathbf{k}, t)$  [60] is given for all  $n \in [m, p]$  by

$$f_\alpha(\mathbf{k}, t) = \left(\frac{\varepsilon_w}{M}\right) \frac{a_n}{P_n} \frac{u_\alpha(\mathbf{k}, t)}{|\mathbf{u}(\mathbf{k}, t)|^2} \quad ; \quad \mathbf{k} \in \mathbb{S}_n, \quad (5.2)$$

where  $\varepsilon_w$  is a constant energy-injection rate and  $M \leq p - m + 1$  denotes the number of shells out of  $\mathbb{K}_{m,p}$  that are actually forced. An equal fraction  $\varepsilon_w/M$  of the energy-input rate is allocated to each of the forced shells. The number of modes in  $\mathbb{S}_n$  is denoted by  $P_n$  and  $a_n = 1$  in case the modes in  $\mathbb{S}_n$  are forced explicitly and 0 otherwise. Hence, the energy-input rate to each of the modes in the same forced band  $\mathbb{S}_n$  is identical.

In this paper we will consider forcing in the band  $\mathbb{K}_{1,16}$  and distinguish three cases:

- (A) large-scale forcing only ( $M = 1$ ;  $a_n = 0$  except  $a_1 = 1$ ),
- (B) two-shell forcing ( $M = 2$ ;  $a_n = 0$  except  $a_1 = a_2 = 1$ ),
- (C) five-shell forcing ( $M = 5$ ;  $a_n = 0$  except  $a_1 = a_2 = a_4 = a_8 = a_{16} = 1$ ).



The number of modes in the forced shells is given by  $P_1 = 18$ ,  $P_2 = 62$ ,  $P_4 = 210$ ,  $P_8 = 762$  and  $P_{16} = 3338$  respectively.

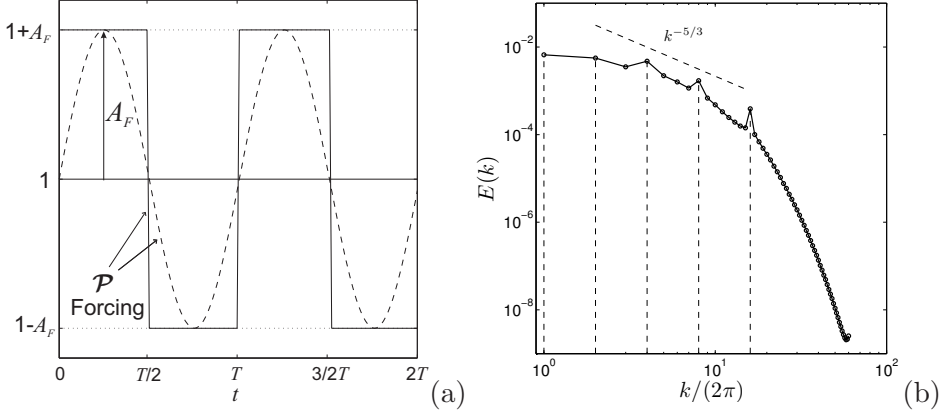


**Fig. 5.1:** (a) Sinusoidal (dashed) and square-wave (solid) forcing protocols  $\mathcal{P}$  with amplitude  $A_F$ . (b) Time-averaged energy spectrum with discrete unmodulated forcing in five shells referred to as the broadband forcing case (C) within the  $\mathbb{K}_{1,16}$  band.

The second step in specifying the forcing  $F_\alpha(\mathbf{k}, t)$  introduces periodic modulation through

$$F_\alpha(\mathbf{k}, t) = \mathcal{P}(\omega t) f_\alpha(\mathbf{k}, t) = \left(1 + A_F s(\omega t)\right) f_\alpha(\mathbf{k}, t), \quad (5.3)$$

where  $A_F$  is the amplitude of the forcing protocol  $\mathcal{P}$ ,  $\omega$  the angular frequency and  $s(\omega t)$  the modulation, which is such that  $s(z + 2\pi) = s(z)$ . We will consider two types of modulation, i.e., the sinusoidal wave:  $s(\omega t) = \sin(\omega t)$  and the square-wave consisting of square pulses:  $s(\omega t) = \text{sgn}(\sin(\omega t))$ . The modulated forcing corresponds to a total energy-input rate, which oscillates around  $\varepsilon_w$  with amplitude  $A_F$ ,

$$T_F(\omega, t) = \sum_{\mathbf{k}} u_\alpha^*(\mathbf{k}, t) F_\alpha(\mathbf{k}, t) = \varepsilon_w \left(1 + A_F s(\omega t)\right), \quad (5.4)$$

where  $(^*)$  denotes complex conjugate. The forcing protocols are schematically presented in Fig. 5.1(a).

In the sequel, the response of the turbulent flow to the class of explicit forcing protocols [Eqs. (5.2) and 5.3] will be investigated. We focus on

dependencies of turbulence properties on the modulation frequency  $\omega$ , the amplitude  $A_F$ , the specific protocol  $s$ , and the spectral support of the forcing (i.e., case (A), (B) or (C)). Particular attention will be given to the kinetic energy and the energy-dissipation rate will be discussed in some detail in the next section.

## 5.3 Periodic modulation

In this section we first describe the flow when subjected to harmonically modulated forcing and discuss in some detail the method of data processing (5.3.1). Then, in separate subsections we will address the effect of variations in forcing amplitude (5.3.2), the influence of variations in the spectral support of the forcing (5.3.3) and the consequences of changes in the forcing protocol (5.3.4).

### 5.3.1 Harmonically modulated forcing

In order to characterize the response to harmonically modulated forcing we adopt, as point of reference, forced turbulence without time-modulation. The computational box-size is taken as  $L_b = 1$  and we use a Reynolds number  $\text{Re} = 1061$  as also adopted in Ref. [77, 60].

The energy-injection rate  $\varepsilon_w = 0.15$  in cases (A) and (B) while  $\varepsilon_w = 0.45$  was used in case (C). These energy-injection rates were selected to obtain approximately comparable Taylor-Reynolds numbers, fluctuating all roughly in the range 30–50 in each simulation. In order to measure the amplitude of the response, numerical simulations in the frequency range  $\pi/5 \leq \omega \leq 80\pi$  were performed with time-modulated forcing at amplitudes  $A_F = 1/5, 1/2, \text{ and } 1$ . As an illustration, the time-averaged kinetic energy spectrum obtained in the five-shell forced case (C) is displayed in Fig. 5.1(b). A general compliance with the well-known  $-5/3$  scaling may be observed, next to characteristic localized peaks in the spectrum, associated with the forced modes. We verified that using a resolution of  $64^3$  provides ample resolution of the small scales in this flow. Throughout this paper simulations are such that for the most computationally demanding modulation amplitudes and frequencies the  $k_{\max}\eta$  criterion does decrease below 1.4 level.

To extract the relevant average quantities from the simulations, an ensemble of  $N_r = 30$  statistically independent initial conditions, taken from the unmodulated forced turbulence, and each separated by two eddy-turnover times, was used. This ensemble of simulations was adopted to extract the conditionally averaged signal at each forcing frequency. Simulations for each frequency, and initial condition, were performed over a time extent of four forcing periods  $T = 2\pi/\omega$  with 320 monitoring points, i.e., 80 for each period). Data were collected over the latter two forcing periods to average the results over time and over realizations. The robustness of this procedure was discussed in Ref. [61] in which also the number of 30 independent realizations and the level of statistical convergence were further scrutinized.

To quantify the response of the total kinetic energy to time-modulated forcing, we adopt the following procedure [61]. First, corresponding to a modulation frequency  $\omega$  and the  $j$ th initial condition out of the  $N_r$  realizations, we record the kinetic energy  $E_j(\omega, t)$  and its time average  $\overline{E}_j(\omega)$ . Second, we build the normalized kinetic energy  $Q_E(\omega, t) = \langle E_j(\omega, t) / \overline{E}_j(\omega) \rangle_{N_r}$  where  $\langle \cdot \rangle_{N_r}$  denotes averaging over the  $N_r$  realizations taken from the ensemble. Third, the Fourier transform ( $\mathcal{F}$ ), in which time  $t$  is transformed into frequency  $f$ , is applied yielding a power amplitude spectrum  $\widehat{Q}_E(\omega, f) = \mathcal{F}(Q_E(\omega, t) - 1)$ . Of particular importance to quantifying the response maxima to time-modulated forcing are the maximum value  $A_E(\omega)$  and phase-shift  $\Phi_E(\omega)$  defined as:

$$A_E(\omega) = \max_f \{ |\widehat{Q}_E(\omega, f)| \} \equiv |\widehat{Q}_E(\omega, f_E(\omega))|, \quad (5.5)$$

$$\Phi_E(\omega) = \arctan \left( \frac{\text{Im}(\widehat{Q}_E(\omega, f_E(\omega)))}{\text{Re}(\widehat{Q}_E(\omega, f_E(\omega)))} \right). \quad (5.6)$$

Here, we introduced  $f_E(\omega)$  as the frequency at which  $|\widehat{Q}_E(\omega, f)|$  attains its maximum. A similar procedure is also applied to the energy-dissipation rate  $\varepsilon(\omega, t)$  yielding  $A_\varepsilon(\omega)$  and  $\Phi_\varepsilon(\omega)$ .

In Fig. 5.2 (see also Ref. [61]) the normalized energy  $Q_E(\omega, t)$  and energy-dissipation rate  $Q_\varepsilon(\omega, t)$  are plotted for four different modulation frequencies  $\omega$ . For lower frequencies the energy response is able to adjust instantaneously to the modulation of the forcing. We observe small phase-shift between the response and modulation. For higher frequencies the amplitudes of the responses strongly decrease and the phase-shift with respect

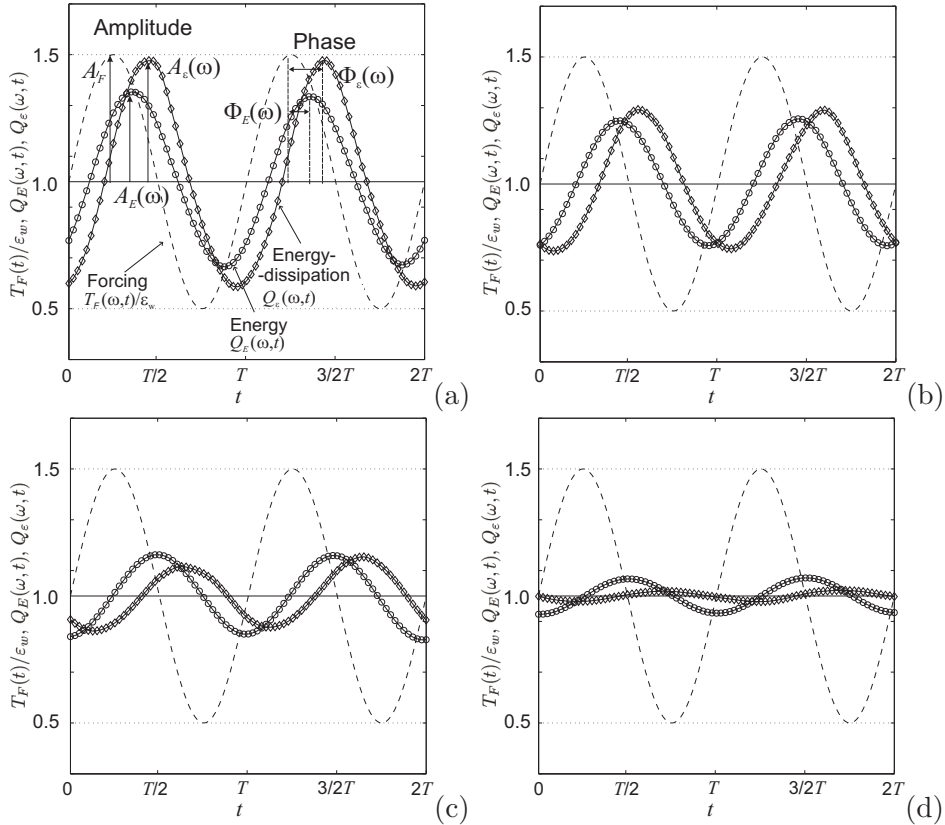


**Fig. 5.2:** The normalized energy  $Q_E(\omega, t)$  ( $\circ$ ), and the energy-dissipation rate  $Q_\varepsilon(\omega, t)$  ( $\diamond$ ) obtained from the large-scale forcing of type (A) with amplitude  $A_F = 1/2$  at modulation frequency  $\omega = 0.32\pi$  (a),  $\omega = 0.56\pi$  (b),  $\omega = 0.80\pi$  (c),  $\omega = 1.60\pi$  (d). In (a) we also illustrated the amplitudes  $A_E(\omega)$ ,  $A_\varepsilon(\omega)$  and phase-shifts  $\Phi_E(\omega)$ ,  $\Phi_\varepsilon(\omega)$  relative to the forcing (dashed).

to the modulation becomes more pronounced. The response in the energy-dissipation rate is larger for low frequencies than the response in the total kinetic energy. The situation changes for higher modulation frequencies. This behavior may be related to the amount of energy remaining in the system for various forcing modulations. For high frequencies turbulence does not detect the modulation, hence smaller portions of energy but larger amount of them in the same time-frame travel to small scales where the

dissipation plays a primary role. Further energy transfer investigations are needed in order to explain this characteristic behavior. These can be performed in similar fashion as in Ref. [75], when the induced pulses of energy at the largest scales were tracked in time as they pass various length scales in a similar way as Lagrangian particles.

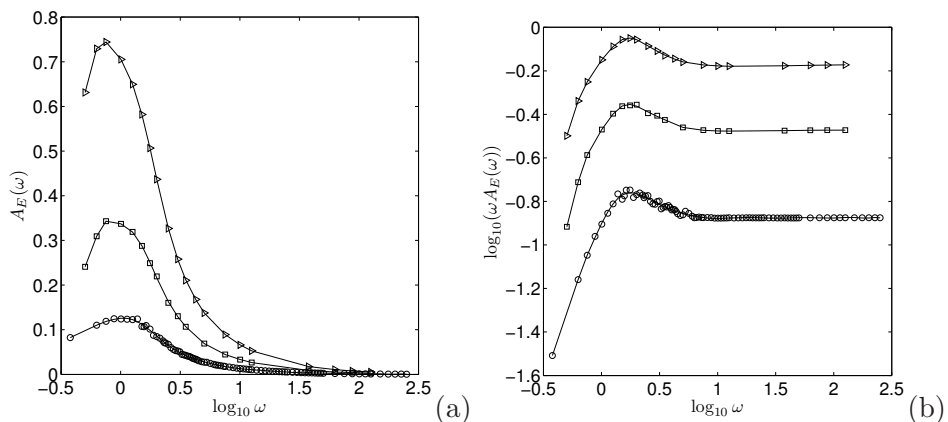


**Fig. 5.3:** Total kinetic energy amplitude response  $A_E(\omega)$  (a) and compensated total kinetic energy amplitude response  $\omega A_E(\omega)$  (b) for the large-scale forcing of type (A) at three different amplitudes:  $A_F = 1/5$  ( $\circ$ ),  $A_F = 1/2$  ( $\square$ ),  $A_F = 1$  ( $\triangle$ ).

Moreover, the relatively large amplitude of forcing ( $A_F \geq 1/2$ ) causes the asymmetry in the amplitude response, because with the growing amplitude of forcing turbulence almost exhibits a free decay period during the negative phase of the modulation. This will be directly seen in subsection 5.3.4, where we analyze the results of the flow modulation by the square-wave pulses of injected energy.

### 5.3.2 Variation of the modulation amplitude

The influence of variations in the amplitude  $A_F$  of the forcing-modulation on the responsiveness of turbulent flow is discussed next. We turn to turbulent flow that is forced at the largest scales only, i.e., adopt type (A) modulation. The direct numerical simulation of time-modulated large-scale

forcing confirms the existence of a response maximum at frequencies quite close to the inverse of the large-eddy turnover time. This is illustrated in Fig. 5.3 where we collected the amplitude response of the kinetic energy  $A_E(\omega)$  obtained at different modulation strengths. The maximum in the amplitude responses in Figs. 5.3(a) and (b) is observed at  $\omega \approx 1$  where we remark that the non-dimensionalization is such that the unit of time corresponds to one large-eddy turnover time. We studied three amplitudes of forcing  $A_F = 1/5, 1/2, 1$ . In each of these cases, quite similar behavior of the response can be observed. The maximal response is more pronounced for the larger amplitude of forcing. At large modulation frequencies  $\omega$ , we observe a decrease in the responsiveness, which indicates that the turbulence can not respond to fast modulation frequencies. At high modulation frequencies the decay of  $A_E(\omega)$  is seen to be proportional to  $1/\omega$ , as predicted by the mean-field theory presented in Ref. [44].

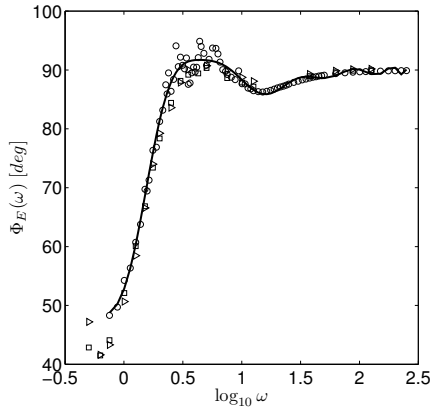


**Fig. 5.4:** Phase-shift between the energy  $\Phi_E(\omega)$  and the forcing modulations for the large-scale forcing (A) at three different modulation amplitudes:  $A_F = 1/5$  ( $\circ$ ),  $A_F = 1/2$  ( $\square$ ),  $A_F = 1$  ( $\triangle$ ).

The phase difference between the forcing modulation and the conditionally averaged total energy response is shown in Fig. 5.4. At low modulation frequencies the phase difference is zero, indicating that the modulations are instantaneously followed by the turbulent flow. We observe a strong variation near the modulation frequency at which the flow is most responsive. We notice that the amplitude  $A_F$  of the forcing-modulation has no

strong influence on the phase difference. At high modulation frequencies the phase-difference approaches  $90^\circ$ .

In Fig. 5.5(a) we show the effect of variations in the amplitude  $A_F$  of the forcing-modulation on the compensated energy-dissipation rate amplitude  $\omega A_\varepsilon(\omega)$ . This quantity is accessible to direct physical experimentation. We notice that at high modulation frequency  $\omega$  the amplitude approaches zero, consistent with the expectation that the modulation of the forcing is not effective in this range. More importantly, the energy-dissipation rate amplitude displays a strong response maximum at roughly the same modulation frequency as observed for the kinetic energy response. The effect of variations in  $A_F$  on the phase difference  $\Phi_\varepsilon(\omega)$  may be observed in Fig. 5.5(b). We notice that the phase difference approaches  $180^\circ$  at high  $\omega$ , which is twice the value observed for the kinetic energy.

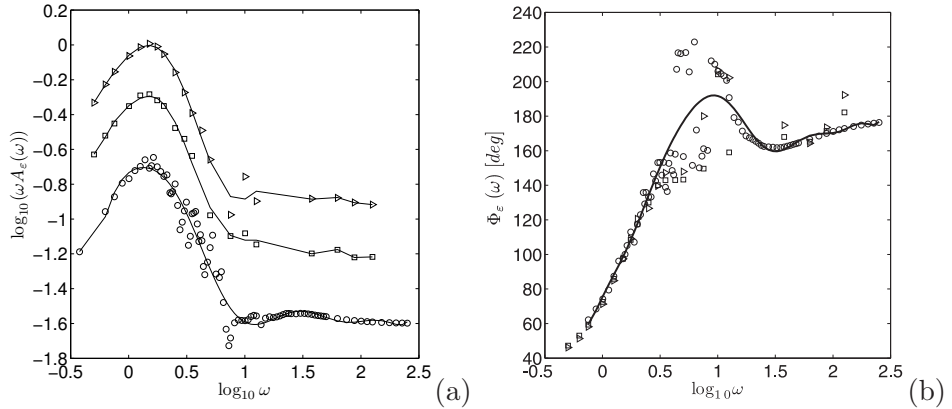


**Fig. 5.5:** Response of compensated energy-dissipation rate amplitude  $\omega A_\varepsilon(\omega)$  (a) and phase-shift between the energy-dissipation rate  $\Phi_\varepsilon(\omega)$  and the forcing modulations (b) for the large-scale forcing (A) at three different modulation amplitudes:  $A_F = 1/5$  ( $\circ$ ),  $A_F = 1/2$  ( $\square$ ),  $A_F = 1$  ( $\triangle$ ).

### 5.3.3 Variation of the range of forced scales

Apart from the amplitude of the forcing modulation, the spectral support of this modulation has a strong effect on the response of the turbulent flow. We now consider this in more detail. We compare the results of

type (A) and (B) forcing to the behavior seen in the five-shell broadband-forced turbulence obtained with type (C) forcing. This effect may be seen in Figs. 5.6(a) and (b) where the total kinetic energy response for the three simulated forcing cases (A), (B) and (C) is shown. The turbulence response changes compared to the large-scale forcing results (type (A)) if we also incorporate forcing of some smaller scales in the second shell (type (B)). In case (B) the maximum response in the compensated energy amplitude is still clearly visible but it has become less pronounced. Moreover, the maximal response is now observed at higher frequencies near  $\omega \approx 3.2$ .

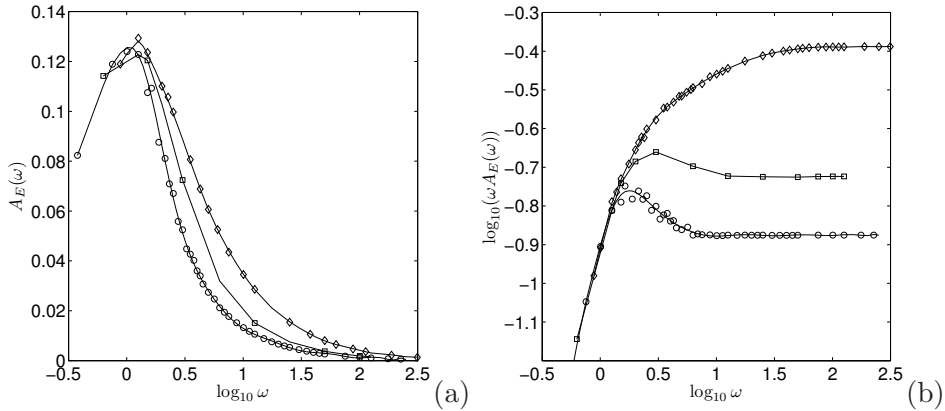


**Fig. 5.6:** Total kinetic energy amplitude response  $A_E(\omega)$  (a) and its compensated value  $\omega A_E(\omega)$  (b) for the large-scale forcing (A:  $\circ$ ), two-shell forcing (B:  $\square$ ) and five-shell forcing (C:  $\diamond$ ).

The agitation of a larger number of small scales at the same total energy-input rate  $\varepsilon_w$  appears to wash out a response maximum. Generally, the forcing of these smaller scales leads to a more rapid decorrelation of the large scales, which evidently diminishes the responsiveness of the turbulence to external agitation. This effect is further pronounced in the broadband-forced case (C) for which a characteristic response maximum can no longer be discerned. Similar conclusions can be drawn for the energy-dissipation rate. Further analysis of the dependence of the velocity correlation-time



on the modulation frequency in the three cases (A), (B) and (C) will be conducted to quantify these effects. This addresses aspects of the physical-space effects of modulated forcing and will be published elsewhere.

### 5.3.4 Variation of the periodic forcing protocol

The dependence of the turbulence response on the specific shape of the modulation protocol  $s(\omega t)$  will be considered next. For that purpose we investigate forcing that is modulated by a square-wave forcing protocol, periodically kicked turbulence [66, 49]. The square-wave forcing induces a much more complicated response structure in comparison to the sinusoidal forcing modulation used so far. However, several global properties of the turbulence responsiveness were found to be quite insensitive to the forcing protocol.

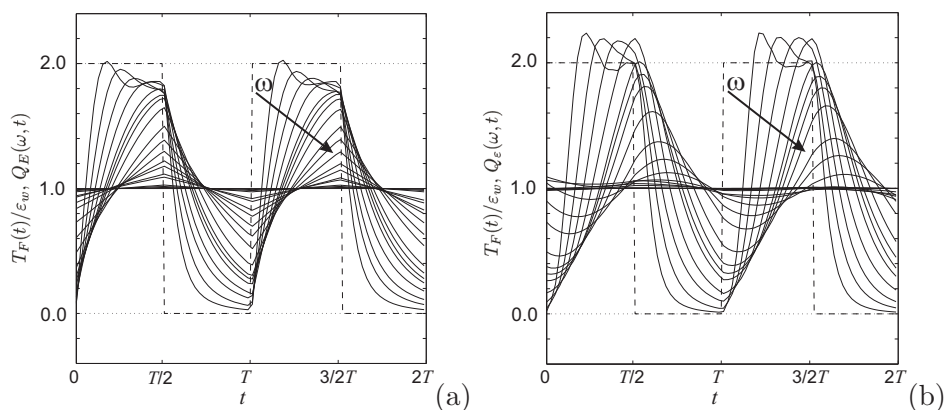


**Fig. 5.7:** Kinetic energy (a) and energy-dissipation rate (b) amplitude response of turbulence to square-wave large-scale forcing of type (A) simulations with amplitude  $A_F = 1$  for various modulation frequencies in the range  $\omega/(2\pi) = 0.16 - 40$ . The arrow denotes the direction of increasing frequency of modulation.

In Fig. 5.7 we plotted the kinetic energy and energy-dissipation rate response for various frequencies of the square-wave forcing modulation. An increase in the modulation frequency is marked by an arrow. The application of the square-wave forcing at an amplitude  $A_F = 1$  causes an energy-injection during half the period, and no forcing during the second half. During this second stage, turbulence freely decays. At low frequencies

$\omega$  the pulsed injection of energy causes an overshoot in the response. Afterwards the turbulence stays approximately in a quasi-stationary state until the end of the energy-injection period, when an abrupt cutoff of energy supply leads to its free decay. The overall amplitude response of the kinetic energy and energy-dissipation rate decreases with increasing frequency. We also observe a stronger and less abrupt response in the energy-dissipation rate compared to the response in the kinetic energy particularly at high  $\omega$ .

Before turning to the frequency-dependence of the amplitude response, we first assess the sensitivity of the results on the averaging procedure. For this purpose we started with two sets of simulations. In the first case, the amplitude of the forcing was positive  $A_F = 1$ , while in the second we reversed the situation applying a negative amplitude  $A_F = -1$  initially. This means that we start either with a sharp pulse of energy-injection or with its free decay. The same set of simulations was performed during four periods of modulation and data were also averaged over 30 independent realizations. If we neglect the first period and shift the response data in the time domain by half the period  $T$ , the differences are negligible. This can be seen in Fig. 5.8, where we plotted the kinetic energy and the energy-dissipation rate amplitude responses for selected frequencies. The kinetic energy ( $\circ, \square$ ) and energy-dissipation rate ( $\diamond, \triangle$ ) responses are almost indistinguishable for these two cases. This further supports the correctness of the averaging procedure employed.

The frequency dependence of the response in the kinetic energy and the energy-dissipation rate, following from a square-wave modulation protocol, are shown in Fig. 5.9. Here, we restrict the analysis of the response to the lowest dominant Fourier coefficient in the response signal. We observe a characteristic response maximum in the compensated energy response plot, Fig. 5.9. Similar as for the sinusoidal forcing-modulation a phase-shift arises between the forcing and the maximal energy and energy-dissipation rate responses. The phase-shift goes to  $90^\circ$  for the energy response and to  $180^\circ$  for the energy-dissipation rate response and varies rapidly at the frequency where the maximal responses exist.

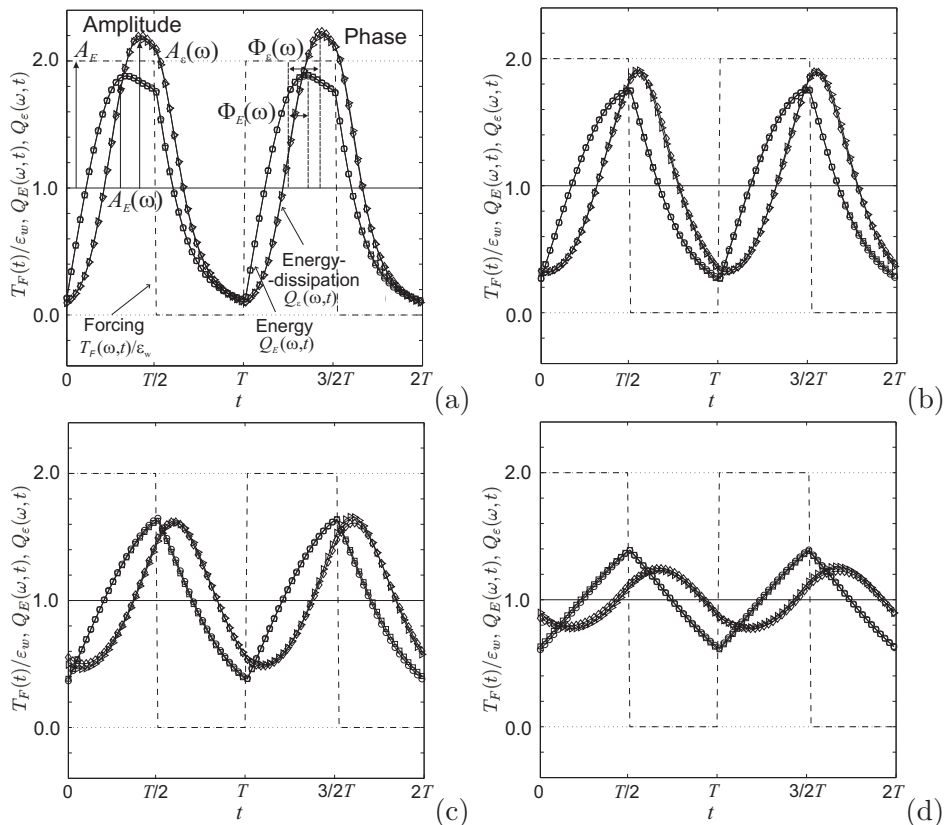


**Fig. 5.8:** The normalized energy  $Q_E(\omega, t)$  ( $\circ$ ,  $\square$ ), and the energy-dissipation rate  $Q_\varepsilon(\omega, t)$  ( $\diamond$ ,  $\triangle$ ) obtained from the square-wave large-scale forcing of type (A) simulations with amplitude  $A_F = 1$  at modulation frequency  $\omega = 0.32\pi$  (a),  $\omega = 0.52\pi$  (b),  $\omega = 0.64\pi$  (c),  $\omega = 0.96\pi$  (d). The amplitudes  $A_E(\omega)$ ,  $A_\varepsilon(\omega)$  and phase-shifts  $\Phi_E(\omega)$ ,  $\Phi_\varepsilon(\omega)$  of the forcing (dashed) are shown. The results for an initial kick ( $\circ, \diamond$ ) are indistinguishable from those started with an initial decay and shifted by half the period  $T$  ( $\square, \triangle$ ).

## 5.4 Conclusions

In this paper we examined turbulence driven by a periodically modulated forcing. We concentrated on the effects of varying the intensity of forcing, the spectral support of the explicitly agitated scales and the forcing proto-

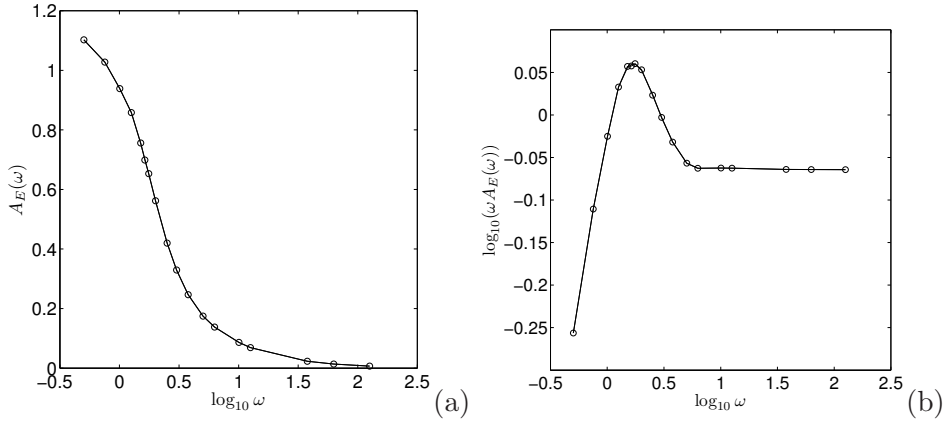


**Fig. 5.9:** Total kinetic energy amplitude response  $A_E(\omega)$  (a) and its compensated value  $\omega A_E(\omega)$  (b) for the large-scale forcing (A) with the square-wave modulation protocol.

col. The amplitude response was observed for the kinetic energy and the energy-dissipation rate. The simulations confirm the existence of a characteristic time-scale in turbulent flow, at which the amplitude response has a maximum. This time-scale is connected to the larger scales in the flow and is on the order of the eddy-turnover time.

The response to pulses of energy injected with a square-wave forcing-protocol was also determined. This problem was considered earlier in Ref. [75] where it was shown that an initial pulse of kinetic energy injected at the large scales of the flow propagates in time to the smaller scales as if it were a fluid particle. It was found also that pulses of energy at the largest scales correlate on average better with pulses at smaller scales only after allowing the cascade to proceed for some time. The results in Ref. [75] were limited to qualitative observations due to the large statistical fluctuations in the data. These qualitative findings could be confirmed in our simulations, where we observe a maximal response of the turbulence at a characteristic time of the order of the eddy-turnover time. In our simulations the statistical fluctuations in the data could be removed by the application of ensemble averaging over a large number of independent realizations.

---

Future analysis of the energy transfer through the scales present in the flow will be performed. This may directly measure the characteristic cascading time associated with the travel of energy down the cascade. Another aspect worthwhile to consider in future work is the possible existence of structures at various scales of motions. This allows addressing the question of possible resonances connected with the presence of specific structures perturbed explicitly in the flow.

## Acknowledgments

AKK and BJB thank Ye Zhou (Lawrence Livermore National Laboratory) for his kind suggestions and remarks. This work is part of the Turbulence Research Program of the Foundation for Fundamental Research of Matter (FOM). Computations were performed at the SARA Computing and Networking Services in Amsterdam through grant SC-213 of the Dutch National Computing Foundation (NCF).



# Chapter 6

## Concluding remarks and outlook

**General context.** The basic aim of this thesis was to numerically investigate the way in which various scales of motion in turbulence interact and how this may be modulated relative to the natural cascading process, through explicit external forcing. One way to observe these interactions is to disturb the processes that govern them, i.e., to influence the energy transfer between the largest and the smallest scales in a flow. We approached this goal by studying the response of turbulence to forcing that is applied not only at the classically studied largest scales, but also at a range of smaller inertial scales. This allows investigating the energy dynamics in broadband-forced turbulence. The application of broadband forcing was shown to yield *controlled non-Kolmogorov turbulence* that displays a strong modification of the energy spectra. Similar situations can be observed in many flows in nature. They do not obey the classical Kolmogorov picture of turbulence because of interactions with complex boundaries. Perturbation of the classical picture of the Kolmogorov cascade served as the main motivation of this thesis. Another motivation was to explore periodically forced flows in the context of large-scale and broadband forcing. Such periodic forcing plays a primary role in the atmosphere and oceans due to the Earth's rotation, heating by the Sun or gravitation of the Moon. The atmosphere and the upper layer of oceans are highly turbulent. Hence, periodic forcing is an important issue in turbulence.

**Mixing in manipulated turbulence.** We investigated explicit forcing methods as a modeling framework that incorporates the effect of agitation of small scales caused by geometrically complex objects such as metal foams. We have shown that with a relatively simple forcing model basic properties of complex flows can be captured such as spectral by-pass arising from the simultaneous forcing of a range of scales in a flow. The ultimate goal would be to find the relation between real objects seen in nature, their mathematical representation and the corresponding forcing.

We paid attention to the relevance of spectral space forcing for physical space mixing characteristics. We performed numerical simulations of the dispersion of a passive scalar field in a turbulent flow driven by broadband forcing. We quantified with a level set integration method the mixing efficiency. We found that broadband forcing causes additional production of smaller scales in the flow that are directly responsible for the localized enhancement of the wrinkling of a level set of the passive scalar. In contrast, the surface area of a level set of the tracer is found to be mainly governed by convective sweeping by larger scales in the flow. A direct influence of broadband forcing on the increase of mixing efficiency was found in the cumulative surface area or wrinkling, while the instantaneous effect was found to be maximal in classical Kolmogorov large-scale forced turbulence.

**Energy dynamics in broadband-forced turbulence.** For inertial-range scales deterministic broadband forcing introduces an explicit energy injection term. We varied the spectral support and strength of this forcing to investigate the modulation of the turbulence that develops. We observed an abrupt transfer of energy to smaller scales similar as seen in case of flows through geometrically complicated structures. In such cases, flow that passes a complex obstacle is immediately disturbed at various small scales. We studied in detail the energy dynamics of broadband-forced turbulence. Forcing methods agitating the flow in a wide range of scales induce significant differences in the developing flow. We found that forcing affects the intensity of the developing turbulence by enhancing the nonlocal energy cascade towards smaller scales. This leads to modifications in the energy transfer spectrum and the energy distribution among scales.



**Response maxima in periodically forced turbulence.** We performed simulations in which the strength of large-scale forcing was periodically varied in time. Although such simulations are far from the complexity of real flows seen in nature, the main goal was to verify the existence of response maxima in turbulence. Harmonically modulated forcing of the large scales was shown to yield a response maximum at frequencies in the range of the inverse of the large-eddy turnover time. At high modulation frequencies the amplitude of the kinetic energy response decreases as the inverse of the driving frequency, consistent with theoretical predictions. We also observed a characteristic rapid change of the phase-angle between forcing and response near ‘resonance’.

**Turbulence modification by time-periodic forcing.** We extended the numerical approach used for studying the response of turbulent flow to large-scale, periodically varied forcing. In particular, we allowed such time-varying forcing at various (discrete) scales, varied the amplitudes and the time-periodic protocols. Harmonically modulated broadband forcing, studied in case a wide spectrum of length-scales is simultaneously forced also displays a response maximum. This occurs at higher frequencies and is less pronounced compared to the case of large-scale forcing alone. The maximum is not observed in case the explicitly forced spectrum is sufficiently wide. We also studied the amplitude response to intense pulses of energy injected via a square-wave modulated forcing. This forcing protocol induces a more complicated response structure. A maximum in the kinetic energy amplitude response at a modulation frequency comparable to the harmonically modulated case is also observed in this case.

**Outlook.** Although numerical simulations of most flows seen in nature are computationally not yet feasible, the big advantage of computational fluid dynamics is the ability to extract and separate various phenomena. The presented *broadband-forced turbulence* and *harmonically forced turbulence* are two examples of such studies.

Future development of the broadband forcing strategy should probably concentrate on two areas. Namely, further numerical investigation of the forcing methods with their connections to real-life objects and studies of spatially localized forcing in turbulence. The spatially localized forcing allows

directly to localize perturbations in the region occupied by the actual object. This way forcing can be used as part of the computational modeling. The mechanisms responsible for a spectral shortcut is another important issue worth further numerical investigations.

Various forcing protocols applied in harmonically forced turbulence may directly enhance the turbulence intensity and physical space dispersive transport that is relevant in many technological processes. The examination of the proposed broadband and harmonically modulated turbulence at various Reynolds and Schmidt numbers would be of considerable interest. Most probably the harmonically forced turbulence induces some geometrical flow structuring that can persist for longer time in a specific range of frequencies. These aspects may be directly investigated by looking at the correlation coefficients between various quantities in harmonically forced flows such as energy-input and energy-dissipation rate.

The effect of forcing may be examined by direct splitting of velocity derivatives into vorticity and strain components. This is the basis for the evaluation of so-called geometrical statistics. Preliminary studies in this direction show that broadband forcing influences classical large-scale forced turbulence by diminishing the importance of the self amplification process between vorticity and strain. In turn, this may help to understand the self-amplification mechanism that enhances velocity gradients and plays an important role in the nonlinear dynamics of turbulence. Moreover, these investigations may help to connect the forcing methods with real-life objects.

As a final remark, there is one unifying concept throughout this work regardless what type of forced flow we analyze. The study demonstrated the utility of forcing methods to represent complicated turbulent flows that usually are seen in nature. The content of this dissertation is a computational attempt to shed some more light on the last unsolved problem of classical physics - turbulence.

# Bibliography

- [1] K. Alvelius. Random forcing of three-dimensional homogeneous turbulence. *Phys. Fluids*, 11(7):1880–1889, 1999.
- [2] J. Banhart, M. F. Ashby, and N. A. Fleck. *Cellular metals and metal foaming technology*. Verlag MIT, Bremen, 2001.
- [3] G. K. Batchelor. *Theory of homogeneous turbulence*. Cambridge University Press, 1953.
- [4] L. Biferale. Shell models of energy cascade in turbulence. *Ann. Rev. Fluid Mech.*, 35:441–468, 2003.
- [5] L. Biferale, E. Calzavarini, F. Toschi, and R. Tripiccion. Universality of anisotropic fluctuations from numerical simulations of turbulent flows. *Europhys. Lett.*, 64:461, 2003.
- [6] L. Biferale, M. Cencini, A. S. Lanotte, M. Sbragaglia, and F. Toschi. Anomalous scaling and universality in hydrodynamic systems with power-law forcing. *New J. Phys.*, 6(37):1–16, 2004.
- [7] L. Biferale, A. S. Lanotte, and F. Toschi. Effects of forcing in three-dimensional turbulent flows. *Phys. Rev. Lett.*, 92(9):094503, 2004.
- [8] L. Biferale and I. Procaccia. Anisotropy in turbulent flows and in turbulent transport. *Phys. Rep.*, 414:43–164, 2005.

- 
- [9] G. Boffetta, A. Celani, and M. Vergassola. Inverse energy cascade in two-dimensional turbulence: deviations from Gaussian behavior. *Phys. Rev. E*, 61(1):R29–R32, 2000.
- [10] T. Bohr, M. H. Jensen, G. Paladin, and A. Vulpiani. *Dynamical Systems Approach to Turbulence*. Cambridge University Press, Cambridge, 1998.
- [11] K. Boomsma, D. Poulikakos, and F. Zwick. Metal foams as compact high performance heat exchangers. *Mech. Mater.*, 35:1161–1176, 2003.
- [12] J. G. Brasseur and Ch.-H. Wei. Interscale dynamics and local isotropy in high Reynolds number turbulence within triadic interactions. *Phys. Fluids*, 6(6):842–870, 1994.
- [13] W. P. Breugem and B. J. Boersma. Direct numerical simulations of turbulent flow over a permeable wall using a direct and a continuum approach. *Phys. Fluids*, 17:025103, 2005.
- [14] W. P. Breugem and D. A. S. Rees. A derivation of the volume-averaged Boussinesq equations for flow in porous media with viscous dissipation. *Transp. Porous Media*, 63(1):1–12, 2006.
- [15] O. Cadot, J. H. Titon, and D. Bonn. Observation of resonances in modulated turbulence. *J. Fluid Mech.*, 485:161–170, 2003.
- [16] R. Camussi, S. Ciliberto, and C. Baudet. Experimental study of the evolution of a velocity perturbation in fully developed turbulence. *Phys. Rev. E*, 56:06181, 1997.
- [17] C. Canuto, M. Hussaini, A. Quarteroni, and T. Zang. *Spectral Methods in Fluid Dynamics*. Springer Verlag (Berlin and New York), 1988.
- [18] M. Caponeri and S. Ciliberto. Thermodynamic aspects of the transition to spatiotemporal chaos. *Phys. D*, 58:365–383, 1992.
- [19] D. Carati, S. Ghosal, and P. Moin. On the representation of backscatter in dynamic localization models. *Phys. Fluids*, 7(3):606–616, 1995.

- 
- [20] J. R. Chasnov. Simulation of the Kolmogorov inertial subrange using an improved subgrid model. *Phys. Fluids*, 3(1):188–200, 1991.
- [21] S. Chen and X. Shan. High-resolution turbulent simulations using the Connection Machine–2. *Comput. Phys.*, 6(6):643–646, 1992.
- [22] H. Cheng and I. P. Castro. Near wall flow over urban-like roughness. *Boundary-Layer Meteorology*, 104(2):229–259, 2002.
- [23] J. H. Curry, J. R. Herring, J. Loncaric, and S. A. Orszag. Order and disorder in two- and three dimensional Bénard convection. *J. Fluid Mech.*, 147:1–38, 1984.
- [24] J. A. Domaradzki. Analysis of energy transfer in direct numerical simulations of isotropic turbulence. *Phys. Fluids*, 31(10):2747–2749, 1988.
- [25] J. A. Domaradzki. Nonlocal triad interactions and the dissipation range of isotropic turbulence. *Phys. Fluids A*, 4(9):2037–2045, 1992.
- [26] J. A. Domaradzki, W. Liu, C. Hartel, and L. Kleiser. Energy transfer in numerically simulated wall-bounded turbulent flows. *Phys. Fluids*, 6(4):1583–1599, 1994.
- [27] J. A. Domaradzki, R. W. Metcalfe, R. S. Rogallo, and J. J. Riley. Analysis of subgrid-scale eddy viscosity with use of results from Direct Numerical Simulations. *Phys. Rev. Lett.*, 58(6):547–550, 1987.
- [28] J. A. Domaradzki and R. S. Rogallo. Local energy transfer and non-local interactions in homogeneous, isotropic turbulence. *Phys. Fluids A*, 2(3):413–426, 1990.
- [29] J. Eggers and S. Grossmann. Does deterministic chaos imply intermittency in fully developed turbulence? *Phys. Fluids A*, 3(8):1958–1968, 1991.
- [30] V. Eswaran and S. B. Pope. An examination of forcing in direct numerical simulations of turbulence. *Comput. Fluids*, 16:257, 1988.
- [31] J. Finnigan. Turbulence in plant canopies. *Ann. Rev. Fluid Mech.*, 32:519–571, 2000.

- 
- [32] M. Frigo and S. G. Johnson. FFTW: An adaptive software architecture for the FFT. In *Proc. 1998 IEEE Int. Conf. Acoustics Speech and Signal Processing*, pages 1381–1384, <http://www.fftw.org>, 1998.
- [33] B. J. Geurts. Mixing efficiency in turbulent shear layers. *J. Turbul.*, 2:2–24, 2001.
- [34] B. J. Geurts. *Modern Simulation Strategies for Turbulent Flow*. R.T. Edwards, 2001.
- [35] B. J. Geurts. *Elements of Direct and Large-Eddy Simulation*. R.T. Edwards, 2004.
- [36] S. Ghosal, T. S. Lund, P. Moin, and K. Akselvoll. A dynamic localization model for large-eddy simulation of turbulent flows. *J. Fluid Mech.*, 286:229–255, 1995.
- [37] Silicon Graphics. SCSL User’s Guide. TechPubs Library of Silicon Graphics, <http://techpubs.sgi.com>.
- [38] S. Grossman and D. Lohse. Scaling in hard turbulent Rayleigh-Bénard flow. *Phys. Rev. A*, 46(2):903–917, 1992.
- [39] S. Grossmann and D. Lohse. Intermittency in the Navier–Stokes dynamics. *Z. Phys. B*, 89:11–19, 1992.
- [40] S. Grossmann and D. Lohse. Scale resolved intermittency in turbulence. *Phys. Fluids*, 6:611, 1994.
- [41] S. Grossmann and D. Lohse. Universality in fully developed turbulence. *Phys. Rev. E*, 50:2784, 1994.
- [42] HDF5 Group. HDF5 User’s Guide. National Center for Supercomputing Applications (NCSA), University of Illinois, <http://www.hdfgroup.org>.
- [43] F. Hayot and C. Jayaprakash. From scaling to multiscaling in the stochastic Burgers equation. *Phys. Rev. E*, 56(4):4259–4262, 1997.
- [44] A. v.d. Heydt, S. Grossmann, and D. Lohse. Response maxima in modulated turbulence. *Phys. Rev. E*, 67:046308, 2003.

- 
- [45] A. v.d. Heydt, S. Grossmann, and D. Lohse. Response maxima in modulated turbulence. II. Numerical simulations. *Phys. Rev. E*, 68:066302, 2003.
- [46] J. O. Hinze. *Turbulence: An Introduction to its Mechanism and Theory*. New York, McGraw-Hill, 1975.
- [47] D. D. Holm. Taylor’s hypothesis, Hamilton’s principle, and the LANS- $\alpha$  model for computing turbulence. *Los Alamos Science*, 29, 2005.
- [48] D. D. Holm, Ch. Jeffery, S. Kurien, D. Livescu, M. A. Taylor, and B. A. Wingate. The LANS- $\alpha$  model for computing turbulence - origins, results, and open problems. *Los Alamos Science*, 29, 2005.
- [49] J.-O. Hooghoudt, D. Lohse, and F. Toschi. Decaying and kicked turbulence in a shell model. *Phys. Fluids*, 13(7):2013–2018, 2001.
- [50] T. Ishihara and Y. Kaneda. High resolution DNS of incompressible homogeneous forced turbulence - time dependence of statistics. In Y. Kaneda and T. Gotoh, editors, *Statistical Theories and Computational Approaches to Turbulence*. Springer, 2003.
- [51] J. Jimenez. Turbulent flow over rough walls. *Ann. Rev. Fluid Mech.*, 36:173–196, 2004.
- [52] J. Jimenez, A. A. Wray, P. G. Saffman, and R. S. Rogallo. The structure of intense vorticity in isotropic turbulence. *J. Fluid Mech.*, 255:65–90, 1993.
- [53] L. Kadanoff, D. Lohse, J. Wang, and R. Benzi. Scaling and dissipation in the gey shell model. *Phys. Fluids*, 7:617–629, 1995.
- [54] Y. Kaneda, T. Ishihara, M. Yokokawa, K. Itakura, and A. Uno. Energy dissipation rate and energy spectrum in high resolution direct numerical simulations of turbulence in a periodic box. *Phys. Fluids*, 15(2):21–24, 2003.
- [55] M. Kearney. Control of fluid dynamics with engineered fractals - adsorption process applications. *Chem. Eng. Comm.*, 173:43–52, 1999.

- 
- [56] R. M. Kerr. Higher-order derivative correlations and the alignment of small-scale structures in isotropic numerical turbulence. *J. Fluid Mech.*, 153:31–58, 1985.
- [57] R. M. Kerr. Velocity, scalar and transfer spectra in numerical turbulence. *J. Fluid Mech.*, 211:309–332, 1990.
- [58] A. N. Kolmogorov. The local structure of turbulence in incompressible viscous fluids at very large Reynolds numbers. *C.R. Acad. Sci. URSS*, 30:301–305, 1941.
- [59] A. N. Kolmogorov. A refinement of previous hypothesis concerning the local structure of turbulence in a viscous incompressible fluid at high Reynolds number. *J. Fluid Mech.*, 13:82–85, 1962.
- [60] A. K. Kuczaj and B. J. Geurts. Mixing in manipulated turbulence. *J. Turbul.*, to appear.
- [61] A. K. Kuczaj, B. J. Geurts, and D. Lohse. Response maxima in time-modulated turbulence: Direct Numerical Simulations. *Europhys. Lett.*, 73(6):851–857, 2006.
- [62] A. K. Kuczaj, B. J. Geurts, D. Lohse, and W. v.d. Water. Turbulence modification by periodically modulated scale-dependent forcing. *Comput. Fluids*, submitted.
- [63] A. K. Kuczaj, B. J. Geurts, and W. D. McComb. Nonlocal modulation of energy cascade in broadband-forced turbulence. *Phys. Rev. E*, 74:016306, 2006.
- [64] S. Kurien and K. R. Sreenivasan. Anisotropic scaling contributions to high-order structure functions in high-Reynolds-number turbulence. *Phys. Rev. E*, 62(2):2206–2212, 2000.
- [65] F. Li, L. Lefferts, and T. H. v.d. Meer. Study on heat transfer enhancement by metallic foams with carbon nano fibers (CNFs). In *Proc. 6th World Conference on Experimental Heat Transfer, Fluid Mechanics, and Thermodynamics*, Matsushima, Japan, April 2005.
- [66] D. Lohse. Periodically kicked turbulence. *Phys. Rev. E*, 62:4946, 2000.



- 
- [67] L. Machiels. Predictability of small-scale motion in isotropic fluid turbulence. *Phys. Rev. Lett.*, 79(18):3411–3414, 1997.
- [68] V.G. Maz'ja. *Sobolev spaces*. Springer Verlag – Berlin, 1985.
- [69] B. Mazzi, F. Okkels, and J. C. Vassilicos. A shell-model approach to fractal-induced turbulence. *Eur. Phys. J. B*, 28:243–251, 2002.
- [70] B. Mazzi and J. C. Vassilicos. Fractal generated turbulence. *J. Fluid Mech.*, 502:65–87, 2004.
- [71] W. D. McComb. *The Physics of Fluid Turbulence*. Oxford University Press, 1990.
- [72] W. D. McComb and K. T. J. Chan. Drag reduction in fibre suspension. *Nature*, 292:520–522, 1981.
- [73] W. D. McComb and K. T. J. Chan. Laser-Doppler anemometer measurements of the turbulent structure in drag-reducing fibre suspensions. *J. Fluid Mech.*, 152:455–478, 1985.
- [74] W. D. McComb, A. Hunter, and C. Johnston. Conditional mode-elimination and the subgrid-modeling problem for isotropic turbulence. *Phys. Fluids*, 13(7):2030–2044, 2001.
- [75] C. Meneveau, T. S. Lund, and J. Chasnov. On the local nature of the energy cascade. In *Proceedings of the Summer Program - Studying Turbulence Using Numerical Simulation Databases – IV*. Center for Turbulence Research (CTR), November 1992.
- [76] J. Meyers. *Accuracy of Large-Eddy Simulation strategies*. PhD thesis, Katholieke Universiteit Leuven, 2004.
- [77] J. Meyers, B. J. Geurts, and M. Baelmans. Database analysis of errors in large-eddy simulation. *Phys. Fluids*, 15(9):2740–2755, 2003.
- [78] A. Misra and D. I. Pullin. A vortex-based subgrid stress model for large-eddy simulation. *Phys. Fluids*, 9(7):2443–2454, 1997.
- [79] D. Mitra, J. Bec, R. Pandit, and U. Frisch. Is multiscaling an artifact in the stochastically forced Burgers equation? *Phys. Rev. Lett.*, 94:194501, 2005.

- 
- [80] K. Mohseni, B. Kosovic, S. Shkoller, and J. E. Marsden. Numerical simulations of the Lagrangian Averaged Navier-Stokes equations for homogeneous isotropic turbulence. *Phys. Fluids*, 15(2):524–544, 2003.
- [81] P. Moin and T. Bewley. Feedback control of turbulence. *Appl. Mech. Rev.*, 47:S3, 1994.
- [82] P. Moin and J. Kim. Tackling turbulence with supercomputers. *Scientific American Magazine (SIAM)*, January 1997.
- [83] MPI. Message Passing Interface. <http://www.mpi-forum.org>.
- [84] K. Ohkitani and S. Kida. Triad interactions in a forced turbulence. *Phys. Fluids A*, 4(4):794–802, 1992.
- [85] M. R. Overholt and S. B. Pope. A deterministic forcing scheme for direct numerical simulations of turbulence. *Comput. Fluids*, 27(1):11–28, 1998.
- [86] S. B. Pope. *Turbulent Flows*. Cambridge University Press, 2000.
- [87] A. Pouquet, U. Frisch, and J. P. Chollet. Turbulence with a spectral gap. *Phys. Fluids*, 26(4):877–880, 1983.
- [88] R. S. Rogallo. An ILLIAC program for the numerical simulation of homogeneous incompressible turbulence. Technical Report NASA-TM-73203, NASA, 1977.
- [89] R. S. Rogallo. Numerical experiments in homogeneous turbulence. Technical Report NASA-TM-81315, NASA, 1981.
- [90] A. Sain, Manu, and R. Pandit. Turbulence and multiscaling in the randomly forced Navier–Stokes equation. *Phys. Rev. Lett.*, 81(20):4377–4380, 1998.
- [91] SARA. Computing and Networking Services. <http://www.sara.nl>.
- [92] X. Shen and Z. Warhaft. The anisotropy of the small scale structure in high Reynolds number ( $R_\lambda = 1000$ ) turbulent shear flow. *Phys. Fluids*, 12(11):2976–2989, 2000.

- 
- [93] E. D. Siggia. Numerical study of small-scale intermittency in three-dimensional turbulence. *J. Fluid Mech.*, 107:375–406, 1981.
- [94] E. D. Siggia and G. S. Patterson. Intermittency effects in a numerical simulation of stationary three-dimensional turbulence. *J. Fluid Mech.*, 86:567, 1978.
- [95] Y. Suzuki and Y. Nagano. Modification of turbulent helical/nonhelical flows with small-scale energy input. *Phys. Fluids*, 11(11):3499–3511, 1999.
- [96] S. F. Tardu, G. Binder, and R. F. Blackwelder. Turbulent channel flow with large-amplitude velocity oscillations. *J. Fluid Mech.*, 267:109–151, 1994.
- [97] C. Tipton and W. v.d. Water. Modulated turbulence. *Phys. Rev. Lett.*, page submitted, 2006.
- [98] J. H. Titon and O. Cadot. The statistics of power injected in a closed turbulent flow: Constant torque forcing versus constant velocity forcing. *Phys. Fluids*, 15(3):625–640, 2003.
- [99] A. A. Townsend. *The Structure of Turbulent Shear Flows*. Cambridge Univ. Press, 1976.
- [100] A. Tsinober. *An Informal Introduction to Turbulence*. Kluwer, 2002.
- [101] A. Vincent and M. Meneguzzi. The spatial structure and statistical properties of homogeneous turbulence. *J. Fluid Mech.*, 225:1–20, 1991.
- [102] F. Waleffe. The nature of triad interactions in homogenous turbulence. *Phys. Fluids A*, 4(2):350–363, 1992.
- [103] L. P. Wang, S. Chen, J. G. Brasseur, and J. C. Wyngaard. Examination of hypotheses in the Kolmogorov refined turbulence theory through high-resolution simulations. Part 1. Velocity field. *J. Fluid Mech.*, 309:113–156, 1996.
- [104] T. Watanabe and T. Gotoh. Statistics of a passive scalar in homogeneous turbulence. *New J. Phys.*, 6(40):1–36, 2004.

- [105] P. Wesseling. *An introduction to multigrid methods*. Wiley, New York, 1992.
- [106] S. Whitaker. The Forchheimer equation: a theoretical development. *Transp. Porous Media*, 25:27–61, 1996.
- [107] Y. Yamazaki, T. Ishihara, and Y. Kaneda. Effects of wavenumber truncation on high-resolution direct numerical simulation of turbulence. *J. Phys. Soc. Jpn.*, 71(3):777–781, 2002.
- [108] P. K. Yeung and J. G. Brasseur. The response of isotropic turbulence to isotropic and anisotropic forcing at the large scales. *Phys. Fluids A*, 3(5):884–897, 1991.
- [109] P. K. Yeung, J. G. Brasseur, and Q. Wang. Dynamics of direct large-small scale couplings in coherently forced turbulence: concurrent physical- and Fourier-space views. *J. Fluid Mech.*, 283:43–95, 1995.
- [110] A. J. Young. *Investigation of Renormalization Group Methods for the Numerical Simulation of Isotropic Turbulence*. Phd thesis, University of Edinburgh, 1999.
- [111] Y. Zhou. Degrees of locality of energy transfer in the inertial range. *Phys. Fluids A*, 5(5):1092–1094, 1993.
- [112] Y. Zhou. Interacting scales and energy transfer in isotropic turbulence. *Phys. Fluids A*, 5(10):2511–2524, 1993.
- [113] Y. Zhou and Ch. G. Speziale. Advances in the fundamental aspects of turbulence: Energy transfer, interacting scales, and self-preservation in isotropic decay. *Appl. Mech. Rev.*, 51(4):267–301, 1998.
- [114] Y. Zhou, P. K. Yeung, and J. G. Brasseur. Scale disparity and spectral transfer in anisotropic numerical turbulence. *Phys. Rev. E*, 53(1):1261–1264, 1996.

# Summary

This thesis is devoted to turbulent mixing. Various flow problems arising in science and technology are intimately connected to properties of turbulent transport. Improvements and control of mixing efficiency rely directly on the understanding of turbulence phenomena. From the mathematical point of view, turbulence is governed by the Navier–Stokes equations. The convective nonlinearity in these equations induces an interaction between a wide range of scales in a flow. In addition, the dissipation term acts mainly on the smallest flow scales, characterized by the fluid viscosity. In the absence of external forces these two terms fully dictate the dynamics of decaying turbulence. In numerical studies of turbulence dynamics one usually incorporates an external forcing to supply energy to the largest flow scales. Correspondingly, we observe an average energy cascading process from the largest to the smallest scales that is well depicted by the so-called Kolmogorov K41 theory.

Actual flows seen in nature are often influenced by boundary conditions, e.g., due to a complex shape of the flow domain such as a forest canopy. Such flows do not follow the K41 predictions. This intriguing fact directly affects the turbulent mixing and motivated the research presented in this thesis. Throughout, we focus on numerical studies of *controlled non-Kolmogorov turbulence*. We concentrated on the canonical problem of flow in a cubic box with periodic conditions. The perturbations arising from flow through and along complex boundaries are represented by broadband forcing. Apart from large-scale agitation of the flow to supply most of the energy, the forcing is allowed to simultaneously act in a broader range of scales, thereby explicitly disturbing the K41 energy cascading process. To study different variants of flow agitation we developed a 3D parallel (MPI) simulation code based on the incompressible Navier–Stokes equations.

We interpreted broadband forcing methods as part of the modeling of flow along complex boundaries. The consequences of adopting different ranges and strengths of externally forced scales were investigated, both in terms of the quality of mixing of embedded passive scalar fields in physical space (Chapter 2) as well as in terms of alterations in the spectral space triadic interactions (Chapter 3). Arising from small-scale forcing, we observed a characteristic depletion in the energy spectrum at part of the inertial scales.

This corresponds to *immediate* transfer of the energy to smaller scales as opposed to gradual ‘cascading’. A similar “spectral by-pass” phenomenon was observed in flow over canopies. The broadband forcing was found to enhance the overall (time-integrated) mixing efficiency measured in terms of surface area and wrinkling of level sets of passive scalar fields, in a range of Reynolds and Schmidt numbers. The instantaneous mixing was found to reach highest levels for the classical Kolmogorov large-scale forced turbulence. However, control may be obtained over the time-scale at which maximal mixing is achieved and over the accumulated level of mixing.

In nature, flows are often modulated by periodic forcing. This arises, for example, in flows that are influenced by the periodic cycles due to the Earth’s rotation and heating from the Sun. This motivated to investigate turbulent flows under the influence of periodically modulated large-scale forcing. Periodic agitation of turbulent flows was recently studied experimentally, e.g., in forced swirling flow and in windtunnels with periodically cycled active grids. These studies suggest the existence of response maxima of the turbulence at frequencies on the order of the inverse of the eddy-turnover time. This was also predicted theoretically using a mean-field approach. Based on full-scale direct numerical simulations we confirmed the existence of response maxima in periodically agitated turbulence (Chapter 4). We also conducted a comprehensive parameter study and investigated the response of turbulent flow to time-modulated forcing at various length scales, forcing strengths and forcing protocols (Chapter 5).

The numerical investigation of forcing strategies has established the strong external influence that may be exerted on the turbulent cascading process. This is directly connected to generic control over turbulent dispersion. The application-goal of future studies could be directed towards the explicit connection of forcing strategies to real-life stirrers and agitation protocols. This would connect controlled turbulent transport to a detailed understanding of the spectral space interactions among the relevant dynamic flow scales, creating a direct connection between better mixing, improved heat-transfer and better insight in turbulence.

# Samenvatting

Dit proefschrift is gewijd aan turbulente menging. Diverse stromingsproblemen uit de natuur en techniek zijn nauw verbonden met eigenschappen van turbulent transport. Mogelijkheden tot verbetering van en controle over de meng-efficiëntie hangen direct samen met het begrip van turbulente fenomenen. Vanuit wiskundig oogpunt bezien wordt turbulentie beschreven door de Navier–Stokes vergelijkingen. De convectieve niet-lineariteit in deze vergelijkingen induceert een interactie tussen een breed scala aan lengteschalen in een stroming. Daarnaast oefent de dissipatieve term zijn invloed vooral uit op de kleinste lengteschalen, gekenmerkt door de viscositeit. Bij afwezigheid van externe krachten dicteren deze twee termen de dynamica van uitdempende turbulentie volledig. In numerieke simulaties van turbulentie wordt vaak een externe aandrijving meegenomen om zo energie aan de grootste lengteschalen in een stroming toe te voeren. Hiermee samenhangend kan men dan een gemiddelde energie-cascade observeren van de grootste naar de kleinste lengteschalen die goed wordt beschreven door de zogenoemde Kolmogorov K41 theorie.

Daadwerkelijke stromingen zoals in de natuur voorkomen worden vaak sterk beïnvloed door randcondities, bijv., doordat de stroming in een domein met complexe vorm plaatsvindt zoals het bladerdak van een bos. Dergelijke stromingen volgen de K41 theorie niet. Dit intrigerende feit heeft ook directe gevolgen voor turbulente menging en motiveerde het onderzoek dat in dit proefschrift is beschreven. We richten ons daarbij op numerieke studies van *gecontroleerde niet-Kolmogorov turbulentie* en concentreren ons met name op het kanonieke probleem van stroming in een kubisch rekendomein met periodieke condities. De verstoringen die ontstaan doordat de stroming door en langs complexe randen plaatsvindt wordt gerepresenteerd door een ‘breedband aandrijving’. Behalve de grote-schaal aandrijving van de stroming, waarmee het grootste deel van de energie wordt toegevoerd, staan we hierbij ook een gelijktijdige aandrijving van een scala aan kleinere lengteschalen toe, waarmee we expliciet het K41 energie-cascade proces modificeren. Om de verschillende varianten van stromings-aandrijving te kunnen bestuderen is een 3D parallelle (MPI) simulatie-code ontwikkeld, gebaseerd op de incompressibele Navier–Stokes vergelijkingen.

We hebben de breedband aandrijvings-methodes geïnterpreteerd als onderdeel van de modellering van stroming langs complexe randen. De consequenties van het aandrijven van verschillende lengteschalen, met verschillende amplitudes, zijn onderzocht, zowel wat betreft de kwaliteit van de menging van passieve scalaire velden in de fysische ruimte (Hoofdstuk 2) als ook in termen van veranderingen in de triadische interacties in de spectrale ruimte (Hoofdstuk 3). Als gevolg van de verstoring van de kleine schalen werd een karakteristieke afname in het energie-spectrum waargenomen in een deel van de inertieële schalen. Dit hangt samen met de *directe* overdracht van energie naar de kleinere schalen, in tegenstelling tot een meer graduele cascade van energie. Een vergelijkbaar “spectraal by-pass” fenomeen is waargenomen in de stroming over bosgebieden. De breedband aandrijving leidt er toe dat de (tijds-gemiddelde) meng-efficiëntie toeneemt, gemeten in termen van het oppervlakte en de ‘rimpeling’ van iso-vlakken van de passieve scalaire velden, in een gebied van Reynolds en Schmidt getallen. De instantane menging was maximaal voor de klassieke Kolmogorov aangedreven turbulentie. Echter, controle kan worden verkregen over de tijdschaal waarop maximale menging kan worden bereikt en de geaccumuleerde menging.

In de natuur worden stromingen vaak gemoduleerd door een periodieke aandrijving. Dit komt bijvoorbeeld voor in stromingen die worden beïnvloed door de periodieke cycli tengevolge van de rotatie van de Aarde en de opwarming door de Zon. Dit motiveerde een onderzoek naar de invloed van periodiek gemoduleerde grote-schaal aandrijving. Dergelijke periodieke aandrijving is recent experimenteel onderzocht, bijv., in aangedreven ‘wervelende’ stroming en in een windtunnel met periodiek aangedreven actieve roosters. Deze studies suggereren het bestaan van maxima in de turbulentie-respons, bij frequenties van de orde van de inverse ‘eddy-turnover’ tijd. Dit is ook theoretisch voorspeld in een gemiddeld-veld aanpak. Gebaseerd op directe numerieke simulaties hebben we het bestaan van dergelijke respons maxima in periodiek aangedreven stromingen kunnen bevestigen (Hoofdstuk 4). We hebben daarnaast een omvattende studie verricht naar de respons van turbulente stroming op tijds-gemoduleerde gelijktijdige aandrijving van diverse lengte-schalen, bij verschillende aandrijf-amplitudes en aandrijf protocollen (Hoofdstuk 5).



Het numerieke onderzoek naar turbulente aandrijf-strategieën heeft de sterke externe beïnvloedbaarheid van het energie-cascade proces aangetoond. Dit is direct verbonden met generieke controle van turbulente dispersie. Toekomstig toegepast onderzoek zou zich met name kunnen richten op de expliciete relatie tussen aandrijf-strategie en de daadwerkelijke roer-mechanismen en protocollen die worden ingezet. Dit zou gecontroleerd turbulent transport direct koppelen aan een gedetailleerd begrip van de interacties tussen de diverse relevante stromingsschalen en daarmee een verbinding leggen tussen betere menging, betere warmteoverdracht en een beter begrip van turbulentie.



# Curriculum vitae

Arkadiusz K. Kuczaj was born on 11 April 1975 in Nowa Ruda, Poland. He obtained his secondary education at the Henryk Sienkiewicz High School in Nowa Ruda.

In August 1994 he started studies in Applied Physics at the Military University of Technology (MUT) in Warsaw, Poland. After the first year, he joined the group of physicists who were prepared during their studies for future work in military research institutes. During individual studies he specialized in the field of Computational Physics. He graduated in June 1999 with the MSc thesis "Modelling of the detonation products scattering from a cylindrical explosive charge".

After finishing his MSc he started to work as a CFD Research Engineer in the Department of Explosives and Physics of Explosion at the Military University of Technology. His research interest oscillated around high-order Godunov-type methods, numerical simulations of shock/blast waves propagation, physics of explosion, parallel computations, and analysis of numerical methods for nonlinear partial differential equations.

In June 2000 he began a two-year postgraduate Software Engineering Program in Computer Science at the Jagiellonian University in Cracow, Poland. He mainly concentrated on software engineering methodologies, object oriented and parallel programming, and specialized in Distributed Computing.

In January 2003 he started to work towards a PhD at the University of Twente, the Netherlands. He worked in the project "Fractal forcing of anisotropic, inhomogeneous turbulence; flow structure and heat transfer" that was part of the Fundamental Research on Matter (FOM) program. He concentrated on direct numerical simulations and modelling of turbulent fluid-flow phenomena, investigating the fundamental aspects of turbulence, e.g., energy-transfer processes in controlled non-Kolmogorov turbulence, passive scalar mixing in modulated turbulence, and periodically forced turbulence. In 2006 he participated in the Summer Research Program held in the Center of Nonlinear Studies at the Los Alamos National Laboratory, USA.

The main areas of his research interest are Computational Fluid Dynamics, High-Performance Computing, Software Engineering, Physics of Explosion, and Numerical Analysis.

## Publications and conference contributions

- *Control over multiscale mixing in broadband-forced turbulence*, A.K. Kuczaj, B.J. Geurts, IUTAM Symposium 2006 “Computational Physics and New Perspectives in Turbulence”, September, 2006, Nagoya, Japan
- *Turbulence modification by periodically modulated scale-dependent forcing*, A.K. Kuczaj, B.J. Geurts, D. Lohse, W.v.d. Water, Conference on Turbulence and Interactions (TI2006), May, 2006 Porquerolles, France, submitted to **Computers & Fluids**
- *Mixing in manipulated turbulence*, A.K. Kuczaj, B.J. Geurts, **Journal of Turbulence**, to appear
- *Nonlocal modulation of the energy cascade in broadband-forced turbulence*, A.K. Kuczaj, B.J. Geurts, W.D. McComb, **Physical Review E**, 74, 016306, 2006
- *Response maxima in time-modulated turbulence: Direct Numerical Simulations*, A.K. Kuczaj, B.J. Geurts, D. Lohse, **Europhysics Letters**, 73(6), 2006
- *Modeling turbulence in complex domains using explicit multi-scale forcing*, A.K. Kuczaj, B.J. Geurts, ERCOFTAC Workshop Direct and Large-Eddy Simulation 6 (DLES6), September, 2005, Poitiers, France, In: ERCOFTAC Series, Vol. 10, Eds.: E. Lamballais, R. Friedrich, B. J. Geurts, O. Metais, 2006
- *Spatially localized broad-band forcing of turbulent flow*, A.K. Kuczaj, B.J. Geurts, In: Advances in Turbulence X, 10<sup>th</sup> European Turbulence Conference, June, 2004, Trondheim, Norway, Eds.: H. I. Anderson, P.-A. Krogstad, CIMNE, Barcelona, Spain, 2004

- *Numerical modelling of blast waves generated by explosion of an elongated gaseous cloud*, A. Kuczaj, **Journal of Technical Physics**, 43 (1), 2002
- *Riemann Problem - a survey of numerical solutions for hydrodynamic computations*, A. Kuczaj, *Biuletyn WAT*, 51(2), 2002
- *Development of mathematical methods for modelling of explosion phenomenon and its influence on structures*, R. Trebinski, Z. Legowski, A. Kuczaj, PBW 720/00 Report, Warsaw, WAT, III-15413, 2001
- *Object Oriented Programming - Fortran 90/95 versus C++ for Scientific Computations*, A. Kuczaj, 5<sup>th</sup> School of Computer Aided Design, Production and Utilization, May, 2001, Szczyrk, Poland

